TOTAL CROSS SECTION MEASUREMENTS FOR THE SCATTERING OF POLARIZED NEUTRONS FROM POLARIZED ^{3}HE

by

CHRISTOPHER DOUGLAS KEITH

A dissertation submitted to the Graduate Faculty of
North Carolina State University
in partial fulfillment of the
requirements for the Degree of
Doctor of Philosophy

Department of Physics

Raleigh
1994

APPROVED BY:

N. Russell Roberson	Werner Tornow
Christopher R. Gould, Co-Chairman	David G. Haase, Co-Chairman

ABSTRACT

KEITH, CHRISTOPHER DOUGLAS, Total Cross Section Measurements for the Scattering of Polarized Neutrons from Polarized ^{3}He. (Under the direction of Christopher R. Gould and David G. Haase.)

The first measurements of polarized neutron—polarized ^{3}He scattering in the few MeV region have been performed. Measurements of the total cross section difference $\Delta\sigma_T$ have been obtained for incident neutron energies 1–10 MeV. The experiment was performed with both beam and target spins in the horizontal plane, transverse to the incident beam momentum. The results are sensitive to the excited state structure of the alpha particle and are compared to phase-shift predictions based on a number of analyses of the n-^{3}He system. The $\Delta\sigma_T$ results are in agreement with a recent R-matrix analysis of $A = 4$ scattering and reaction data, and lend support to the ^{4}He level scheme derived from that analysis. None of the analyses considered here are able to simultaneously reproduce both the current results and previous measurements of the unpolarized total cross section.

The experiment was performed at the Triangle Universities Nuclear Laboratory and its Polarized Target Facility. The polarized neutron beam is produced as a secondary beam through polarization-transfer reactions with polarized protons and deuterons. The beams of polarized charged particles are obtained from the TUNL Atomic Beam Polarized Ion Source and accelerated by a tandem Van de Graaff. The beam polarization is monitored by a carbon-foil polarimeter located after the accelerator.

A statically-polarized target of solid ^{3}He was developed for the experiment. A 0.4 mole sample of solid ^{3}He is grown under a pressure of 45.5 bars at 1 K and cooled to 12 mK with a ^{3}He-^{4}He dilution refrigerator. A 7 Tesla superconducting split-coil magnet is used to polarize the nuclear spins to nearly 40%. The temperature is determined by two independent thermometric standards: ^{60}Co γ-ray anisotropy and the ^{3}He melting curve. For temperatures below 20 mK, agreement between the two methods is better than 2%. We observe no heating in the target due to neutron or γ-ray induced reactions. The density of the 2.16 cm long ^{3}He sample is 2.0×10^{22} atoms/cm^3, two orders of magnitude greater than any current gas target of polarized ^{3}He. The target is well-suited for a variety of nuclear physics experiments in which a dense target of polarized ^{3}He is desirable.

Biography

Christopher Douglas Keith

Personal

Born in Elizabethton, Tennessee, July 27, 1965
Married Jacqueline Kelly, October 18, 1991

Education

B.S. Physics, University of North Carolina—Asheville, 1987
M.S. Physics, North Carolina State University, 1990
Thesis Title: *Application of ^{3}He Melting Curve Thermometry in a Nuclear Orientation Experiment*

Academic Positions

President, UNCA Society of Physics Students, 1986–1987
Teaching Assistant, NCSU, 1987–1989
Research Assistant, NCSU, 1989–1994

Memberships

American Physical Society
Sigma Pi Sigma
Sigma Xi

Publications

C. D. Keith, C. R. Gould, D. G. Haase, G. M. Hale, H. M. Hofmann, H. Postma, N. R. Roberson, and W. Tornow. *Sensitivity of Polarized Neutron–Polarized ^{3}He Scattering to the Excited Level Structure of ^{4}He.* Physical Review C, **50** 237 (1994).

C. D. Keith, C. R. Gould, D. G. Haase, P. R. Huffman, N. R. Roberson, M. K. Seely, W. Tornow, and W. S. Wilburn. *Measurement of the Polarized Neutron – Polarized ^{3}He Total Cross Section.* To appear in *Proceedings of the XIV International Conference on Few-Body Problem in Physics,* Williamsburg, VA (May, 1994).

C. D. Keith, C. R. Gould, D. G. Haase, P. R. Huffman, N. R. Roberson, M. L. Seely, W. Tornow, and W. S. Wilburn. *Realization of a Statically Polarized Solid ^{3}He Target for Measurements of Neutron Transmission at MeV Energies.* Accepted for publication in Nuclear Instruments and Methods A (September, 1994).

C. D. Keith, C. R. Gould, D. G. Haase, N. R. Roberson, W. Tornow, and W. S. Wilburn. *^{3}He Melting Curve Thermometry in a Nuclear Polarization Experiment.* Hyperfine Interactions, **75** 525 (1992).

C. R. Gould, D. G. Haase, P. R. Huffman, C. D. Keith, N. R. Roberson, M. L. Seely, and W. S. Wilburn, *Neutron Transmission Tests of Parity Conserving Time Reversal Non Invariance.* To appear in *Proceedings of the 5th International Conference on the Intersections of Particle and Nuclear Physics,* St. Petersburg, FL (June, 1994).

D. G. Haase, C. D. Keith, C. R. Gould, P. R. Huffman, N. R. Roberson, M. L. Seely, and W. S. Wilburn, *A Statically Polarized Solid ^{3}He Target.* To appear in *Proceedings of the 8th International Symposium on Polarization Phenomena in Nuclear Physics,* Bloomington, IN (September, 1994).

P. R. Huffman, C. R. Gould, D. G. Haase, C. D. Keith, N. R. Roberson, M. L. Seely, W. S. Wilburn, and N. R. Roberson, *An Experimental Test of P-Even Time Reversal Invariance with MeV Neutrons.* To appear in *Proceedings of the 8th International Symposium on Polarization Phenomena in Nuclear Physics,* Bloomington, IN (September, 1994).

M. K. Seely, C. R. Gould, D. G. Haase, P. R. Huffman, C. D. Keith, N. R. Roberson, W. Tornow, and W. S. Wilburn. *Polarized Targets at Triangle Universities Nuclear Laboratory.* To appear in Nuclear Instruments and Methods.

W. S. Wilburn, C. R. Gould, D. G. Haase, P. R. Huffman, C. D. Keith, J. E. Koster, N. R. Roberson, and W. Tornow. *Measurements of Polarized Neutron–Polarized Proton Scattering: Implications for the Triton Binding Energy.* Physical Review Letters, **71** 1982 (1993).

W. S. Wilburn, P. R. Huffman, J. E. Koster, N. R. Roberson, W. Tornow, C. R. Gould, D. G. Haase, and C. D. Keith. *The NN Tensor Force from $\vec{n}$-$\vec{p}$ Scattering.* In I. R. Afnan and R. T. Cahill, editors, *Proceedings of the XIII International Conference on Few-Body Problems in Physics,* Adelaide (1992).

W. S. Wilburn, C. R. Gould, D. G. Haase, P. R. Huffman, C. D. Keith, N. R. Roberson, and W. Tornow. *Measurements at Low Energies of the Polarization Transfer Coefficient $K_y^{y'}$ for the Reaction $^3H(\vec{p},\vec{n})^3He$ at 0°.* In preparation.

Contributed Abstracts

C. D. Keith, C. R. Gould, D. G. Haase, P. R. Huffman, N. R. Roberson, W. Tornow, and W. S. Wilburn. *A Polarized Solid ^3He Target for Polarized Neutron Scattering.* Bulletin of the American Physical Society, **39** 1042 (1994).

C. D. Keith, C. R. Gould, D. G. Haase, P. R. Huffman, N. R. Roberson, W. Tornow, and W. S. Wilburn. *Level Structure of ^4He and the Spin Dependence of the n-^3He Total Cross Section.* Bulletin of the American Physical Society, **37** 1257 (1992).

C. D. Keith, D. G. Haase, C. R. Gould, W. S. Wilburn, N. R. Roberson, and W. Tornow. *Application of ^3He Melting Curve Thermometry in a Nuclear Orientation Cryostat.* Bulletin of the American Physical Society, **35** 2361 (1990).

Co-Authored Abstracts

W.S. Wilburn, P.R. Huffman, J.E. Koster, N.R. Roberson, W. Tornow, C.R. Gould, D.G. Haase, and C.D. Keith. *Measurements of Polarized Neutron–Polarized Proton Scattering: Implications for the Triton Binding Energy.* Bulletin of the American Physical Society, **38** 1846 (1993).

W.S. Wilburn, P.R. Huffman, J.E. Koster, N.R. Roberson, W. Tornow, C.R. Gould, D.G. Haase, and C.D. Keith. *Measurement of $\Delta\sigma_T$ in Polarized Neutron/Polarized Proton Scattering.* Bulletin of the American Physical Society, **37** 902 (1992).

Oral Presentations

Measurement of the Polarized Neutron– Polarized ^{3}He Total Cross Section. Given at the XIV International Conference on Few-Body Problems in Physics, Williamsburg, VA (May, 1994).

A Polarized Solid ^{3}He Target for Polarized Neutron Scattering. Given at the 1994 Joint April Meeting of the American Physical Society and the American Association of Physics Teachers, Crystal City, VA (April, 1994).

Level Structure of ^{4}He and the Spin Dependence of the n-^{3}He Total Cross Section. Given at the 1992 Annual Fall Meeting of the APS Division of Nuclear Physics, Santa Fe, NM (October, 1992).

Investigation of the ^{4}He Excited Level Structure with a Solid Polarized ^{3}He Target. Given at the 5th Annual Summer School for Nuclear Physics Research, Corvallis, OR (July, 1992).

Application of ^{3}He Melting Curve Thermometry in a Nuclear Orientation Cryostat. Given at the 1990 Annual Meeting of the Southeastern Section of the APS, Atlanta, GA (Nov. 1990).

Acknowledgements

One of the nicer things about writing a dissertation is the opportunity to thank the people who helped you get to this point. I owe the success of this project to the hard work, the advice, and the words of encouragement I received from several individuals. First I am deeply indebted to the members of my advisory committee, Drs. Chris Gould, David Haase, Russell Roberson, and Werner Tornow. Each of these four gentlemen has taught me something about how to be a physicist. I hope that I am someday able to pass this knowledge along.

I especially want to acknowledge the contributions of Scott Wilburn and Paul Huffman. Most of the neutron collimation and data acquisition systems used in this experiment is Dr. Wilburn's handiwork, and Mr. Huffman put in considerable time — despite the fact that he was beginning his own experiment. And although he joined the Polarized Target Group rather late in the experiment, Dr. Mike Seely somehow managed to make himself invaluable. A number of other students, notably Tim Murphy and Brian Raichle, donated their time to the experiment, helping me assemble the spin-spin cryostat countless times. Dr. Jim Koster provided sage advice from his terminal in Los Alamos, and four thousand miles away in Berlin, Gertrude Reiss kept her fingers crossed. Dr. Ross Setze was kind enough to guard my office in the wee hours of the night.

For the support I received from others at TUNL, I am very grateful. Lack of space prevents me from thanking each member of the Duke Instrument Shop, but I would be remiss in not mentioning Bob Hogan or Robert Timberlake. The ^{3}He target container was expertly machined by Mr. Jimmy Johnson of the NCSU instrument shop. At one time or another, Sidney Edwards and Patrick Mulkey have either built, repaired, or modified nearly every piece of electronic equipment used in this experiment. More than any anyone else, Paul Carter, Chris Westerfeldt, John Dunham and Richard O'Quinn are responsible for keeping TUNL running smoothly.

I received considerable theoretical support from Dr. Gerry Hale at LANL and Dr. Hartmut Hofmann from the Universität of Erlangen-Nürnberg in Germany. My understanding of few-nucleon systems also benefited from several discussions with Dr. Don Lehman of George Washington University. In the early stages of the experiment, a great deal of work was done by Dr. Hans Postma, on sabbatical from the

University of Technology, Delft, The Netherlands.

I also give thanks to Mike Schapira and Jon Rowley. Their words of encouragement are fondly remembered. Finally, and most importantly, I would like to thank my parents, Don and Thelma Keith, and my wife Jacqueline. I owe more to these three people than I can ever possibly repay. My parent's faith in me and their constant support are the foundation for everything I will ever achieve. This dissertation is dedicated to Jackie. If there are bounds to her patience, understanding, or love, I have not yet found them.

Contents

List of Figures

List of Tables

Chapter 1

Introduction

This thesis reports measurements of the total cross section for polarized neutrons scattering from polarized ^{3}He. The results are compared to the resonant structure of the ^{4}He nucleus. Additionally, the design, construction and operation of a polarized solid ^{3}He target are described. The target is statically polarized to 37% at 12 mK by application of a 7 Tesla magnetic field. The target used for this experiment is the largest polarized ^{3}He target constructed to date.

1.1 The Resonant Structure of ^{4}He

The four-nucleon (4N) system, particularly the α particle, has received considerable attention during the last two decades. Much of this interest has been triggered by theoretical advances in the field of few-nucleon dynamics. It is hoped that the present experimental results will provide new understanding of the role of few-nucleon dynamics in the 4N continuum.

At present, meson-exchange models provide the most quantitative treatment of the nucleon-nucleon (NN) interaction. In these models the nucleon is treated as a fundamental (non-composite) particle, and it interacts with other nucleons by exchanging one or more meson particles. Most of the observed properties of the two-nucleon system can now be reproduced with these "semi-phenomenological"[1] models [Sto94]. See Machleidt [Mac89] for a comprehensive treatment of the theory.

[1] Semi-phenomenological because we know that both nucleons and mesons are composed of quarks.

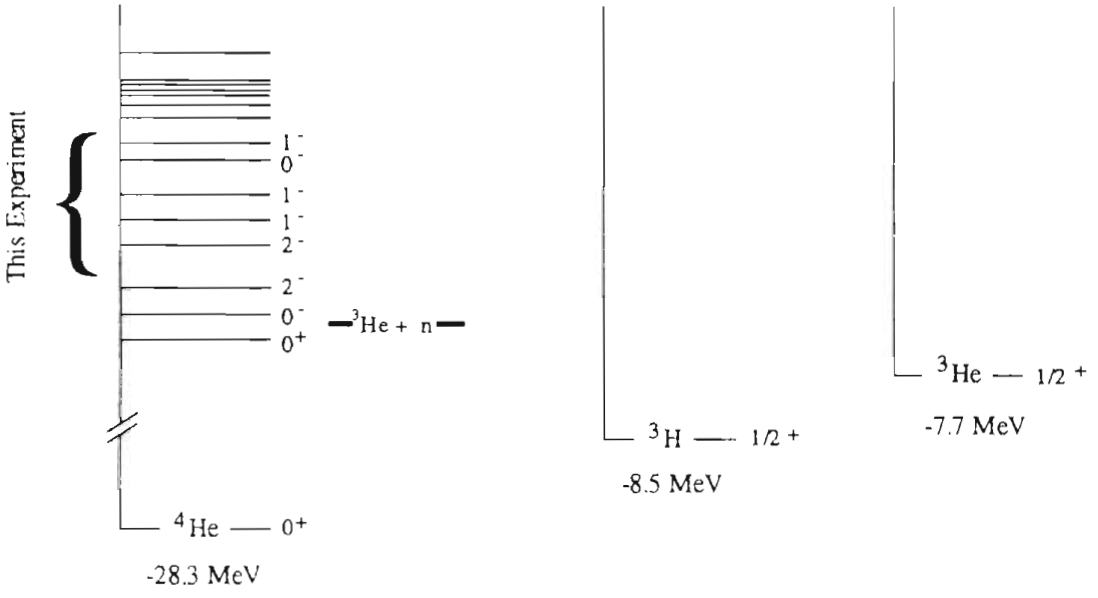

Figure 1.1: Energy levels of the three- and four-nucleon systems. Only systems that possess bound states are displayed. The experimental binding energies are shown at the bottom. The spin and parity assignments for several of the ^{4}He excited states are indicated [Til92]. A more detailed diagram of the ^{4}He levels is given in Fig. 2.2. There are no excited states in the 3N systems.

However, attempts to reproduce the underlying structure heavier systems (3N, 4N ...) in this fashion are hindered by the complexity and strength of the NN interaction. Numerically-exact solutions to the three- and four-body equations using "realistic", meson-exchange potentials have only become available in the last decade. When applied to the 3N system, results have revealed intriguing inadequacies concerning our knowledge of the NN force. For example, all "state-of-the-art" meson-exchange potentials underbind the 3N bound state by as much as 1 MeV [Bra88]. Similar results exist for the α particle as well, and there is strong evidence that the 4N *bound* system does not probe nucleon-nucleon dynamics in a manner different from the 3N system (see [Kam92]).

There is one fundamental difference between the three- and four-nucleon systems. Whereas the former has none, the latter system is known to possess several excited states (Fig. 1.1).

These excited states have long been used as a testing ground for several micro-

scopic approaches to scattering theory. Examples are the resonating group model (e.g. [Hac71] and [Hof81]), and the nuclear shell model ([DS66] and [Zhe93]). Exact four-body calculations of the excited states utilizing realistic potentials are only now in their infancy. We expect that the continuum states will display more sensitivity than the ground state to fundamental differences between the various meson-exchange models.

Obviously, we need to compare the theoretical results to experiment. The four-body system is attractive because it can be reached through a variety of two-body channels (n-^{3}He p-^{3}H, d-D, ...). Each of these two-body channels has at least one spin-degree of freedom, making a variety of polarization measurements possible. Polarization observables are more sensitive to the angular momentum of scattering states than cross sections. However, nuclear data in the ^{4}He system with *both* polarized beam and polarized target are limited to one experiment. In 1966 Passell and Schermer measured the transmission of polarized thermal neutrons through a polarized ^{3}He target [Pas66]. At this low energy, the cross section is completely insensitive to all but one resonance in the ^{4}He compound nucleus. In contrast, the present experiment covers the excitation energy range where a number of broad, negative-parity levels are believed to exist (see Fig. 1.1).

The present results are compared to the ^{4}He resonant structure recently obtained from a comprehensive R-matrix analysis of nearly all $A = 4$ scattering and reaction experiments in the 20–30 MeV excitation energy range [Hal]. Comparison is also made with two sets of n-^{3}He phase-shift analyses [Lis76, Jan88] and a microscopic resonating group model calculation of the ^{3}He system [Hof].

1.2 The Polarized ^{3}He Target

Polarized targets of ^{3}He are important in a variety of sub-atomic physics experiments. The impetus behind this is the fact that polarized ^{3}He closely approximates a polarized neutron [Fri90]. Polarized ^{3}He targets are thus used in a number of experiments that propose to measure fundamental properties of the neutron, such as its electric and magnetic form factors. Without exception, the targets used are polarized gaseous targets.

Since 1963, when Colgrove, Schearer and Walters first polarized ^{3}He gas at a

pressure of 1 mbar [Col63], considerable progress has been made in applying their technique to higher sample pressures. The technique developed by Colgrove *et al.* involves exciting ^{3}He atoms from the 1^1S_0 atomic ground state to the 2^3S_1 metastable state. From there, circularly polarized laser light is used to optically pump atoms in the 2^3S_1 states to the 2^3P_0 atomic levels.[2] The laser light is transmitted along a weak applied magnetic field that breaks the degeneracy of the atomic Zeeman levels. The optical pumping process must satisfy the selection rule $\Delta m = +1$ for right-handed circularly polarized light, or $\Delta m = -1$ if the light is polarized in the opposite sense. m labels the z-projection of the hyperfine substates. This means that only $^3S_1$ atoms with $m = -1/2$ or $-3/2$ are pumped to the $^3P_0$ level.[3] The $^3P_1$ atoms decay back to all the 2^3S_1 metastable states with equal probabilities. In this manner, atoms are preferentially transferred from the low magnetic substates ($m = -1/2,\ -3/2$) and placed in the high substates ($m = +1/2,\ +3/2$). The ^{3}He gas becomes nuclear-spin polarized as a result. Polarizations of 50–60% are typically achieved.

An alternative, though closely related, method was developed several years later at Princeton and Harvard [Chu87]. In this method, a small amount (a few mbar) of rubidium vapor is added to the ^{3}He gas and is optically pumped in a manner similar to that prescribed above. Dipole-dipole interactions transfer the nuclear polarization of the Rb to the ^{3}He nuclei during collisions between the two species.

Either method—pumping of the ^{3}He metastable state or "Rb spin-exchange"—requires a powerful laser to provide the necessary pumping photons. The density of the ^{3}He gas that is to be polarized is limited by the power of available lasers. Considerable progress has been made in this area in recent years. Still, present-day gas targets are limited to densities equivalent to about 10 bar of pressure at room temperature. We shall see in the next section that these relatively-low densities make polarized ^{3}He gas targets unsuitable for this neutron-transmission experiment.

In contrast, the condensed phases of ^{3}He correspond to about 1000 bar of room-temperature gas. The target described herein makes use of the static, or "brute-force" method to polarize solid ^{3}He. The ^{3}He sample is cooled to a low temperature ($\sim$ 0.01 K), and a large magnetic field (7 Tesla) is applied to polarize the nuclear spins. At these temperatures, liquid ^{3}He is governed by Fermi-Dirac statistics, and

[2] For each $(2s+1)L_j$ atomic state, there are $(2I+1)(2j+1)$ hyperfine substates. I is the nuclear spin of ^{3}He.

[3] Or atoms with $m = +1/2,\ +3/2$, depending on the "handedness" of the laser beam.

the maximum nuclear polarization that can be achieved with present-day apparatus is only a few percent. However, solid ^{3}He is a nuclear paramagnet, and in thermal equilibrium at the given temperature and field (0.01 K, 7 T), a polarization of nearly 45% is obtained.

1.3 Experimental Method

We briefly summarize the experimental method used to make these measurements. We do this primarily to illustrate the need for a dense target. Based upon the rough estimates to follow, we shall see that only the solid target developed for this project is suitable for these measurements.

We project a beam of polarized neutrons at the polarized ^{3}He target and count the number that make it through to a detector located on the other side. The beam is attenuated by the target in a manner that depends exponentially on the total cross section and the areal density of the target (target density times length). If N_0 is the incident number of neutrons, the number counted will be

$$N^{\pm} = N_0^{\pm} e^{-\sigma_{tot}^{\pm}\tau}, \tag{1.1}$$

where τ is the areal density. The $\pm$ superscripts are used to indicate whether the beam and target spins are oriented parallel (+) or antiparallel (−) to one another. As we will see in Chapter 2, the nuclear force is spin-dependent. The spin-dependence of the cross section can be determined by reversing the neutron spin and comparing the resulting attenuation to the attenuation prior to spin-reversal. It can be shown that measuring the "spin-spin" cross section σ_{ss} in this manner is subject to an error $\delta\sigma_{ss}$ that depends on the number of counted neutrons, the polarizations of the beam and target (P_b and P_t) and the areal density τ:

$$\delta\sigma_{ss} = \frac{1}{\sqrt{2N}P_b P_t \tau}. \tag{1.2}$$

Here N is the average of N^+ and N^-, and the factor of two indicates that we need to use both spin states of the neutron. The number of counts (per spin state) needed to resolve σ_{ss} to within 5% of its value is then

$$N_{5\%} = \frac{1}{2\left(0.05\sigma_{ss}P_b P_t \tau\right)^2}. \tag{1.3}$$

This indicates that the figure-of-merit for comparing targets in these experiments should be $(P_t\tau)^2$. Obviously, it is advisable to use a well-polarized *thick* target.

For example, we expect σ_{ss} in our experiment to be of order 0.5×10^{-24} cm^2 (1/2 b). Assuming 50% polarization of the neutron beam, and the parameters of the solid target used in the present work ($P_t = 37\%$, $\tau = 4.3 \times 10^{22}$ atoms/cm^2) we require

$$N_{5\%}(solid) = 1 \times 10^7. \tag{1.4}$$

On the other hand, to perform the experiment with the TRIUMF gas target (9 bar, 8 cm, 55% polarization) [Lar91] would require

$$N_{5\%}(gas) = 3 \times 10^9. \tag{1.5}$$

Use of the solid target reduces the length of the experiment by a factor of 300.

For some applications this may not be a significant savings in time. But the luminosities of polarized neutron beams are usually low, particularly in the few MeV energy region. An accurate measurement of the spin-spin asymmetry can often require several hours. For example, using the polarized solid ^{3}He target the measurement at 1.94 MeV required 18 hours of beam time (see Chapter 5 for additional details). An equivalent measurement using the TRIUMF gas target would take about 225 days!

The discussion we have just presented is only meant to outline the experiment described in this dissertation. More details — theoretical and experimental — are given in the five chapters that follow.

Chapter 2 Derivation of the formalism for describing the spin-dependent total cross section. Detailed calculations for the scattering of polarized neutrons from polarized ^{3}He.

Chapter 3 Technical description of the TUNL polarized ^{3}He target and a review of the low-temperature properties of solid ^{3}He.

Chapter 4 Details of the production and detection of the polarized neutron beam.

Chapter 5 Description of the experimental procedure and data analysis. Presentation of the findings for the experiment and comparison to various phase-shift predictions.

Chapter 6 Summary of the work.

Appendix A The method of determining the polarization of the neutron beam.

Chapter 2

Theory

2.1 Polarization Formalism

Consider a collection of identical particles, each with nuclear spin I. There are $(2I+1)$ possible projections that each spin may make with regard to a given axis. We say that each particle possesses $(2I+1)$ "magnetic" substates. The substates are labeled as m and can take values

$$m = -I, -I+1, \ldots, I-1, I. \tag{2.1}$$

We use the word *polarization* to indicate that, on average, the spins are oriented in some nonrandom fashion. That is, the $(2I+1)$ substates are not equally populated.

If we expand the particle's (normalized) wave function in terms of its magnetic substates,

$$\begin{aligned} |\psi\rangle &= \sum_{m=-I}^{+I} \langle m|\psi\rangle |m\rangle \\ &= \sum_{m=-I}^{+I} a_m |m\rangle, \end{aligned} \tag{2.2}$$

then $|a_m|^2$ may be interpreted as being the probability of finding the particle in the m^{th} substate. An ensemble of particles is then described by a probability or *density* matrix ρ, whose elements are

$$\rho_{mm'} = a_m a^*_{m'}. \tag{2.3}$$

Typically, the polarization of nuclei is accomplished by a process whose hamiltonian possesses cylindrical symmetry. If we measure the spin-projection against this symmetry axis (the "spin-axis") then the off-diagonal elements of the density matrix vanish. As an example, consider the case of nuclei that are subjected to the field of a powerful solenoidal magnet. The interaction between the field $\vec{B}$ and the magnetic moment $\vec{\mu}$ that arises due to the nuclear spins is given by

$$\begin{aligned} \mathcal{H} &= -\vec{B}\cdot\vec{\mu} \\ &= -\mu_N g m B_z, \end{aligned} \tag{2.4}$$

where g is the gyromagnetic moment of the nuclear species and μ_N is the nuclear magneton, $\mu_N = 3.15 \times 10^{-8}$ eV/T. This interaction breaks the degeneracy of the $|Im\rangle$ substates, m being the projection of the nuclear spins upon the solenoid's z axis. In order to minimize the energy, the magnetic moments will try to align themselves along the magnetic field. In thermal equilibrium at temperature T, the population of the m^{th} substate (i.e. the diagonal matrix element ρ_{mm}) is given by Boltzmann statistics to be

$$\rho_{mm} = \frac{\exp(-\mu_N g m B_z/kT)}{\sum_{m=-I}^{+I} \exp(-\mu_N g m B_z/kT)}. \tag{2.5}$$

This is the basis of the *brute-force* or *static* technique of polarization — the sample is subjected to a magnetic field and is then cooled to a sufficiently low temperature to produce a non-uniform population distribution among the various magnetic substates.

Unfortunately, a number of equivalent methods exist in the literature to characterize polarized beams and targets. We will follow the suggestion of the Madison convention and use the set of irreducible spherical tensors t_{KQ}. These tensors may be defined in terms of the density matrices as

$$t_{KQ}(I) = \hat{I}\sum_{m}(-1)^{I-m}\langle IIm' - m|KQ\rangle\rho_{mm'}(I), \tag{2.6}$$

where $\hat{I}$ means $\sqrt{2I+1}$. With this definition, t_{00} is equal to one. The advantage of the t_{KQ} is their behavior under rotational transformations. Let us again consider the case of cylindrical symmetry and use the axis of symmetry as the z axis. It is easy to see that the spin tensors calculated in this coordinate system, $\tilde{t}_{KQ}$, vanish

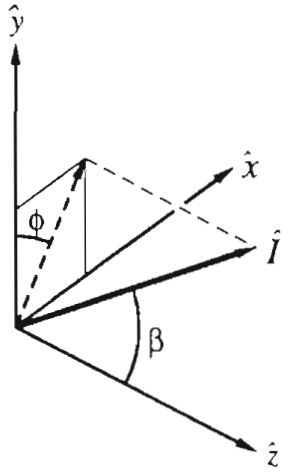

Figure 2.1: The coordinate system for the Madison convention. Here, $\hat{z}$ is parallel to the direction of the beam, $\vec{k}$. The $\hat{y}$-axis is along $\vec{k} \times \vec{k}'$ ($\vec{k}'$ is the direction of the scattered beam), and $\hat{x}$ is chosen so as to make a right-handed coordinate system. The spin-axis $\hat{I}$ is that axis which diagonalizes the spherical tensor $\tilde{t}_{KQ}$.

unless $Q = 0$. Additionally, the $Q = 0$ elements are real quantities. The spin tensors calculated in a different coordinate system (say, one in which the z axis is along the beam direction) can be expressed in terms of the $\tilde{t}_{K0}$ by the rotation

$$\begin{aligned} t_{KQ}(I) &= \sqrt{\frac{4\pi}{2K+1}} Y_K^Q(\beta_I, \phi_I) \tilde{t}_{K0}(I) \\ &= C_{KQ}(\beta_I, \phi_I) \tilde{t}_{K0}(I), \end{aligned} \tag{2.7}$$

where β_I and ϕ_I are the polar and azimuthal angles that the spin-axis makes in the new coordinate system (see Fig. 2.1) and $Y_K^Q(\beta_I, \phi_I)$ is a normalized spherical harmonic [Bri71].

Despite the elegance of the spherical tensors, it can probably be said that most of us live in a Cartesian world. It is very common for experimentalists to speak of "vector" or "tensor" polarizations with respect to the y or z axes. I will be guilty of this fault myself when it is time to discuss the polarization of the charged-particle beam in Chapter 4. The connection between the spherical tensors and their Cartesian cousins is listed below. Since we will primarily be discussing protons, neutrons and deuterons in this thesis, the list is limited to spin-1/2 and spin-1 particles. For spin-1 particles we

have

$$t_{10} = \sqrt{\frac{3}{2}}P_z \qquad (2.8)$$
$$t_{11} = -\frac{\sqrt{3}}{2}(P_x + iP_y)$$
$$t_{1-1} = +\frac{\sqrt{3}}{2}(P_x - iP_y)$$
$$t_{20} = \frac{1}{\sqrt{2}}P_{zz}$$
$$t_{21} = -\frac{1}{\sqrt{3}}(P_{xz} + iP_{yz})$$
$$t_{2-1} = +\frac{1}{\sqrt{3}}(P_{xz} - iP_{yz})$$
$$t_{22} = \frac{1}{2\sqrt{3}}(P_{xx} - P_{yy} + 2iP_{xy})$$
$$t_{2-2} = \frac{1}{2\sqrt{3}}(P_{xx} - P_{yy} - 2iP_{xy})$$

$$P_x = -\frac{1}{\sqrt{3}}(t_{11} - t_{1-1}) \qquad (2.9)$$
$$P_y = \frac{i}{\sqrt{3}}(t_{11} + t_{1-1})$$
$$P_z = \sqrt{\frac{2}{3}}t_{10}$$
$$P_{xx} = \frac{\sqrt{3}}{2}(t_{22} + t_{2-2}) - \frac{1}{\sqrt{2}}t_{20}$$
$$P_{yy} = -\frac{\sqrt{3}}{2}(t_{22} + t_{2-2}) - \frac{1}{\sqrt{2}}t_{20}$$
$$P_{zz} = \sqrt{2}t_{20}$$
$$P_{xy} = P_{yx} = -\frac{i\sqrt{3}}{2}(t_{22} - t_{2-2})$$
$$P_{xz} = P_{zx} = -\frac{\sqrt{3}}{2}(t_{21} - t_{2-1})$$
$$P_{yz} = P_{zy} = \frac{i\sqrt{3}}{2}(t_{21} + t_{2-1})$$

$$\text{with} \quad P_{xx} + P_{yy} + P_{zz} = 0$$

The list is shorter for spin-1/2 particles:

$$t_{10} = P_z \qquad (2.10)$$
$$t_{11} = -\frac{1}{\sqrt{2}}(P_x + iP_y)$$
$$t_{1-1} = +\frac{1}{\sqrt{2}}(P_x - iP_y)$$

$$P_x = -\frac{1}{\sqrt{2}}(t_{11} - t_{1-1}) \qquad (2.11)$$
$$P_y = \frac{i}{\sqrt{2}}(t_{11} + t_{1-1})$$
$$P_z = t_{10}$$

Polarization described by rank-1 tensors ($K = 1$) is called *vector* polarization, whereas *tensor* polarization refers to higher-orders of t_{KQ}[1]. Beams or targets of spin-1/2 particles can only possess vector polarization (i.e. P_x, P_y, or P_z). However, an ensemble of deuterons can be either vector or tensor polarized, or both at the same

[1] In some parts of the literature, it is common to reserve the term 'polarization' for the odd-rank t_{KQ} and to use 'alignment' to indicate the even-ranks.

time. The difference between vector and tensor polarization be summarized in the following manner. Vector polarization indicates that there is a preferred *direction* for the spin. Tensor polarization says that there is a preferred *axis*. If $N_{+,0,-}$ are the fractional populations for the $m = +1, 0, -1$ magnetic substates of an ensemble of deuterons (measured with respect to the z axis), then

$$P_z = N_+ - N_- \tag{2.12}$$

while

$$P_{zz} = 1 - 3N_0. \tag{2.13}$$

In this particular case, the tensor polarization only depends on the population of the $m = 0$ substate. The $m = +1$ and $m = -1$ may (or may not) have the same populations as one another, so that the vector polarization may be zero or non-zero.

In this dissertation we will most often use P_p, P_d, and P_n to represent the *vector* polarization of the proton, deuteron, and neutron beams, respectively. Likewise P_3 will be used to indicate the vector polarization of the ^{3}He target. In case of the deuteron beam, P_{dd} will refer to its *tensor* polarization. In analogy with the $\hat{t}_{K0}$ discussed previously, these polarizations are measured with respect to that spin-quantization axis which diagonalizes the corresponding t_{KQ}. In the case of a charged-particle beam, this axis is defined by the sextupole magnets used in the Polarized Ion Source. A Wien filter is used to rotate this "spin-axis" so that (at the location of the polarized target) it is perpendicular to the beam momentum. See Section 4.1.1 for additional details. A 7 Tesla superconducting magnet defines the polarized target's spin-axis (Chapter 3).

2.2 Nuclear Scattering Theory

In the following sections we present an overview to the scattering of nuclear particles. Our treatment will be brief since the topic is discussed in nearly all introductory textbooks for nuclear physics. For additional information, the reader is recommended Blatt and Weisskopf [Bla52b] and Preston [Pre62] for their pedagogical approach to the subject, as well as Wu and Ohmura [Wu62] for a more detailed treatment. The topic of polarization observables in nuclear scattering is covered by Satchler [Sat83].

2.2.1 The Scattering of Spinless Particles

In any treatment of nuclear scattering, it is advisable to begin with a simple example—the elastic scattering between two spinless particles due to a central potential. Because the potential is only a function of the radial distance between the particles, $V = V(r)$, their relative orbital angular momentum ℓ is conserved. Non-central forces are known to exist which mix states of orbital angular momentum. However, it is useful to treat these non-central forces as "perturbative" additions to $V(r)$ and retain the states of definite ℓ as the eigenstates of the total wave function.

In the asymptotic region, the wave function for a particle in the incident (unscattered) beam assumes the free-particle solution to Schödinger's equation. Hence, the incident beam is described as a plane wave $e^{i\vec{k}\cdot\vec{r}}$ that propagates in a direction that we choose to call the z axis,

$$\begin{aligned} \psi_{inc} &= e^{i\vec{k}\cdot\vec{r}} \\ &= e^{ikr\cos\theta} \end{aligned} \tag{2.14}$$

where k is the center-of-mass wave number,

$$k = \sqrt{\frac{2\mu E}{\hbar^2}}. \tag{2.15}$$

Expanding Eq. (2.14) into partial waves, one obtains

$$\begin{aligned} \psi_{inc} &= \sum_{\ell=0}^{\infty} \sum_{m=-\ell}^{m=\ell} A_{\ell m} j_\ell(kr) Y_\ell^m(\theta,\phi) \\ &= \sum_{\ell=0}^{\infty} A_{\ell 0} j_\ell(kr) Y_\ell^0(\theta,\phi) \end{aligned} \tag{2.16}$$

Here $j_\ell(kr)$ is a regular spherical Bessel function, while $Y_\ell^m(\theta,\phi)$ is a normalized spherical harmonic. Since there is no azimuthal dependence in our potential $V(r)$, only the $m = 0$ terms appear in the partial-wave expansion. Note that the right side of Eq. (2.16) is exactly the result one obtains by solving the free-particle Schödinger equation in spherical coordinates using separation of variables. The expansion coefficients can be determined by making use of the orthogonality of the spherical harmonics.

Next, we can substitute the relation between Y_ℓ^0 and the Legendre polynomials $P_\ell(\cos\theta)$,

$$Y_\ell^0(\theta,\phi) = \sqrt{\frac{2\ell+1}{4\pi}} P_\ell(\cos\theta), \tag{2.17}$$

and the asymptotic form of $j_\ell(kr)$,

$$j_\ell(kr) = -\frac{1}{2ikr}\left[e^{-i(kr-\ell\pi/2)} - e^{+i(kr-\ell\pi/2)}\right], \tag{2.18}$$

into 2.16 and write

$$\psi_{inc} \simeq -\frac{1}{2ik}\sum_{\ell=0}^{\infty} i^\ell \sqrt{\frac{2\ell+1}{4\pi}}\left[\frac{e^{-i(kr-\ell\pi/2)}}{r} - \frac{e^{+i(kr-\ell\pi/2)}}{r}\right] P_\ell(\cos\theta). \tag{2.19}$$

The two terms in the brackets of Eq. (2.19) indicate that our incident plane wave can be described as the superposition of incoming and outgoing spherical waves.

The effect of the potential $V(r)$ will be to modify the outgoing part of Eq. (2.19), so that the total wave function (*incident + scattered*) in the asymptotic region is

$$\psi_{tot} \simeq -\frac{1}{2ik}\sum_{\ell=0}^{\infty} i^\ell \sqrt{\frac{2\ell+1}{4\pi}}\left[\frac{e^{-i(kr-\ell\pi/2)}}{r} - S_\ell(k)\frac{e^{+i(kr-\ell\pi/2)}}{r}\right] P_\ell(\cos\theta), \tag{2.20}$$

subject to the flux-conservation condition

$$|S_\ell(k)|^2 = 1. \tag{2.21}$$

This unitarity property of the S factor allows it to be written in the form

$$S_\ell(k) = e^{2i\delta_\ell(k)}. \tag{2.22}$$

This means that the scattering potential only changes the *phase* of the outgoing wave (δ_ℓ is called the *phase shift*):

$$\psi_{tot} = -\frac{1}{2ik}\sum_{\ell=0}^{\infty} i^\ell \sqrt{\frac{2\ell+1}{4\pi}} P_\ell(\cos\theta)\left[\frac{e^{-i(kr-\ell\pi/2)}}{r} - \frac{e^{+i(kr-\ell\pi/2+2\delta_\ell)}}{r}\right]. \tag{2.23}$$

Inelastic scattering processes will occur if the potential has an imaginary component. In this event, it is necessary to include an imaginary component to the phase shift, so that

$$S_\ell = \eta_\ell e^{2i\delta_\ell}. \tag{2.24}$$

η_ℓ is referred to as the inelastic parameter.

We can re-write Eq. (2.23) so that it has the intuitive form (*incident plane wave + scattered spherical wave*):

$$\begin{aligned}\psi_{tot} &= e^{i\vec{k}\cdot\vec{r}} + \sum_\ell \frac{2\ell+1}{2ik} i^\ell \left[S_\ell - 1\right] \frac{e^{ikr}}{r} P_\ell(\cos\theta) \\ &= e^{i\vec{k}\cdot\vec{r}} + f(\theta)\frac{e^{ikr}}{r}. \end{aligned} \tag{2.25}$$

The *scattering amplitude* $f(\theta)$ is a function of the polar angle because, in general, the scattered wave will not be spherically symmetric. The flux of particles that scatter into the solid angle $d\Omega$ (normalized to the incident flux of particles) is a measure of the differential cross section $d\sigma/d\Omega$. In terms of the scattering amplitude,

$$\frac{d\sigma}{d\Omega} = |f(\theta)|^2. \tag{2.26}$$

The total cross section can be obtained by integrating Eq. (2.26). An alternative method is provided by the *optical theorem*, which relates the total cross section to the imaginary part of the zero degree (or *forward*) scattering amplitude:[2]

$$\sigma_{tot} = \frac{4\pi}{k} \mathrm{Im}\, f(0^\circ). \tag{2.27}$$

The optical theorem states that the total cross section can be determined by measuring the flux of particles that are not scattered by the potential $V(r)$. It says nothing about where the scattered particles go.

2.2.2 The Scattering of Particles with Spin

If either the particles in the beam or particles in the target have an intrinsic (spin) angular momentum I, the nuclear Hamiltonian may contain non-central forces. As a result the orbital angular momentum ℓ is no longer a conserved quantity. The correct integral of motion is now the total angular momentum J, defined to be

$$\begin{aligned}\vec{J} &= \vec{\ell} + (\vec{I}_a + \vec{I}_A) \\ &= \vec{\ell} + \vec{s}. \end{aligned} \tag{2.28}$$

[2]See Section N in Wu and Ohmura [Wu62] for a derivation of the optical theorem.

Here I_a (I_A) is the spin of the beam (target), and s is called the channel spin. It should be noted that the angular momenta can be coupled in an order different than Eq. (2.28). We choose the channel-spin representation because it is standard in most discussions of few-nucleon systems.

Now the S factor in Eq. (2.20) becomes the *S matrix*, whose elements describe transitions from an initial state with quantum numbers (J, ℓ, s) to a final state with quantum numbers (J, ℓ', s'). The scattering amplitude now includes summations over all initial and final quantum numbers, and we must specify the z components of the initial and final spins m_a, m_A, m'_a, and m'_A:

$$f^{m_a m_A}_{m'_a m'_A}(\theta,\phi) = \frac{\sqrt{4\pi}}{2ik} \sum_{\substack{J,\ell,s \\ \ell',s'}} \hat{\ell}\langle I_A I_a m_A m_a | s m_s\rangle \langle \ell s 0 m_s | J m_s\rangle \times \langle I_A I_a m'_A m'_a | s' m'_s\rangle \langle \ell' s'\, m_s - m_{s'}\, m_{s'} | J m_s\rangle \times \left[S^J_{\ell s,\ell' s'} - \delta_{\ell,\ell'}\delta_{s,s'}\right] Y_{\ell'}^{m_s - m_{s'}}(\theta,\phi). \quad (2.29)$$

See Satchler [Sat83] for additional details.

2.2.3 Total Cross Section for Polarized Target—Polarized Beam

There is an analog to the optical theorem given in Eq. (2.27) that may be used to determine the total cross section whenever one or both of the particles in the initial state are polarized. The generalized, spin-dependent optical theorem is [Phi63]

$$\sigma_{tot} = \mathrm{Im}\left\{4\pi\lambda \sum_{\substack{m_A m_a \\ m'_A m'_a}} \rho_{m_A m'_A}\rho_{m_a m'_a} f^{m'_A m'_a}_{m_A m_a}(0^\circ)\right\} \quad (2.30)$$

where $\rho_{m_A m'_A}$ and $\rho_{m_a m'_a}$ are the density matrices for the target and beam, respectively. Equation 2.6 can be inverted to write

$$\rho_{mm'}(I) = \hat{I}\sum_{KQ}(-1)^{I-m} t_{KQ}(I)\langle I I m' - m | K Q\rangle. \quad (2.31)$$

Substitution of Eq. 2.29 (with $\theta = \phi = 0^\circ$) and Eq. 2.31 into Eq. (2.30) yields the following formula for the polarized beam—polarized target total cross section

$$\sigma_{tot} = \mathrm{Re}\left\{2\pi\lambda^2 \sum_{\substack{J\ell\ell' \\ ss'}} \sum_{\substack{KQ \\ kq}} \sum_{\substack{m_A m_a \\ m'_A m'_a}} (-1)^{I_A + I_a - m_A - m_a} \hat{\ell}\hat{\ell}' \hat{I}_A^{-1} \hat{I}_a^{-1}\right.$$

$$\times \langle I_A I_A m'_A - m_A | KQ \rangle \langle I_a I_a m'_a - m_a | kq \rangle \langle I_A I_a m_A m_a | s m_s \rangle$$
$$\times \langle \ell s 0 m_s | J m_s \rangle \langle \ell' s' m_s - m_{s'} m_{s'} | J m_s \rangle \langle I_A I_a m'_A m'_a | s' m_{s'} \rangle$$
$$\times t_{KQ}(I_A) t_{kq}(I_a) \left[\delta_{\ell'\ell} \delta_{s's} - S^J_{\ell s \ell' s'} \right] \Bigg\}. \qquad (2.32)$$

Equation (2.32) can be reduced to a less cumbersome form by the use of standard angular momentum coupling relations [Bri71]. The final form contains no summation over the magnetic quantum numbers m_α. The total cross section is expressed as an expansion in terms of the polarization tensors calculated in the "spin-axis" coordinate system,

$$\sigma_{tot} = \sum_{kK} \sigma_{kK} \tilde{t}_{K0}(I_A) \tilde{t}_{k0}(I_a) \qquad (2.33)$$

where

$$\sigma_{kK} = \mathrm{Re} \Bigg\{ 2\pi \lambda^2 \sum_{\substack{J \ell \ell' \\ s s'}} \sum_q \frac{2J+1}{(2I_a+1)(2I_A+1)}$$
$$\times F_q(J \ell s \ell' s') \left[\delta_{\ell\ell'} \delta_{ss'} - S^J_{\ell s \ell' s'} \right] C^*_{Kq}(\beta_A, \phi_A) C_{kq}(\beta_a, \phi_a) \Bigg\} \qquad (2.34)$$

and

$$F_q(J \ell s \ell' s') = \sum_\Lambda (-1)^K (-1)^{(J-s')} \hat{\Lambda} \hat{I}_a \hat{I}_A \hat{\ell} \hat{\ell}' \hat{s} \hat{s}' \hat{k} \langle \Lambda k 0 q | K q \rangle$$
$$\times \langle \ell' \ell 00 | \Lambda 0 \rangle W(s' s \ell' \ell; \Lambda J) \begin{Bmatrix} I_a & s & I_A \\ I_a & s' & I_A \\ k & \Lambda & K \end{Bmatrix}. \qquad (2.35)$$

Here $W(s's\ell'\ell;\Lambda J)$ is a Racah angular momentum coupling coefficient. The expression in the curly brackets is a 9-j symbol [Bri71], and $\vec{\Lambda}$ is the orbital angular momentum transfer $\vec{\ell}' - \vec{\ell}$.

It is worth mentioning that this formula applies to the scattering of any nuclear particles, regardless of their charges or their spins. In this thesis we describe the experimental determination of σ_{tot} for one particular system—neutrons incident on ^{3}He. We will concentrate on spin-1/2–spin-1/2 scattering, and the words "projectile" and "neutron" may be used interchangeably.

2.2.4 Partial-Wave Decomposition for Spin-1/2 Particles

If both the target and projectile are spin-1/2 particles, the expression for the total cross section can be greatly simplified. The spin tensors $\tilde{t}_{K0}(1/2)$ are identically zero except for the $K = 0$ and $K = 1$ components. Therefore, the expansion in Eq. (2.32) contains only four terms,

$$\sigma_{tot} = \sigma_{00} + \sigma_{01}\tilde{t}_{10}(I_A) + \sigma_{10}\tilde{t}_{10}(I_a) + \sigma_{11}\tilde{t}_{10}(I_A)\tilde{t}_{10}(I_a). \tag{2.36}$$

The middle two terms are parity violating contributions to the total cross section and may be ignored in the present treatment. The first term, σ_{00}, is simply the total cross section for the scattering of unpolarized beam and target, and will henceforth be written as σ_0. σ_{11} is the contribution to the total cross section that arises from spin-spin interactions and is sometimes called the *spin-spin* cross section. Since the polarization tensor for the beam (or target) $\tilde{t}_{10}$ changes sign whenever the spin is reversed, the spin-spin cross section can be determined from the total cross-section difference $\Delta\sigma$:

$$\begin{aligned} \Delta\sigma &= \frac{\sigma_{tot}(++) - \sigma_{tot}(+-)}{\tilde{t}_{10}(I_A)\tilde{t}_{10}(I_a)} \\ &= \frac{2\sigma_{11}}{\tilde{t}_{10}(I_A)\tilde{t}_{10}(I_a)}. \end{aligned} \tag{2.37}$$

The $(+)$ and $(-)$ signs indicate the relative orientation of the beam and target spins with respect to their respective spin axes (e.g. "+" means spin-*up etc.*). Experimentally, $\Delta\sigma$ is determined from the "spin-spin asymmetry" ε_{ss}. To measure ε_{ss}, polarized neutrons are transmitted through a polarized target. The neutron spin (or target spin) is periodically reversed and the corresponding 0° yields are compared according to

$$\begin{aligned} \varepsilon_{ss} &= \frac{\mathrm{N}(++) - \mathrm{N}(+-)}{\mathrm{N}(++) + \mathrm{N}(+-)} \\ &= -\tanh\left[\frac{1}{2}\Delta\sigma\,\tau_A\,\tilde{t}_a\,\tilde{t}_A\right]. \end{aligned} \tag{2.38}$$

Here $\mathrm{N}(++)$ is the neutron yield at 0°, and $\mathrm{N}(+-)$ is the same yield after one of the spins has been reversed. τ_A is the areal density of the polarized target in units of atoms per barn.

Such experiments are usually performed with the beam and target spin axes parallel to one another. The most common spin geometries are those in which the spins are parallel (Longitudinal) or perpendicular (Transverse) to the incident beam direction. The corresponding $\Delta\sigma$'s can be pictorially represented in the following manner,

$$\Delta\sigma_L = \sigma_{tot}(\overrightarrow{\rightarrow}) - \sigma_{tot}(\overrightarrow{\leftarrow}) \tag{2.39}$$

$$\Delta\sigma_T = \sigma_{tot}(\uparrow\uparrow) - \sigma_{tot}(\uparrow\downarrow) \tag{2.40}$$

where it is understood that $\Delta\sigma_L$ and $\Delta\sigma_T$ are normalized to unit beam and target polarizations.

Both σ_0 and σ_{11} can be decomposed into their partial-wave contributions as follows. The cross section corresponding to the $(Jlsl's')$ S-matrix element is

$$\sigma(J\ell s\ell' s') = \mathrm{Re}\left\{2\pi\lambda^2 \frac{2J+1}{(2I_a+1)(2I_A+1)}\left[\delta_{\ell\ell'}\delta_{ss'} - S^J_{\ell s\ell' s'}\right]\right\}. \tag{2.41}$$

In general, these "partial-wave cross sections" make different contributions to the unpolarized and spin-spin total cross sections, and must be weighted according to the angular momentum coupling coefficients $F_q(J\ell s\ell' s')$. Substituting $k = K = 0$ into Eq. (2.35), we find $F_q = \delta_{\ell\ell'}\delta_{ss'}$ for all values of q and J, and one obtains the familiar result that the unpolarized total cross section is simply a coherent sum over the diagonal elements of the scattering matrix

$$\sigma_0 = \sum_{J\ell s} \sigma(J\ell s\ell s). \tag{2.42}$$

A similar result can be obtained directly from the optical theorem for unpolarized particles, Eq. (2.27).

One of the advantages of using the channel-spin representation is that the channel-spin is a conserved quantity in the forward elastic scattering amplitude[3] and so $F_q = 0$ whenever $s' \neq s$. The spin-spin cross section, however, does include contributions from the off-diagonal S-matrix elements that mix[4] orbital angular momenta ℓ and $\ell \pm 2$. Expressed in terms of the partial-wave cross sections, the spin-spin cross section is

$$\sigma_{11} = \sum_{J\ell\ell' s} \sigma(J\ell s\ell' s)\Big\{F_0(J\ell s\ell' s)\cos(\beta_A)\cos(\beta_a)$$

[3]This statement is not true for cases involving parity-violating contributions to the hamiltonian.
[4]Such terms are a consequence of the spin-dependent tensor force (see Eq. (2.47) below.

$$+\frac{1}{2}\left[F_{-1}(J\ell s\ell' s)+F_1(J\ell s\ell' s)\right]\sin(\beta_A)\sin(\beta_a)\cos(\phi_A-\phi_a)\Big\}, \quad (2.43)$$

where the explicit forms for $C_{1q}(\beta,\,\phi)$ in Eq. 2.35 have been substituted.

The longitudinal and transverse geometries correspond to $\beta_A = \beta_a = 0°$ and $\beta_A = \beta_a = 90°$, respectively, and so

$$\Delta\sigma_L = 2\sum_{J\ell\ell' s} F_0(J\ell s\ell' s)\sigma(J\ell s\ell' s) \quad (2.44)$$

and

$$\Delta\sigma_T = 2\sum_{J\ell\ell' s} F_1(J\ell s\ell' s)\sigma(J\ell s\ell' s) \quad (2.45)$$

since $F_{-1}(J\ell s\ell' s) = F_1(J\ell s\ell' s)$. Explicit values of F_0 and F_1 up to $l = 3$ are given in Table 2.1.

Equation 2.43 can be expressed in a form in which $\Delta\sigma_L$ and $\Delta\sigma_T$ serve as the longitudinal and transverse components of the spin-spin cross section:

$$\sigma_{11} = \frac{1}{2}\left[\Delta\sigma_L\cos(\beta_A)\cos(\beta_a)+\Delta\sigma_T\sin(\beta_A)\sin(\beta_a)\cos(\phi_A-\phi_a)\right]. \quad (2.46)$$

In order to fully determine the spin-spin cross section, we see that it is necessary to measure *two* quantities (in this notation, $\Delta\sigma_L$ and $\Delta\sigma_T$). To completely determine σ_{tot} (and therefore the forward part of the PCTRI[5] elastic scattering amplitude), we need to know a third quantity, the unpolarized cross section σ_0.

Since two measurements are necessary to determine σ_{11}, there must be two spin-dependent interactions which contribute to the total cross section. If we require the Hamiltonian to be invariant under rotation, reflection, and time reversal, the elastic scattering amplitude can be written [Oku58] as the sum of six independent terms, $\sum_{i=1}^{6} f_i P_i$. A common choice for the six operators P_i is [Sto94] (expressed in our notation):

$$\begin{aligned} P_1 &= 1, \\ P_2 &= \vec{I}_a\cdot\vec{I}_A, \\ P_3 &= S_{12} = 3(\vec{I}_a\cdot\hat{r})(\vec{I}_A\cdot\hat{r}) - (\vec{I}_a\cdot\vec{I}_A), \\ P_4 &= \vec{\ell}\cdot\vec{s}, \end{aligned} \quad (2.47)$$

[5] Parity Conserving-Time Reversal Invariant

$^{(2s+1)}\ell_J$	$F_0(J\ell s\ell s)$	$F_1(J\ell s\ell s)$
$^1S_0$	-1	-1
$^3S_1$	$\frac{1}{3}$	$\frac{1}{3}$
$^1P_1$	-1	-1
$^3P_0$	-1	1
$^3P_1$	1	0
$^3P_2$	$\frac{1}{5}$	$\frac{2}{5}$
$^1D_2$	-1	-1
$^3D_1$	$-\frac{1}{3}$	$\frac{2}{3}$
$^3D_2$	1	0
$^3D_3$	$\frac{1}{7}$	$\frac{3}{7}$
$^1F_3$	-1	-1
$^1F_3$	-1	-1
$^3F_2$	$-\frac{1}{5}$	$\frac{3}{5}$
$^3F_3$	1	0
$^3F_4$	$\frac{1}{9}$	$\frac{1}{3}$

$^{(2s+1)}\ell_J - ^{(2s+1)}\ell'_J$	$F_0(J\ell s\ell' s)$	$F_1(J\ell s\ell' s)$
$^3S_1 - {}^3D_1$	$\frac{2}{3}\sqrt{2}$	$-\frac{1}{3}\sqrt{2}$
$^3P_2 - {}^3F_2$	$\frac{2}{5}\sqrt{6}$	$-\frac{1}{5}\sqrt{6}$

Table 2.1: The angular momentum coupling coefficients $F_0(J\ell s\ell' s)$ and $F_1(J\ell s\ell' s)$ of Eq. (2.35) up to $\ell = 3$. The subscripts 0 and 1 correspond respectively to the longitudinal and transverse spin geometries. The coupling coefficients for mixed orbital angular momentum states $\ell' = \ell \pm 2$ are listed at the bottom.

$$P_5 = Q_{12} = \frac{1}{2}\left[(\vec{I}_a \cdot \vec{\ell})(\vec{I}_A \cdot \vec{\ell}) + (\vec{I}_A \cdot \vec{\ell})(\vec{I}_a \cdot \vec{\ell})\right],$$
$$P_6 = \frac{1}{2}(\vec{I}_a - \vec{I}_A) \cdot \vec{\ell}.$$

Here $\hat{r}$ is a unit vector that points from particle a to particle A. These operators are referred to as (top to bottom) the central, scalar (or spin-spin), tensor, spin-orbit, quadratic spin-orbit, and antisymmetric spin-orbit operators. Because the last three are functions of the orbital angular momentum, they do not contribute to the zero-degree elastic scattering amplitude.

We will now show that the remaining two spin-dependent interactions make separate contributions to the total cross section that can be written in terms of $\Delta\sigma_L$ and $\Delta\sigma_T$. Note that

$$\begin{aligned} \cos(\beta_A) &= \hat{k} \cdot \vec{I}_A \\ \cos(\beta_a) &= \hat{k} \cdot \vec{I}_a \end{aligned} \tag{2.48}$$

and

$$\begin{aligned} \sin(\beta_A)\sin(\beta_a)\cos(\phi_A - \phi_a) &= (\hat{k} \times \vec{I}_A) \cdot (\hat{k} \times \vec{I}_a) \\ &= (\vec{I}_A \cdot \vec{I}_a) - (\hat{k} \cdot \vec{I}_A)(\hat{k} \cdot \vec{I}_a), \end{aligned} \tag{2.49}$$

where $\hat{k}$ is a unit vector pointing in the direction of the beam (not to be confused with $\sqrt{2k+1}$). At 0° $\vec{k}$ and $\vec{r}$ are parallel. This allows us to write the spin-spin cross section as

$$\sigma_{11} = \frac{1}{2}\left[(\Delta\sigma_L - \Delta\sigma_T)(\hat{r} \cdot \vec{I}_A)(\hat{r} \cdot \vec{I}_a) + \Delta\sigma_T(\vec{I}_A \cdot \vec{I}_a)\right], \tag{2.50}$$

which is similar to the form written in Eq. (3) of Phillips [Phi63]. After some rearranging, we can write

$$\sigma_{11} = \sigma_{sc}(\vec{I}_A \cdot \vec{I}_a) + \sigma_t\left[3(\hat{r} \cdot \vec{I}_A)(\hat{r} \cdot \vec{I}_a) - (\vec{I}_A \cdot \vec{I}_a)\right], \tag{2.51}$$

where

$$\sigma_{sc} = \frac{1}{6}(\Delta\sigma_L + 2\Delta\sigma_T) \tag{2.52}$$

$$\sigma_t = \frac{1}{6}(\Delta\sigma_L - \Delta\sigma_T). \tag{2.53}$$

We see that the spin-dependent cross sections in Eq. (2.51) have the same form as the spin-spin and tensor interactions listed in Eq. (2.47). With experimental measurements of both $\Delta\sigma_L$ and $\Delta\sigma_T$ it is possible to determine the contributions that these two operators make to $f(0°)$.[6]

To aid in the following discussion of n–^{3}He scattering, we write the explicit forms of σ_0, $\Delta\sigma_L$ and $\Delta\sigma_T$ in terms of partial-wave cross sections up to $\ell = 1$.

$$\begin{aligned}\sigma_0 &= \sigma(^1S_0) + \sigma(^3S_1) + \sigma(^1P_1) \\ &+ \sigma(^3P_0) + \sigma(^3P_1) + \sigma(^3P_2)\end{aligned} \tag{2.54}$$

$$\begin{aligned}\Delta\sigma_L &= -2\sigma(^1S_0) + \frac{2}{3}\sigma(^3S_1) - 2\sigma(^1P_1) \\ &- 2\sigma(^3P_0) + 2\sigma(^3P_1) + \frac{2}{5}\sigma(^3P_2) + \frac{4}{3}\sqrt{2}\sigma(^3S_1 - {}^3D_1)\end{aligned} \tag{2.55}$$

and

$$\begin{aligned}\Delta\sigma_T &= -2\sigma(^1S_0) + \frac{2}{3}\sigma(^3S_1) - 2\sigma(^1P_1) \\ &+ 2\sigma(^3P_0) + \frac{4}{5}\sigma(^3P_2) - \frac{2}{3}\sqrt{2}\sigma(^3S_1 - {}^3D_1).\end{aligned} \tag{2.56}$$

Here $\sigma(^{2s+1}\ell_J)$ refers to the $\sigma(J\ell s\ell s)$ partial-wave cross section defined in Eq. (2.41). Extension of these formulas to include higher partial waves follows from Table 2.1. In Section 2.3.2 we shall discuss how this partial-wave decomposition may be used to extract information about the contributions of specific partial waves.

2.3 Calculation of $\Delta\sigma$ for n-^{3}He Scattering

The ^{4}He excited level scheme is shown in Fig. 2.2. This level scheme was obtained from a comprehensive, charge-independent R-matrix analysis of n-^{3}He, p-^{3}H and d-^{2}H scattering and reaction data [Hal]. A formal description of R-matrix theory is given by Vogt [Vog59].

The isospin-1 parameters for this level spectrum are taken from an analysis of p-^{3}He scattering data at proton enegies below 20 MeV. The validity of these parameters is checked by using them to calculate the n-^{3}H total cross section and S-wave

[6] See [Wil93a] for an alternative procedure that allows for the *direct* determination of either σ_{sc} or σ_t.

scattering lengths. Good agreement is found at all energies below 20 MeV (χ^2 per degree of freedom is 1.23) [Hal90].

The $T = 1$ parameters are then incorporated, essentially fixed, into a larger analysis of the ^{4}He data in which the isospin-0 parameters are allowed to vary. Each p-^{3}He energy eigenvalue E_λ is shifted by -0.64 MeV. This corresponds to the internal Coulomb energy difference ΔE_C between the ^{4}Li and ^{4}He systems. The reduced-width amplitudes γ_T for the p-^3H, p-^{3}He and n-^{3}He channels are constrained by the the isospin relations

$$\begin{aligned} \gamma_1(p,^3\mathrm{H}) &= \gamma_1(n,^3\mathrm{He}) = \frac{1}{\sqrt{2}}\gamma_1(p,^3\mathrm{He}) \\ \gamma_0(p,^3\mathrm{H}) &= -\gamma_0(n,^3\mathrm{He}) \end{aligned} \tag{2.57}$$

and are thus interrelated. Additionally, all three nucleon-trinucleon channels share the same channel radius of 4.9 fm.

The d-d channel (which is pure isospin-0) is given a different channel radius, 7.0 fm. However, to improve agreement with low-energy D$(d,p)^3$H and D$(d,n)^3$He reaction data, a small amount of isospin mixing is allowed by introducing small (but non-zero) values of $\gamma_1(d,d)$ in the ^{3}P channels [Hal91b].

Although the R-matrix fit to the 4652 data points with 87 free parameters is not yet complete, with χ^2 per degree of freedom about 4 [Hal91b], the ^{4}He levels obtained thus far are sufficiently stable to allow accurate calculations. The analysis finds evidence for a series of fifteen excited states lying 20 to 30 MeV above the ^{4}He ground state. They do not appear as sharp, well-isolated resonances but are instead broad, overlapping structures. It is felt that any accurate, theoretical description of the ^{4}He system must reproduce the positions and widths of these levels. Experimental determination of the states is hindered by the width of the levels and by the degree to which they overlap.

To investigate the sensitivity of the spin-spin cross section to the excited states of the α particle, we have calculated $\Delta\sigma_L$ and $\Delta\sigma_T$ for n-^{3}He scattering. The transmission of polarized neutrons through polarized ^{3}He has been measured previously [Pas66, Ben87]. Both experiments were performed using thermal neutrons and hence were only sensitive to S-wave scattering amplitudes. However, it is worth noting that the experiment of Paschell and Schermer [Pas66] was important in confirming that 100% of the ^{3}He$(n,p)^3$H reaction proceeds through the $^1S_0$ partial wave

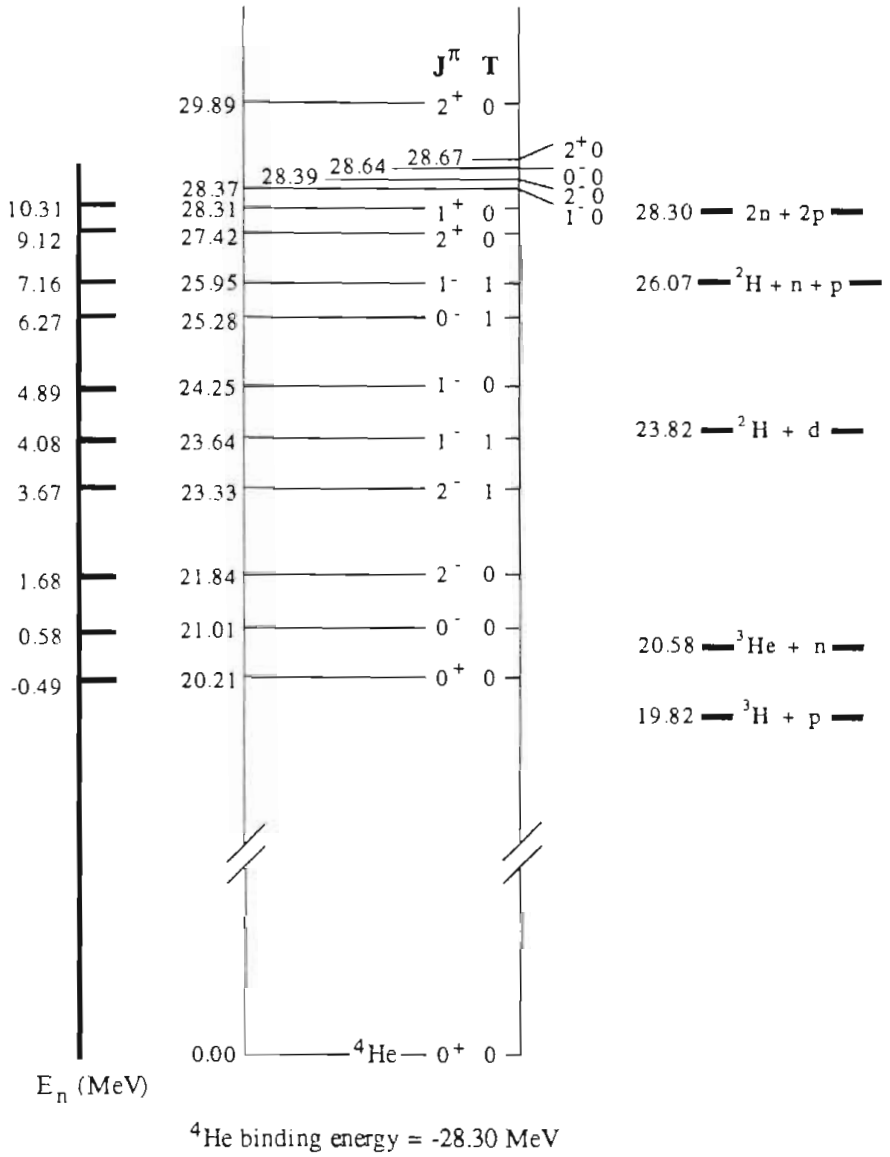

Figure 2.2: The level scheme of ^{4}He as determined by the R-matrix analysis of Hale *et al.* [Til92, Hal]. The vertical bar on the left marks the position of the levels in the n-^{3}He laboratory frame, and the positions of the two-, three- and four-body break-up thresholds are shown on the right.

Analysis	Energy Range (MeV)	ℓ_{max}	J_{max}
R-matrix	0.10 — 10.00	3	4
MCRGM	0.14 — 12.14	2	3
Lisowski PWA	1.00 — 23.70	2	3
Jany PWA	1.00 — 3.70	2	2

Table 2.2: Parameters describing the S-matrix elements used in the n-^{3}He cross section calculations.

at 0.11 eV. The experimental results presented in Chapter 5 probe the sensitivity of polarized neutron–polarized ^{3}He scattering to the P and D-wave amplitudes as well.

The S-matrix elements used in the calculations were obtained from four sources:

1. Hale's R-matrix analysis [Hal];
2. the single-energy partial-wave analysis of Lisowski *et al.* [Lis76] (Lisowski PWA);
3. the single-energy partial-wave analysis of Jany *et al.* [Jan88] (Jany PWA);
4. a preliminary, Multi-Channel Resonating Group Model (MCRGM) calculation of the ^{4}He continuum [Hof].

The R-matrix analysis is a global parameterization of the $A = 4$ system. That is, the R-matrix parameters are varied to obtain simultaneous best fits to all $A = 4$ scattering and reaction data. In contrast, the two sets of partial-wave analyses are attempts to describe only the n-^{3}He two-body channel. The MCRGM matrix elements result from a microscopic, variational calculation that utilizes a Gaussian-parameterized version of the Bonn nucleon-nucleon potential [Kel89].

We include two sets of partial-wave analyses because the Jany PWA is the most recent partial-wave analysis of n-^{3}He scattering in the few MeV energy region, but it does not cover as broad an energy range as that of Lisowski *et al.* Also, the Jany PWA used the R-matrix phase shifts as its starting parameters. One might therefore expect these latter two analyses to give similar results.

In the case of the R-matrix and MCRGM calculations, elements were obtained at laboratory energies separated by approximately 0.25 MeV below 1 MeV and by

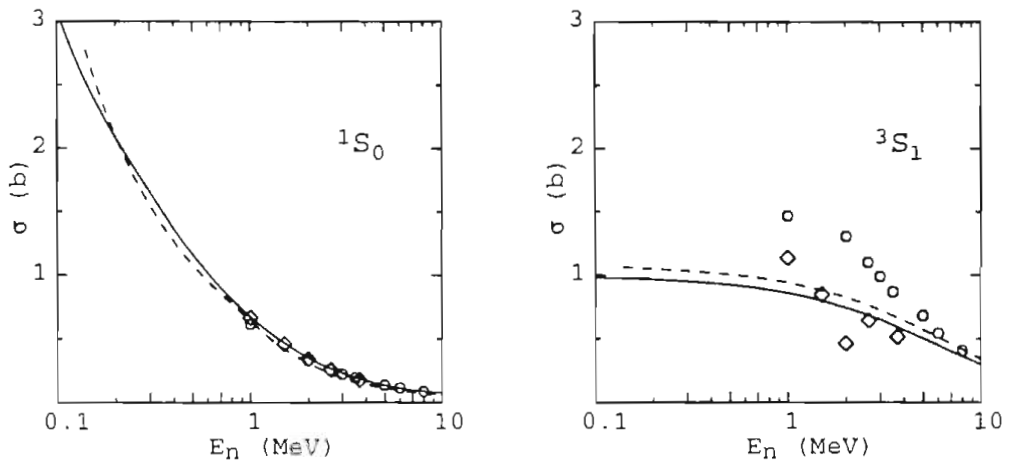

Figure 2.3: The $\ell = 0$ partial-wave cross sections $\sigma(J\ell s\ell s)$ calculated from the four sets of matrix elements, R-matrix (solid line), MCRGM (dashed line), Jany PWA (diamonds) and Lisowski PWA (circles).

approximately 2 MeV above 1 MeV. In these cases the phase shifts (both real and imaginary parts) varied smoothly and slowly, so that a cubic spline interpolation routine could be used to obtain phase shifts at intervals of approximately 0.1 MeV. Table 2.2 compares many of the relevant parameters for the four sets of S-matrix elements.

2.3.1 The Unpolarized and Partial-Wave Cross Sections

Figures 2.3, 2.4, and 2.5 indicate the partial-wave contributions ($\ell \leq 2$) to the total cross section for each of the four sets of matrix elements. For further comparison, we plot the six dominant R-matrix partial-wave cross sections together in Fig. 2.6. According to the R-matrix analysis, partial waves corresponding to $l \geq 2$ contribute less than 4% of the total cross section between 0.1 and 10 MeV and thus are not shown in Fig. 2.6.

We see from the figures that there is considerable discrepancy in many of the partial waves, especially the $\ell \geq 2$ waves. In most cases the R-matrix predicts the largest P-wave cross sections, while the D-waves of Lisowski *et al.* are generally stronger than those of the other three analyses.

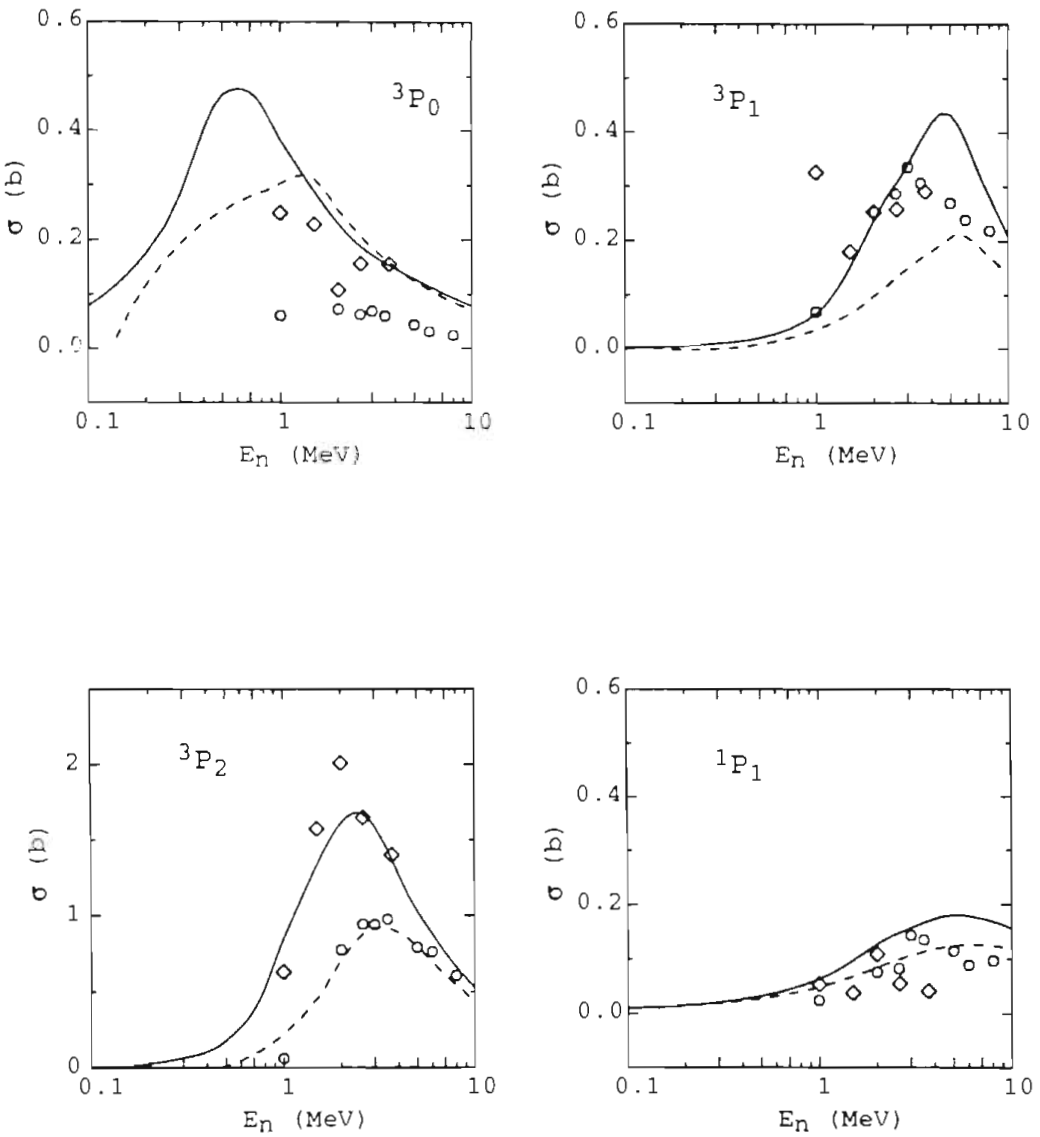

Figure 2.4: The $\ell = 1$ partial-wave cross sections $\sigma(J\ell s\ell s)$ calculated from the four sets of matrix elements. Symbols same as Fig. 2.3. Note scale change for the $^3P_2$ partial wave.

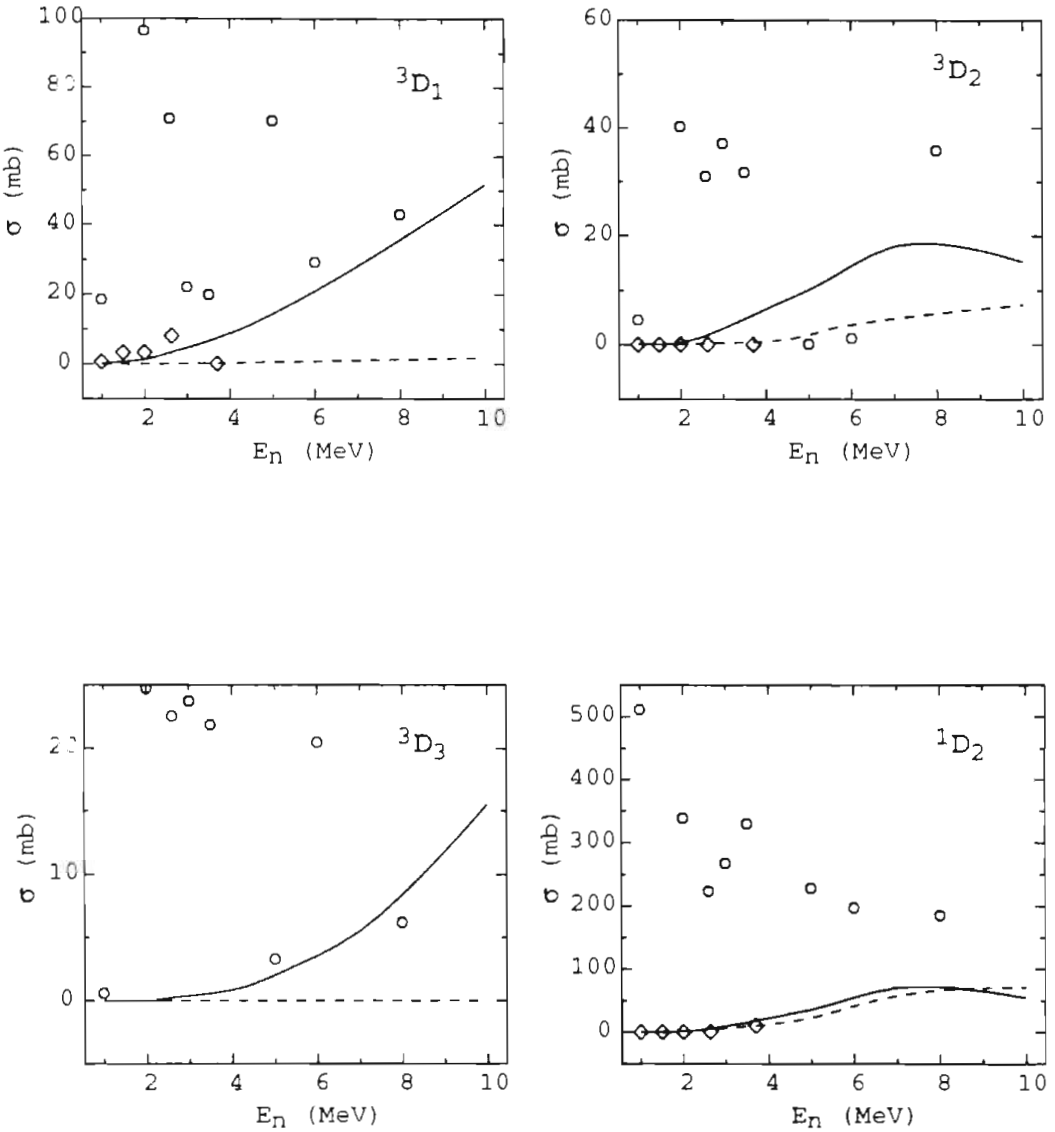

Figure 2.5: The $\ell = 2$ partial-wave cross sections $\sigma(J\ell s\ell s)$ calculated from the four sets of matrix elements. Symbols same as Fig. 2.3. The Jany PWA does not include a $^3D_3$ partial wave. Note scale changes.

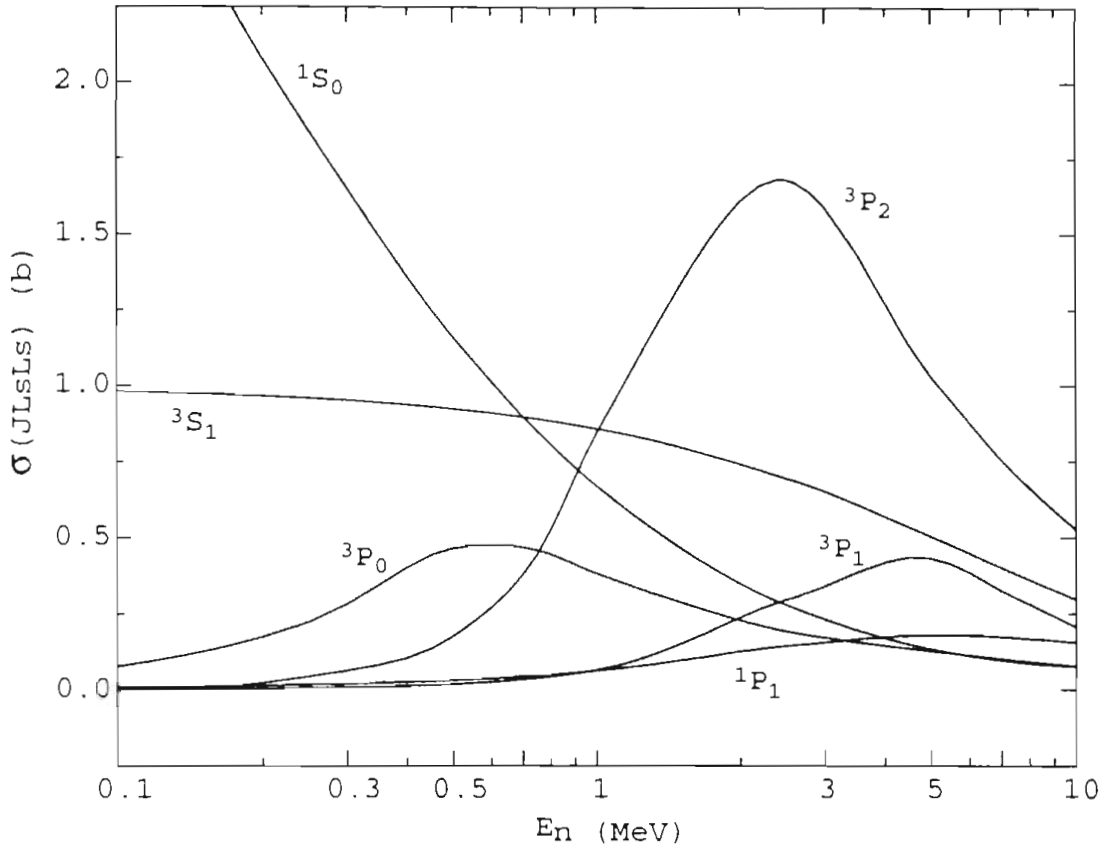

Figure 2.6: The dominant R-matrix partial-wave contributions to the n-^{3}He total cross section.

The dominant partial waves below 100 keV are the two S-waves, $^1S_0$ and $^3S_1$. Scattering through the $^3S_1$ partial wave is mostly elastic, whereas the large $^1S_0$ partial wave indicates the presence of the 0^+ resonance located 20.2 MeV above the ^{4}He ground state. This resonance is unstable against break-up into the p-^{3}H channel and is responsible for the enormous thermal neutron cross section of ^{3}He. The 0^+ resonance is customarily described as a breathing-mode oscillation.

The ^3P_J partial-wave cross sections are obviously related to the series of negative parity states in Fig. 2.2 between 21 and 25 MeV, beginning with a 0^- level at 21.0 MeV. De-Shalit and Walecka have observed that these low energy states may be viewed as $(1s)^3(1p)$ excitations in a simple shell model of ^{4}He [DS66]. The spin of one of the nucleons is flipped, and it is elevated to the (1p) orbital. The resulting nucleon-tri-nucleon cluster then has quantum numbers $\ell = 1$, $s = 1$, $J = 0$, 1 or 2, and isospin $T = 0$ or $T = 1$. These negative parity levels belong to the $\{15\}$ dimensional representation of SU(4) [Fol64]. Another negative parity state with quantum numbers $s = 0$, $\ell = 1$, $J = 1$ and $T = 0$ belongs to the $\{15\}$ representation as well. Spin-dependent forces and charge-symmetry breaking are responsible for breaking the degeneracy of the $\{15\}$ supermultiplet.

The total (unpolarized) cross section is shown in Fig. 2.7. The R-matrix and the two phase-shift analyses describe the total cross section about equally well, with the Lisowski PWA perhaps doing the best between 1 and 10 MeV. On the other hand, the MCRGM calculation does not quantitatively reproduce the experimental values above 1 MeV. As this is the region where $\ell = 1$ scattering begins to dominate, the inadequacy of the MCRGM calculations can probably be attributed to insufficient P-wave amplitudes. Comparing the individual partial-wave cross sections, we find the greatest discrepancy between the R-matrix and MCRGM results in the $^3P_2$ partial wave. The $^3P_2$ wave of the MCRGM calculation is nearly identical with that of the Lisowski PWA. The latter uses unusually large D waves to account for the "missing" cross section (see Fig. 2.5).

2.3.2 The Spin-Spin Cross Sections

We now describe how the spin-dependent total cross-section differences $\Delta\sigma_L$ and $\Delta\sigma_T$ reflect the excited structure of ^{4}He and how these observables may be used to delineate

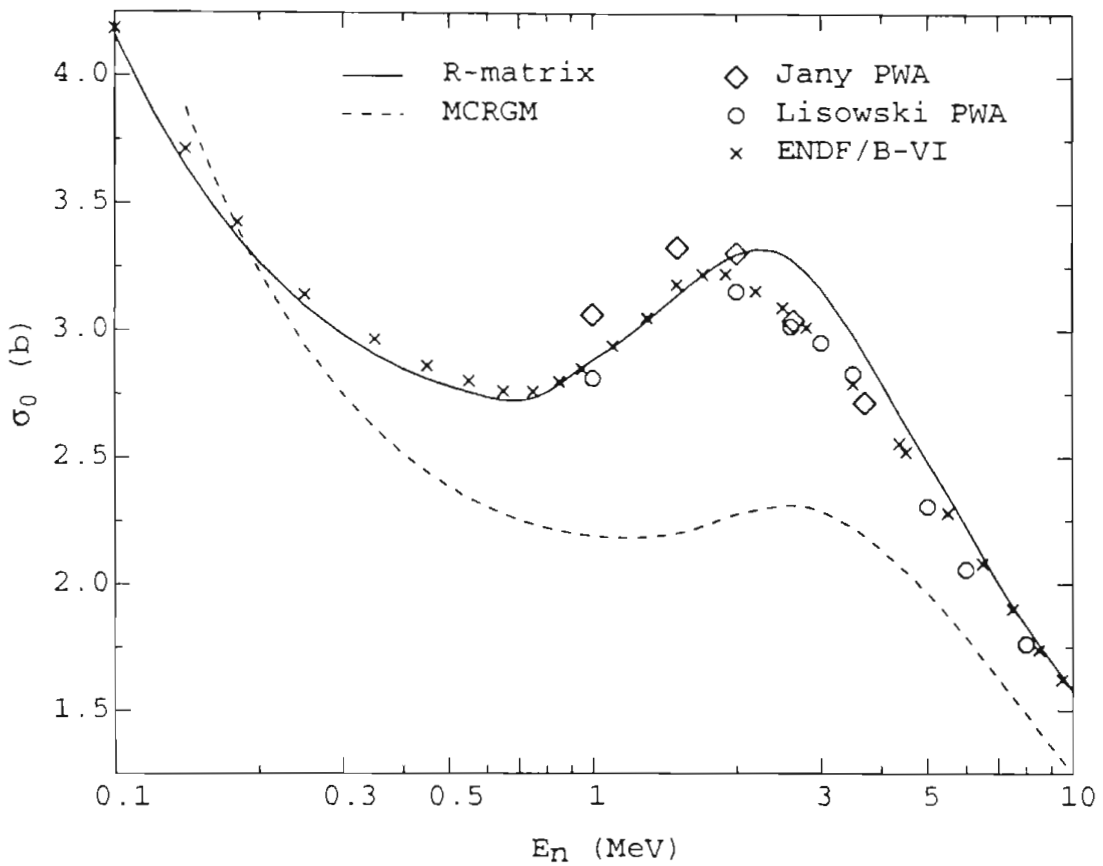

Figure 2.7: The (unpolarized) n-^{3}He total cross section calculated using the four sets of phase shifts detailed in the text. The ENDF/B-VI [Hal91a] fit to the experimental values is also shown (crosses).

specific partial-wave information.

Calculated values of $\Delta\sigma_L$ and $\Delta\sigma_T$ using the four groups of matrix elements are shown in Figs. 2.8 and 2.9. At low energies (<500 keV) both $\Delta\sigma_L$ and $\Delta\sigma_T$ are large and negative, indicating that scattering primarily occurs between antiparallel spins. At these low energies the total cross section is dominated by the 0^+ resonance at 20.2 MeV in the ^{4}He system. A 0^+ resonance must have $F(Jlsl's) = -1$ for either the longitudinal or transverse geometry. Therefore the contribution of this state to the unpolarized cross section is doubled when the cross-section differences $\Delta\sigma_L$ and $\Delta\sigma_T$ are calculated (see Eqs. (2.55) and (2.56)). As E_n increases, the ratio of triplet-to-singlet S-wave scattering increases, which along with the emergence of P waves causes both $\Delta\sigma_L$ and $\Delta\sigma_T$ to cross through zero near 1 MeV.

Above 1 MeV, we see considerable disagreement in the predictions of both $\Delta\sigma_L$ and $\Delta\sigma_T$. The main contributors in this energy region (according to the R-matrix analysis) are the $^3S_1$, $^3P_1$ and $^3P_2$ partial waves. However, the $^3P_1$ partial wave cannot contribute to $\Delta\sigma_T$ because $F_1(^3P_1) = 0$. Therefore $\Delta\sigma_T$ is mainly a measure of the $^3P_2$ strength in this energy region, with some contribution from the $^3S_0$ and $^1P_1$ partial waves. Correspondingly, between 1 and 5 MeV (where the $^3P_2$ wave is at a maximum) the calculated values of $\Delta\sigma_T$ disagree by as much as 1.5 barn. This would indicate that there is no consensus as to the strength of the $^3P_2$ partial wave—a conclusion that is supported by Fig. 2.4. Comparing the four sets of analyses, we find similarity between the $^3P_2$ waves of the Lisowski PWA and the MCRGM calculation, but the R-matrix and Jany $^3P_2$ waves are considerably stronger. This explains why the latter two analyses predict higher values of $\Delta\sigma_T$: the $^3P_2$ wave makes a positive contribution to $\Delta\sigma_T$ (see Table 2.1). The Lisowski PWA prediction of $\Delta\sigma_T$ is noticeably lower than the other three predictions. The difference is the unusually strong $^1D_2$ partial wave of Lisowski *et al.* (see Fig. 2.5) which lowers $\Delta\sigma_T$ by as much as one barn.

The sensitivity to the $^3P_2$ wave is reduced by half in the longitudinal geometry (see Table 2.1), and so slightly better agreement is observed in the values of $\Delta\sigma_L$, particularly above 2 MeV. The effect of the $^3P_2$ partial wave may be removed entirely using the linear combination $(3\Delta\sigma_L - \Delta\sigma_T)$. At the same time, this linear combination magnifies the $^3P_1$ contribution by a factor of six.

The difference $(\Delta\sigma_T - \Delta\sigma_L)$ for the four sets of calculations is shown in Fig. 2.10. All S-wave and spin-singlet contributions to the total cross section are removed by

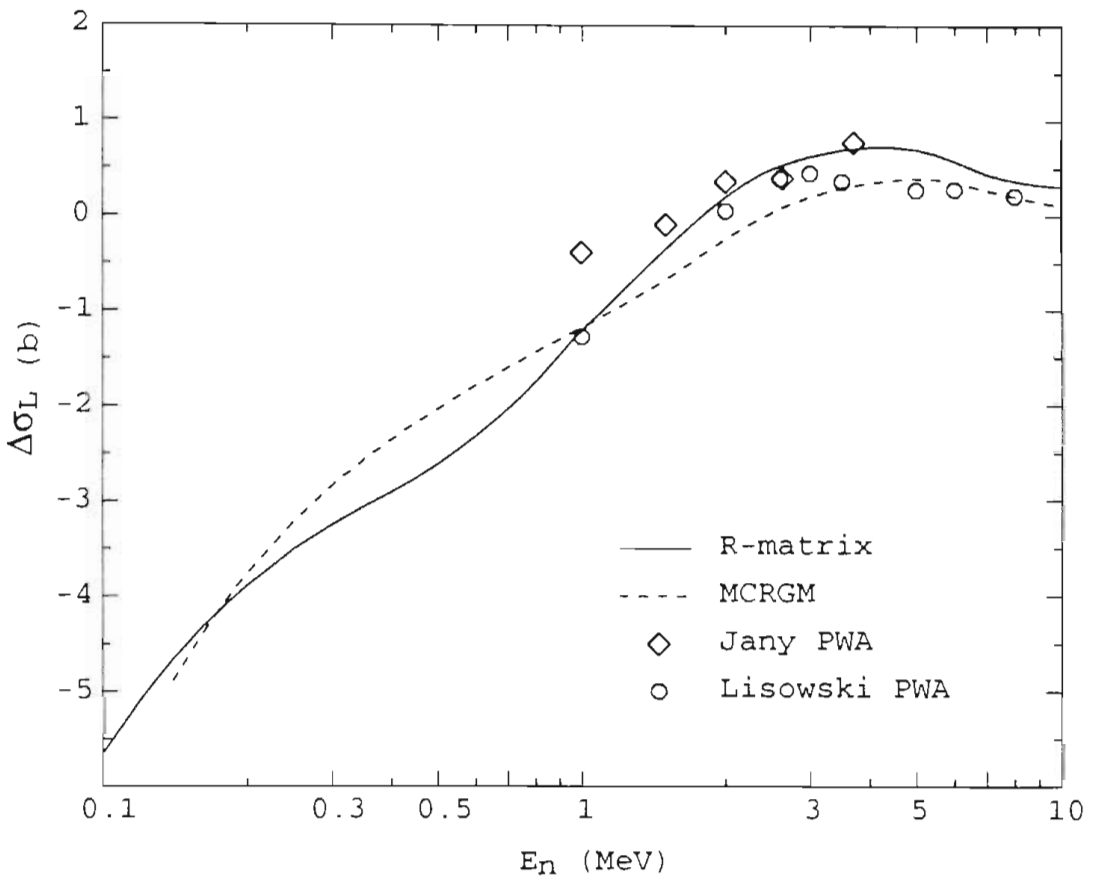

Figure 2.8: Calculated values of $\Delta\sigma_L$ using the four set of S-matrix elements detailed in the text.

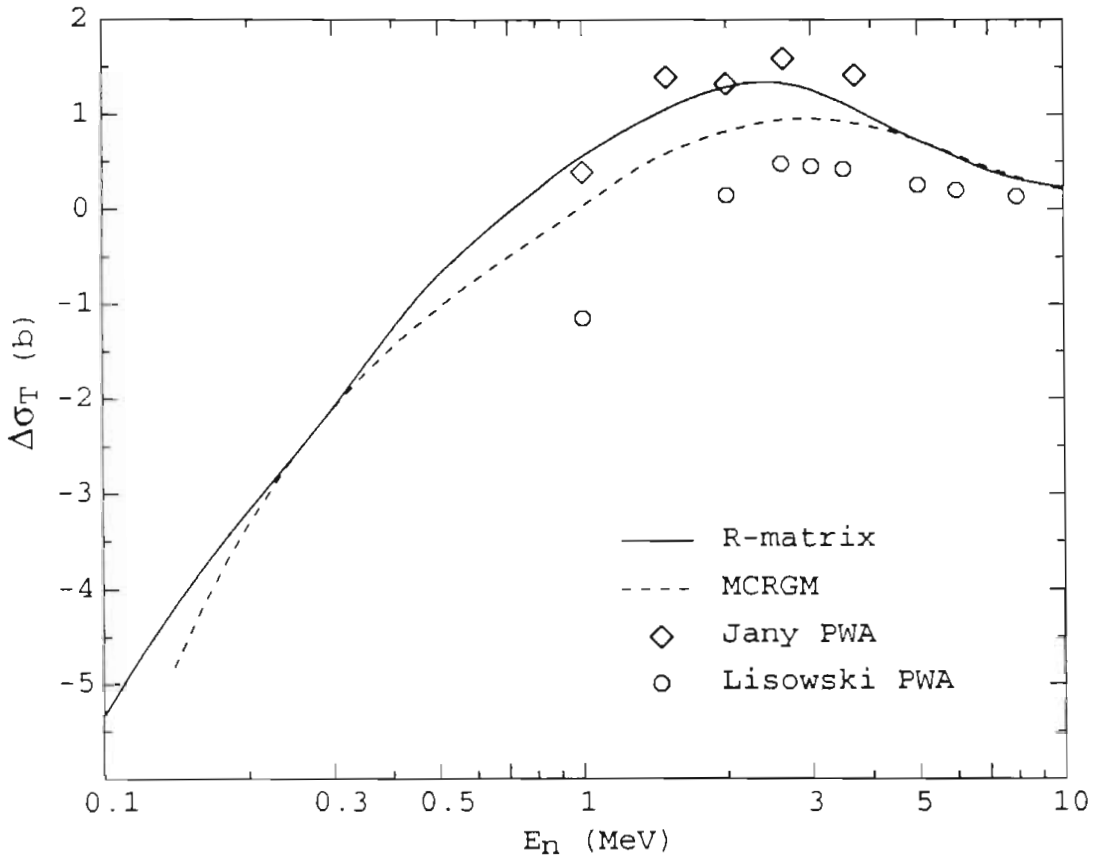

Figure 2.9: Calculated values of $\Delta\sigma_T$ using the four set of S-matrix elements detailed in the text.

this linear combination of $\Delta\sigma_L$ and $\Delta\sigma_T$.[7] Therefore, this combination is extremely sensitive to the low-lying negative-parity states shown in Fig. 2.2. The large difference around 700 keV is a result of $^3P_0$ scattering (a 0^- resonance at 21.0 MeV). For the $^3P_0$ partial wave, scattering only occurs between *anti*-parallel spins in the longitudinal spin geometry ($F_0 = -1$), whereas the opposite is true for the transverse geometry ($F_1 = +1$). Therefore, the contribution of the $^3P_0$ partial wave is magnified by a factor of four when the difference $(\Delta\sigma_T - \Delta\sigma_L)$ is taken. Combinations utilizing the unpolarized cross section σ_0 can be made to exploit other partial waves as well. In particular, we find that below about 1 MeV,

$$\Delta\sigma_T - \Delta\sigma_L \simeq 4\,\sigma(^3P_0), \tag{2.58}$$

$$2\,\sigma_0 + \Delta\sigma_L \simeq \frac{10}{3}\,\sigma(^3S_1), \tag{2.59}$$

$$\Delta\sigma_L + \Delta\sigma_T \simeq 4\,\sigma(^1S_0) + \frac{4}{3}\,\sigma(^3S_1). \tag{2.60}$$

To illustrate this point, we have included the R-matrix $^3P_0$ partial wave in Fig. 2.10 (dash-dotted line). It is evident that the scattering amplitudes for these lowest partial waves can be completely and uniquely extracted from a complete measurement of $\Delta\sigma_L$ and $\Delta\sigma_T$ below 1 MeV. Such measurements are seriously hampered by the difficulty in producing polarized neutrons in the 0.1–1 MeV energy region, however.

Finally, we see in Fig. 2.10 that there is essentially no difference between the calculated values of $\Delta\sigma_L$ and $\Delta\sigma_T$ when the phase shifts of Lisowski *et al.* are used. Referring again to Table 2.1, we find this indicative of strong S-wave and spin-singlet scattering amplitudes. Examination of the individual partial waves agrees with this conclusion. The $^3S_1$ and $^1D_2$ partial waves are considerably stronger in the Lisowski PWA than in any of the other three analyses.

The sensitivity of $\Delta\sigma_L$ and $\Delta\sigma_T$ to the $l \geq 2$ scattering as well as the amplitudes corresponding to mixed orbital angular momentum can be determined from Table 2.1. In the energy range under consideration, such contributions to the total cross section are relatively unimportant in comparison to the S and P-wave amplitudes (an ex-

[7] The $\Delta\sigma_T$-$\Delta\sigma_L$ combination is sensitive to $\ell = 0$ scattering in that the off-diagonal elements of the S-matrix corresponding to $^3S_1$-$^3D_1$ transitions do not disappear in this particular combination of $\Delta\sigma_L$ and $\Delta\sigma_T$ (see Table 2.1). Below 1 MeV their contribution to the spin-spin cross section is negligible (see Fig. 2.11).

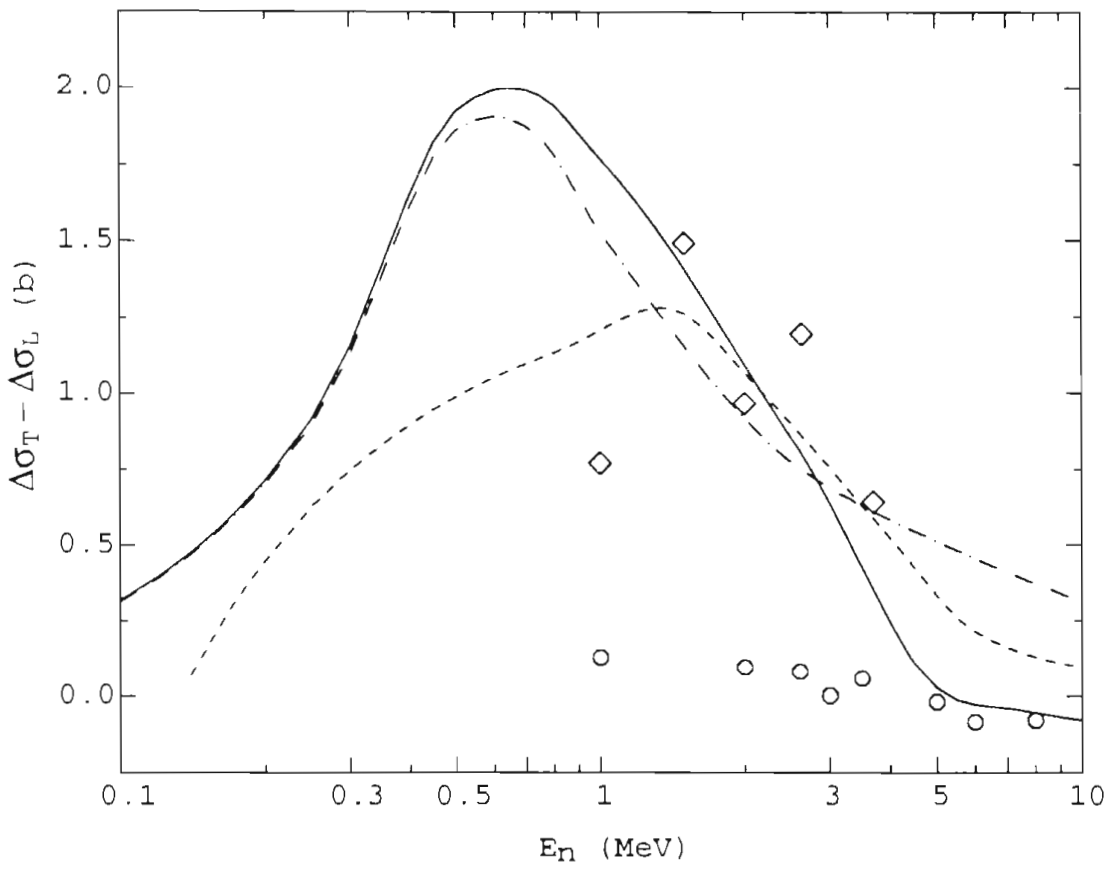

Figure 2.10: Calculated values of the quantity $(\Delta\sigma_T - \Delta\sigma_L)$ using the four sets of S-matrix elements detailed in the text. Symbols same as Fig. 2.8. Also shown (dash-dotted line) is four times the $^3P_0$ cross section from Fig. 2.6, $4\sigma(^3P_0)$.

ception is the Lisowski PWA $^1D_2$). Linear combinations of σ_0, $\Delta\sigma_L$ and $\Delta\sigma_T$ can be made to emphasize these partial waves at higher energies once the effects of $l = 0$ and $l = 1$ scattering have been well determined.

However, it is worth noting that the spin-spin cross section is one of the few observables that displays considerable sensitivity to the mixed-orbital angular momentum amplitudes. We end this chapter with a brief discussion of these off-diagonal contributions.

Due to non-central forces in the nuclear hamiltonian, the orbital angular momentum is not a conserved quantity of motion. These forces are responsible for the off-diagonal elements of the S matrix. However, it is still convenient to speak of eigen-phase shifts $\delta^J_{\ell s}$ which result from the partial-wave expansion in Eq. (2.16). There are two common parameterization schemes in which the S matrix is expressed in terms of eigen-phase shifts. Blatt and Biedenharn write [Bla52a]

$$S = \begin{pmatrix} \cos^2\epsilon_J e^{2i\delta^J_{\ell s}} + \sin^2\epsilon_J e^{2i\delta^J_{\ell' s}} & \frac{1}{2}\sin(2\epsilon_J)\left[e^{2i\delta^J_{\ell s}} - e^{2i\delta^J_{\ell' s}}\right] \\ \frac{1}{2}\sin(2\epsilon_J)\left[e^{2i\delta^J_{\ell s}} - e^{2i\delta^J_{\ell' s}}\right] & \sin^2\epsilon_J e^{2i\delta^J_{\ell s}} + \cos^2\epsilon_J e^{2i\delta^J_{\ell' s}} \end{pmatrix} \tag{2.61}$$

whereas in the Stapp parameterization

$$S = \begin{pmatrix} \cos(2\bar{\epsilon}_J)e^{2i\bar{\delta}^J_{\ell s}} & i\sin(2\bar{\epsilon}_J)e^{i(\bar{\delta}^J_{\ell s}+\bar{\delta}^J_{\ell' s})} \\ i\sin(2\bar{\epsilon}_J)e^{i(\bar{\delta}^J_{\ell s}+\bar{\delta}^J_{\ell' s})} & \cos(2\bar{\epsilon}_J)e^{2i\bar{\delta}^J_{\ell' s}} \end{pmatrix}. \tag{2.62}$$

The latter is the common choice for analysis of nucleon-nucleon data. The quantities ϵ_J and $\bar{\epsilon}_J$ are called *mixing parameters*. In general there can be mixing between states of different channel spin as well (e.g. $^1P_1$ and $^3P_1$).[8] However, the spin-spin cross sections are not sensitive to these mixed-angular momentum states.

Note that in either parameterization, it is the corresponding S-matrix elements that are equivalent. Only in the limit that the mixing parameters are zero do the $\delta^J_{\ell s}$ and $\bar{\delta}^J_{\ell s}$ become equal.

The contributions to $\Delta\sigma_T$ due to the off-diagonal elements of the even-parity $J = 1$ S matrix are shown in Fig. 2.11. Note that $\Delta\sigma_T$ is sensitive to both the magnitude and *sign* of the mixing parameter $\bar{\epsilon}_J$. The MCRGM calculation predicts a negative

[8] In spin-1/2 – spin-1/2 scattering it is not possible to simultaneously mix both channel spin and orbital angular momentum without violating parity. For example, there are no $^3S_1$ to $^1P_1$ matrix elements.

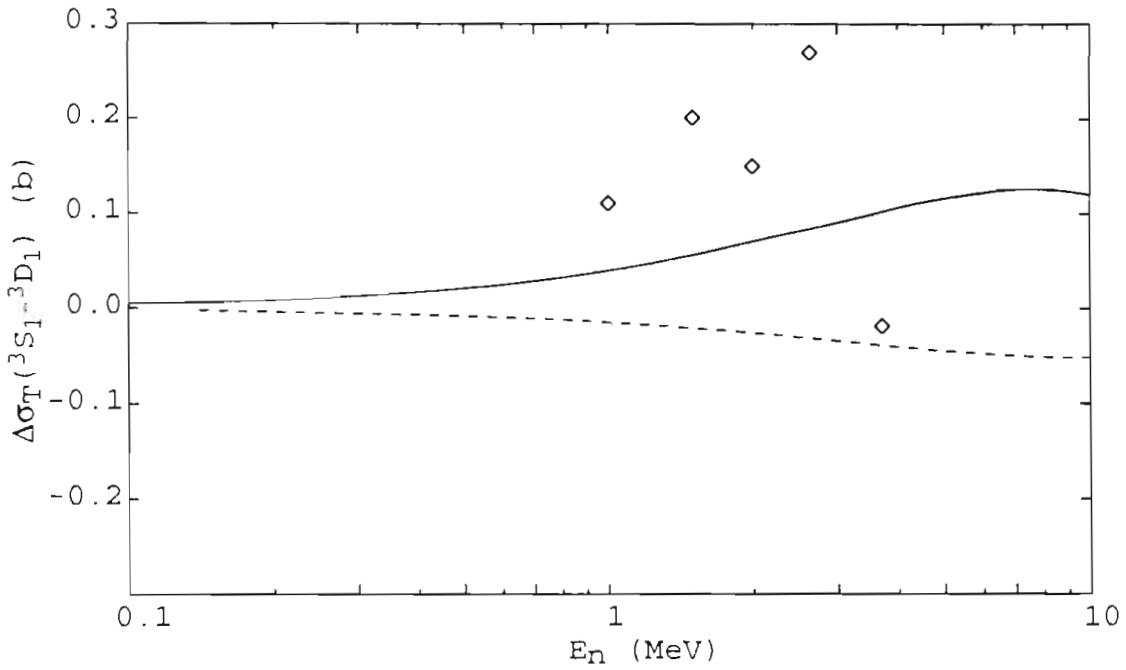

Figure 2.11: Contributions to $\Delta\sigma_T$ due to the mixed orbital angular momentum states $^3S_1$-$^3D_1$. Symbols same as Fig. 2.7.

contribution to $\Delta\sigma_T$, the R-matrix analysis predicts a positive contribution, and the Jany PWA contribution actually *changes* sign near 3 MeV. The phase-shift analysis of Lisowski *et al.* does not include mixing between different orbital angular momenta.

Chapter 3

The Polarized Solid ^{3}He Target

3.1 Low-Temperature Properties of ^{3}He

The design and operation of a scattering target that consists of nearly one-half mole of solid ^{3}He requires some understanding of the low-temperature properties of ^{3}He. Because this information is typically not included in a nuclear physicist's training, and because such a large portion of this project concerned the development of the polarized target, some basic properties of ^{3}He at low temperatures will be discussed in detail. Conversely, the target was designed with a neutron scattering experiment in mind, and those aspects of the target will be discussed in this chapter as well. This chapter begins with a review of some low-temperature physics. A more thorough discussion of this subject can be found in Lounasmaa [Lou74], White [Whi79], Wilks [Wil67] and Richardson and Smith [RS88].

Helium is an inert gas with a very low mass. Additionally, the ^{3}He isotope has a nuclear spin of $\frac{1}{2}\hbar$, making it subject to Fermi-Dirac statistics. These three properties combine to generate unusual characteristics in the condensed phases of ^{3}He. In the scientific vernacular, ^{3}He is a *quantum solid* (or *liquid*), and has been investigated by the low-temperature community for several decades. The results of this investigation allow us to make precise statements concerning the polarization and density of the TUNL target.

3.1.1 The Melting Curve of ^{3}He

^{3}He has the lowest boiling point of any known substance, 3.2 K. Because of its low mass and because the atoms are bound to one another only by the relatively weak Van der Waals force, ^{3}He does not solidify under its own vapor pressure, even if cooled to absolute zero. Solidification can occur only if the liquid is pressurized above 29.3 bar.

The low-temperature phase diagram of ^{3}He is shown in Fig. 3.1. At sample pressures shown the figure, the crystalline structure of solid ^{3}He is body-centered cubic (bcc). If the sample is grown under a pressure exceeding about 100 bars, a hexagonal close-packed (hcp) crystal results. There are four well-determined temperature fixed-points that occur along the melting curve (in zero applied magnetic field):

1. the melting curve minimum (29.3118 bar, 318 mK) [Fog92];
2. the superfluid-A transition (34.34 bar, 2.49 mK) [Gre86];
3. the superfluid-B transition (34.39 bar, 1.93 mK) [Gre86];
4. the nuclear-spin ordering transition (34.39 bar, 0.914 mK) [Fuk87].

Since the nuclear-spin ordering transition in ^{3}He has important implications concerning the polarizability of solid ^{3}He, we will delay discussion of this transition until Section 3.1.2, and turn our attention to fixed points 1–3.

In a manner analogous to electron superconductivity, ^{3}He becomes a superfluid via Bose condensation. Pairs of ^{3}He atoms combine to form integer-spin *quasi-particles* which can then occupy the same quantum mechanical ground state. The A transition corresponds to quasi-particle pairs coupled with net spin angular momentum $s = 1$, orbital angular momentum $\ell = 1$ and total angular momentum $J = 1$. On the other hand, the B phase corresponds to coupling with $\ell = 1$, $s = 1$ and $J = 0$. A review of the superfluid properties of ^{3}He can be found in [Dob83].

The pressure minimum that occurs in the melting curve signals an interesting "transition". The difference in entropy between the liquid and solid phases can be expressed in terms of the melting pressure P_m via the Clausius-Clapeyron equation

$$\frac{\partial P_m}{\partial T} = \frac{S_\ell - S_s}{v_\ell - v_s}. \tag{3.1}$$

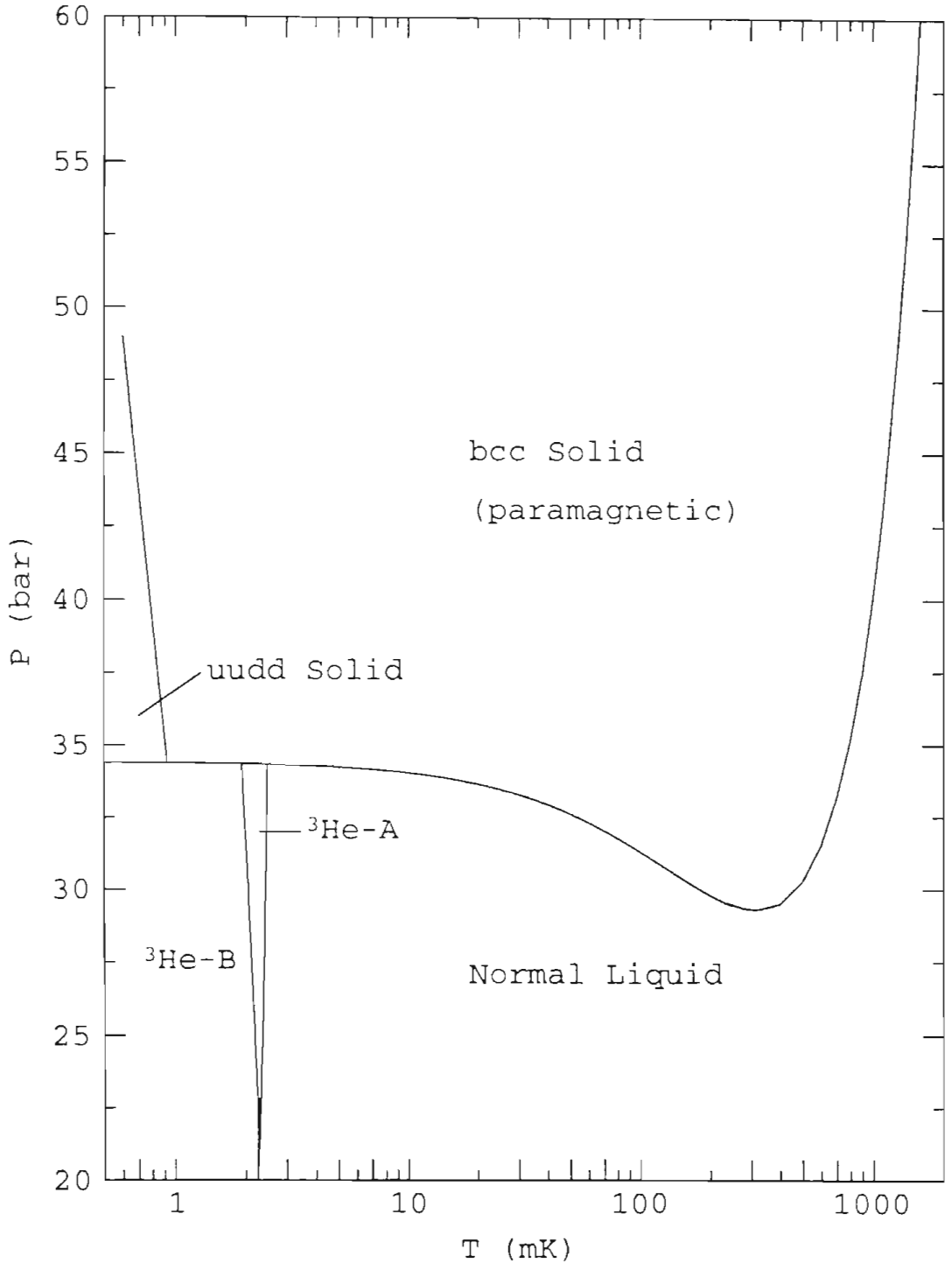

Figure 3.1: The low-temperature phase diagram of ^{3}He for zero applied magnetic field.

Here S_ℓ (S_s) is the entropy of the liquid (solid) and v_ℓ (v_s) is the liquid (solid) molar volume. Below about 1 K, the denominator is essentially constant—approximately 1.2 ± 0.1 cm^3/mole. Since the melting curve has a negative slope below 318 mK, this implies that below this temperature the solid phase has greater entropy than the liquid. This can be understood as follows.

In the solid phase the atoms are rather well localized (except for their zero-point motion) and may be distinguished by their position in the crystal lattice. In such a case Boltzmann statistics are applicable. The entropy of the solid below about 1/2 K is entirely due to the degeneracy of the nuclear spin $I = 1/2$. In the regime where there is no ordering of the nuclear spins, the entropy is temperature-independent:

$$S_s \simeq R \ln 2 \tag{3.2}$$

where R is the universal gas constant, $R = 8.3143$ J mole^{-1} K^{-1}. Atoms in the liquid phase are freer to move about and consequently, cannot be distinguished by their position. This ensemble must be treated with Fermi-Dirac statistics, in which case the entropy is proportional to the temperature,

$$S_\ell = R \ln 2 \frac{T}{T_F}. \tag{3.3}$$

This equation defines the Fermi temperature T_F, which is approximately 0.2 K for pressures near the melting curve. Hence the entropy of the liquid decreases with temperature. At the melting curve minimum, the entropies of the liquid and solid phases are equal, and $S_\ell < S_s$ at lower temperatures. The entropies are shown in Fig. 3.2, which also indicates the presence of the nuclear-spin ordering transition near 1 mK.

The densities of two phases at melting pressure have been measured by Grilly with about 0.5% accuracy [Gri71]. The densities ρ_ℓ and ρ_s are shown as a function of temperature in Fig. 3.3. The relatively wide shaded band in Fig. 3.3 indicates that there is no unique liquid-to-solid ratio at any point along the melting curve. Another way to say this is that for a given pressure and temperature on the melting curve, the ratio of liquid atoms to solid atoms depends upon how the sample of melting ^{3}He was prepared. Suppose, for example, that we prepare a one mole sample of liquid ^{3}He whose density $\rho_\ell = 0.123$ g/cm^3. (Liquid helium is quite compressible so that we can vary its density by adjusting the pressure applied to the sample. Also, the number

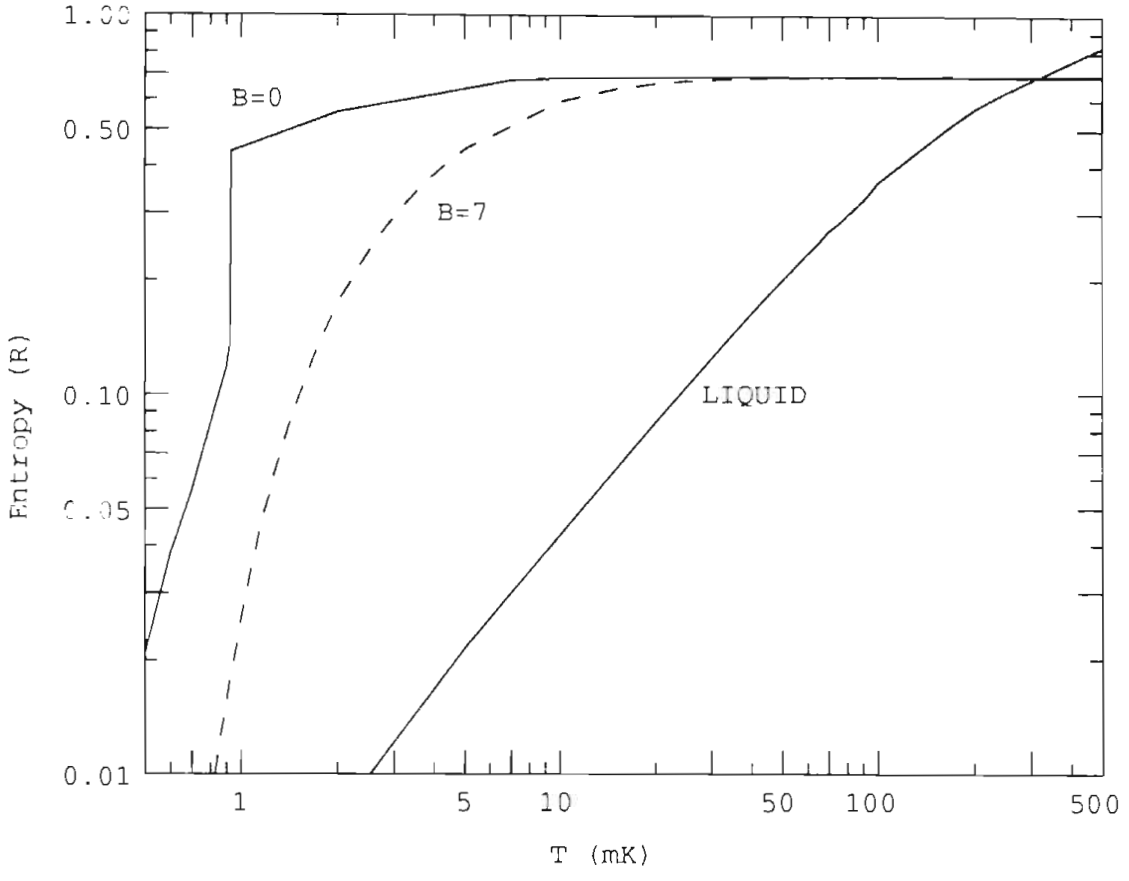

Figure 3.2: The entropy of liquid and solid ^{3}He below 1 K (solid lines). The entropy of solid ^{3}He in a 7 Tesla magnetic field is also indicated (dashed line), where simple paramagnetic behavior is assumed.

of moles in the sample is unimportant so long as it is kept constant.) Figure 3.3 indicates that our sample will begin to solidify if it is cooled to approximately 1 K. The melting pressure P_m (the pressure which the ^{3}He sample exerts on the walls of its container) is then 41.2 bar. As the sample continues to cool, more and more of our liquid sample is converted to solid. Since the solid is less dense than the liquid, the melting pressure decreases with decreasing temperature. Eventually the sample will be completely solid by the time it is cooled to 0.62 K at which point $P_m = 31.7$ bar. If we continue to cool the all-solid sample, Fig. 3.3 reveals that the solid sample again encounters the melting curve at 87 mK. At this point the solid begins to melt. Further cooling continues to reduce the solid-to-liquid ratio although some solid continues to exist even at absolute zero.

This illustrates the care must be given to the preparation of the ^{3}He from which we wish to scatter neutrons. The liquid phase of ^{3}He does not polarize to any great extent. Therefore it is important that the ^{3}He target is completely solid at the lowest temperatures. The polarizations of the solid and liquid phases will be discussed in Sections 3.1.2 and 3.1.3, respectively.

The horizontal lines in Fig. 3.3 correspond to isopycnal[1] lines for melting ^{3}He. The number to the right of each line in Fig. 3.3 indicates the pressure at which the liquid encounters the melting curve. These lines can be used to determine what portion of ^{3}He is liquid at any point along the melting curve. If the starting pressure of the liquid is 33 bar, the liquid begins to solidify at 0.75 K. That portion of sample that remains in the liquid phase at 0.2 K is given by $a/b \approx 0.65$ (see Fig. 3.3). The various starting pressures can be grouped according to the resulting liquid ratio a/b at absolute zero:

1. If $P_{start} < 29.31$ bar, $a/b = 1$ at all temperatures, i.e., no portion of the sample will solidify.

2. If $P_{start} \leq 33.73$ bar, $a/b = 1$ at some $T < 0$. The sample will completely liquify as the temperature approaches zero.

3. If $P_{start} > 44.90$ bar, $a/b = 0$ at $T = 0$. The sample will remain solid at absolute zero.

4. If $33.73 < P_{start} < 44.90$ bar, $0 < a/b < 1$ at $T = 0$.

[1]Isopycnals are lines of constant-density in a P, T diagram.

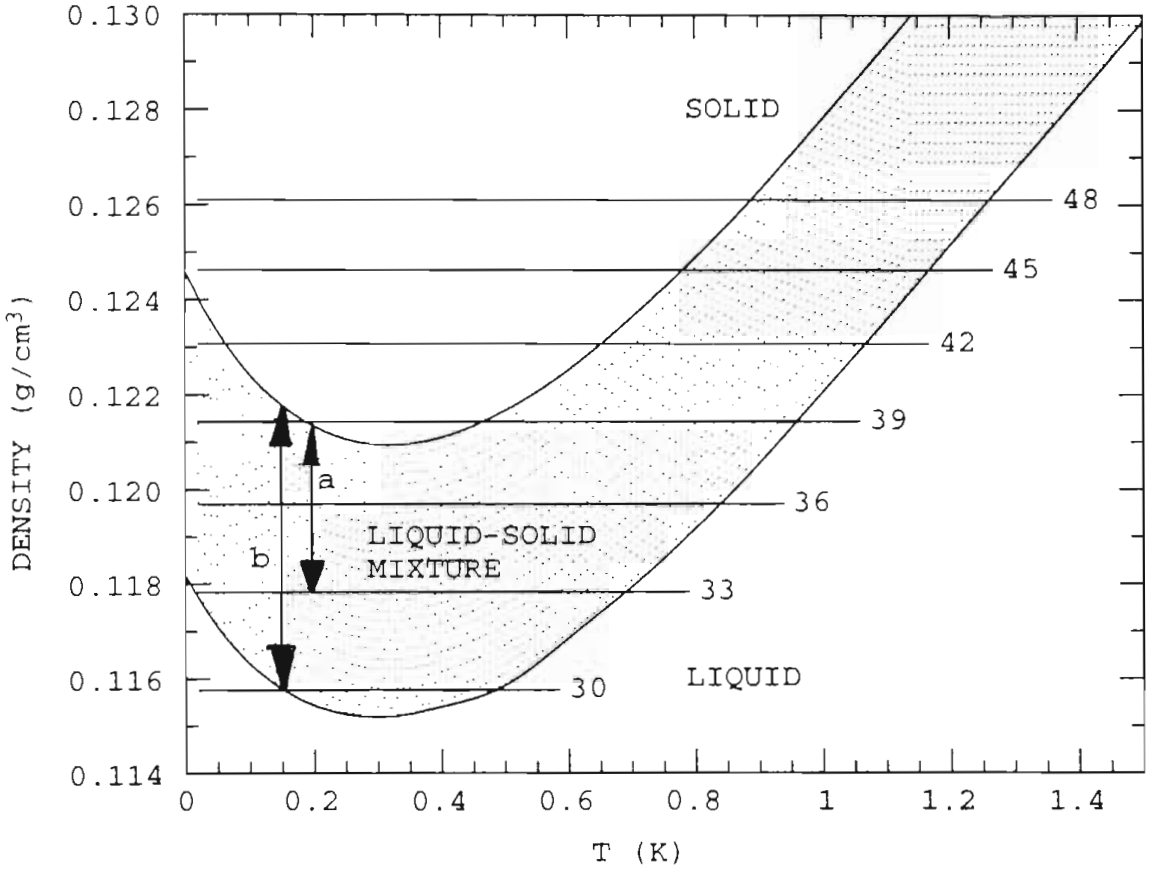

Figure 3.3: The density of liquid and solid ^{3}He along the melting curve. The numbers to the right of the horizontal lines correspond to the initial sample pressure, measured in bar. Additional details in the text.

Item 4 indicates that a sample of ^{3}He can be made to stay on the melting curve all the way to absolute zero. We will re-examine this in Section 3.3.2 when the operation of the ^{3}He melting curve thermometer is discussed.

3.1.2 Polarization of Solid ^{3}He

The magnetic properties of solid ^{3}He have elicited considerable attention since it was discovered that the susceptibility of the solid deviated from simple paramagnetic behavior at temperatures below about 50 mK. It was long believed that the solid would undergo a second-order[2] antiferromagnetic phase transition near 2 mK. The mechanism for this transition was thought to be ordinary Heisenberg spin-exchange (exchange between nearest neighbors only). Even in the solid phase, ^{3}He has a large zero-point motion—about 30% of its interatomic distance (approximately 3.6 Å), and there is significant overlap of the atomic wavefunctions. The Pauli principle induces an interaction between the spin-1/2 nuclei that causes atoms to exchange positions in the bcc lattice. This interaction becomes important when the exchange energy approaches the lattice energy kT.

However, it was soon discovered that the Heisenberg nearest neighbor model was inadequate in its ability to describe the experiments. For example, the observed paramagnetic-to-antiferromagnetic transition is first-order and occurs at 0.91 mK (in zero field) rather than a second-order transition at 2 mK. It is now understood that "ring-type" exchanges between three and four atoms at a time must be considered in addition to the nearest-neighbor exchanges. A schematic drawing of the four most dominant spin-exchange mechanisms is given in Fig. 3.4. A comprehensive review of the magnetic properties of solid ^{3}He is given by Roger, Hetherington and Delrieu [Rog83].

At temperatures above T_N, the Néel temperature, the polarization of solid ^{3}He P_3 can be described by a Brillouin function that includes the effects of the two-, three- and four-atom exchange parameters (cf. Eq. (7.28) in Roger, Hetherington

[2] A second-order phase transition signals the emergence of a new phase that co-exists in equilibrium with the original phase. A first-order transition marks the abrupt change from one equilibrium state to another.

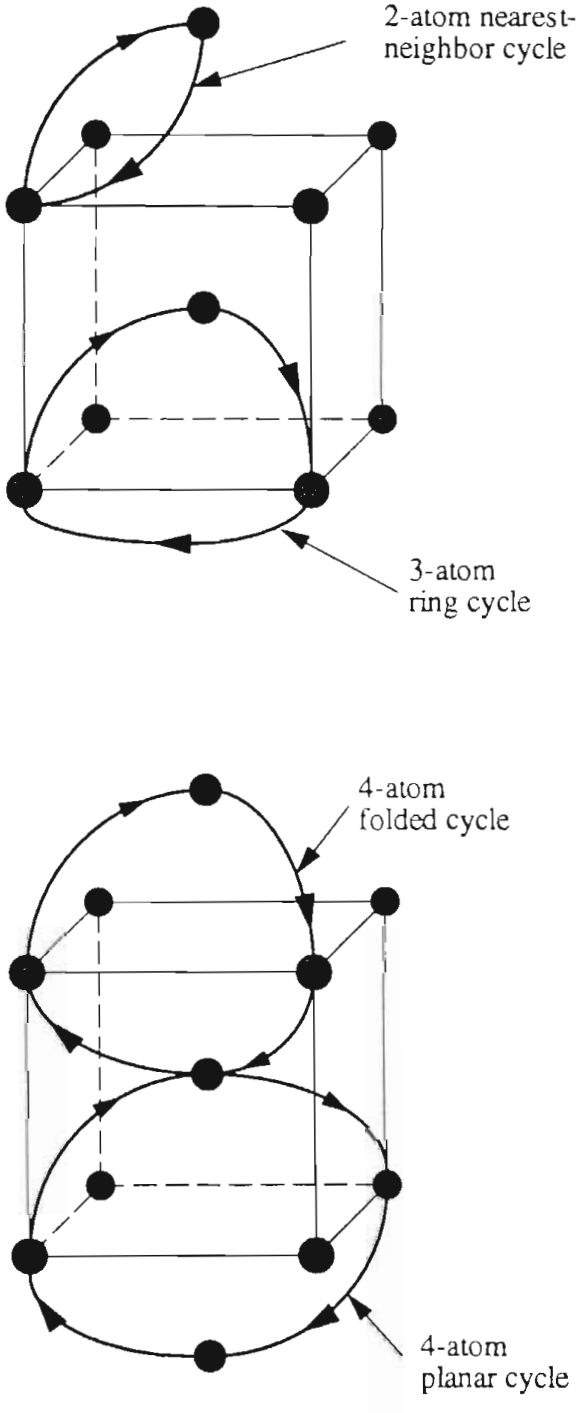

Figure 3.4: Spin-exchange mechanisms in bcc ^{3}He.

Nearest-neighbor J_{nn}	Triple-atom J_t	Planar 4-atom K_p	Folded 4-atom K_f	Weiss Θ
-0.377	-0.155	-0.327	0.0	-1.81

Table 3.1: The exchange parameters used to calculate the polarization of bcc ^{3}He. Values are taken from [Sti85a]. Additional information can be found in [Sti85b] and [Rog83]. All units are mK.

and Delrieu [Rog83]),

$$\begin{aligned} P_3 &= \tanh\left\{\frac{1}{kT}\left[(4J_{nn} - 36J_t + 18K_p + 18K_f)\,P_3 + 6\,(K_p + K_f)\,P_3^3 + \mu_3 H\right]\right\} \\ &= \tanh\left\{\frac{1}{kT}\left[\Theta P_3 + 6\,(K_p + K_f)\,P_3^3 + \mu_3 H\right]\right\}. \end{aligned} \tag{3.4}$$

Here J_{nn} and J_t are the nearest-neighbor and triple-exchange parameters, and K_p and K_f are parameters for two types of four-spin exchanges, the planar- and folded-exchange mechanisms. The interaction between the applied field H and the ^{3}He magnetic moment ($\mu_3 = -2.1276$ nm) is called the Zeeman field. Θ is the Weiss temperature for ^{3}He, and is known from experiment [Dob93];

$$\Theta = -1.8 \pm 0.1\text{mK}. \tag{3.5}$$

Equation (3.4) can be solved by iteration. First, the exchange parameters are ignored and the polarization due to the Zeeman field is calculated. This would be the polarization corresponding to a simple paramagnet. This estimate of the polarization is inserted in Eq. (3.4) and a new value of P_3 is calculated. The new value is then inserted, and so on until P_3 converges. The result for a 7 Tesla field is shown in Fig. 3.5. Below approximately 3 mK, the Brillouin function in Eq. (3.4) is no longer applicable, as this is the temperature at which solid ^{3}He undergoes the antiferromagnetic phase transition in a 7 Tesla field. Table 3.1 lists the values of the exchange parameters used to generate Fig. 3.5.

For this experiment, we are primarily concerned with temperatures in the 10–15 mK range. In anticipation of Chapter 5, we note that in this temperature region a 2% resolution in T results in a 1.5% uncertainty in the polarization. The ± 0.1 mK uncertainty associated with the Weiss temperature contributes a negligible error to the calculation of P_3.

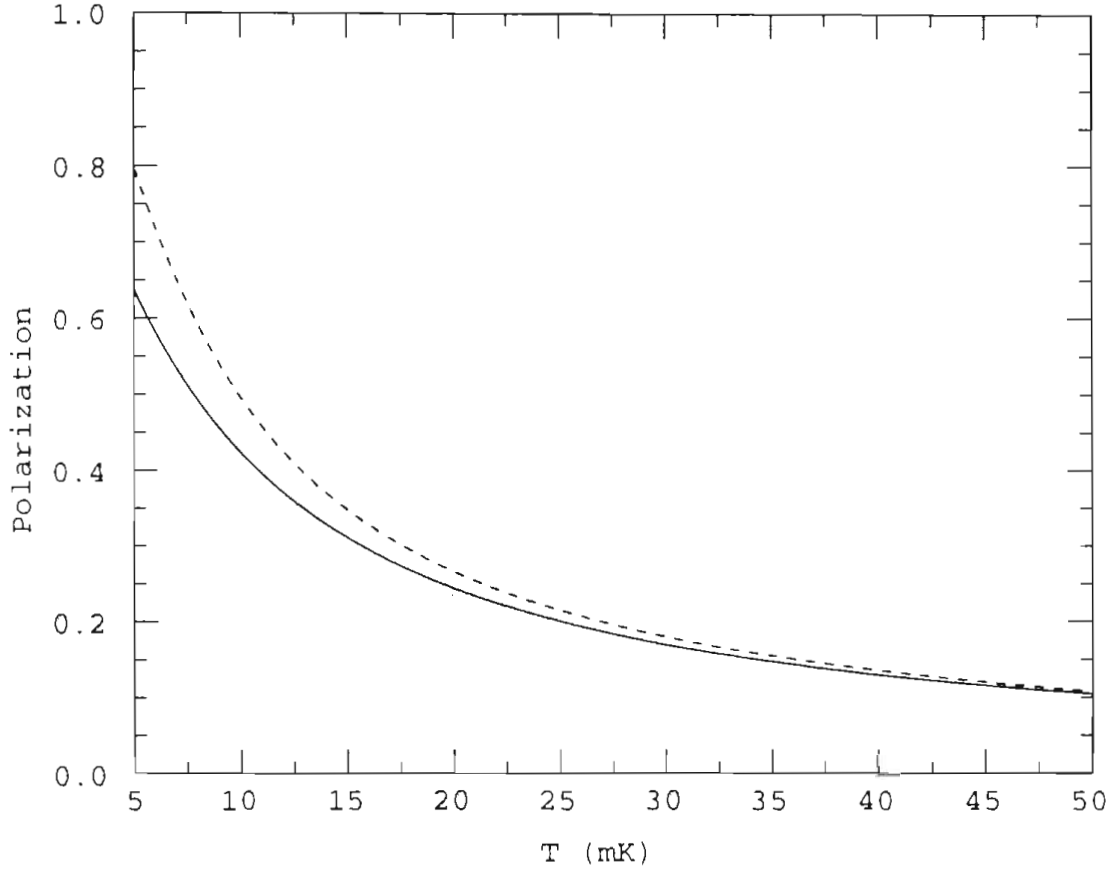

Figure 3.5: The polarization of solid ^{3}He for a 7 Tesla magnetic field. The polarization is calculated assuming the two-, three-, and four-spin exchange parameters listed in Table 3.1 (solid line) and assuming simple paramagnetic behavior (dashed line).

3.1.3 Polarization of Liquid ^{3}He

The properties of liquid ^{3}He are governed by Fermi-Dirac statistics. Below approximately 1 K, the Landau theory of Fermi liquids [Lan57] can be used to account for many of the observed properties. A simplified discussion of the Landau theory can be found in Wilks [Wil67]. We are mainly concerned with the polarizability of the liquid and will only address this issue briefly.

Because the thermal conductivity of liquid ^{3}He increases at low temperatures, a sample of liquid ^{3}He would be much easier to cool than a solid sample. One must wonder why we bother with the solid. The answer is that liquid ^{3}He cannot be polarized to any great extent. Above 1 K, the susceptibility χ_ℓ of the liquid follows Curie's law, and so $\chi_\ell \propto T$. At lower temperatures however, χ_ℓ becomes essentially independent of temperature in a manner similar to a perfect Fermi gas. Ramm *et al.* have measured the susceptibility of liquid ^{3}He as a function of temperature for a variety of molar volumes [Ram70]. Extrapolating their results to the value of V_ℓ at the melting curve minimum (26.18 cm^3/mole), we find $\chi_\ell/C \rightarrow 5.4$ as T approaches zero. The reduced units are in terms of the Curie constant, $C = \mu_3^2 N/k$.

The polarization of the liquid in the presence of an applied field H is then

$$\begin{aligned} P_\ell &= \frac{\chi_\ell H}{\mu_3 N} = 5.4\,\frac{\mu_3 H}{k} \\ &= \frac{\mu_3 H}{k T_F^*}. \end{aligned} \tag{3.6}$$

Here T_F^* is the magnetic Fermi temperature, $T_F^* = 1/5.4 = 0.185$ K. The polarization of the liquid is essentially independent of temperature below T_F^*. For a 7 Tesla field, P_ℓ has a maximum value of 2.95%.

3.2 The TUNL Polarized ^{3}He Target

The polarization of solid ^{3}He was discussed in Section 3.1.2. We have seen that appreciable nuclear polarization only occurs when the Zeeman splitting $\mu_3 H/kT$ is of order one. Since $\mu_3/k = 0.778$ mK Tesla^{-1} this requires $H/T \approx 1$. Continuous magnetic fields much greater than approximately 10–20 Tesla are not currently available, and so it is necessary to cool the target to a few milliKelvin in order to produce significant

values of P_3. The apparatus used to achieve these extreme conditions is discussed in the following sections.

3.2.1 The TUNL Spin-Spin Cryostat

A schematic diagram of the TUNL polarized target cryostat (the "Spin-Spin cryostat") is shown in Fig. 3.6. The cryostat has been used previously to polarize targets of ^{27}Al, ^{93}Nb and TiH_2. A more thorough description of the facility is offered in Haase, Gould and Seagondollar [Haa86].

A 7 Tesla superconducting magnet[3] is mounted in the liquid Helium dewar of the cryostat. The magnet is a split-coil solenoid with NbTi windings. The design of the magnet allows beam access for magnetic fields that are either parallel or perpendicular to the beam direction. The magnet is first charged to 86.2 A which produces a field of 7 Tesla, and is then switched to persistent-current mode so that the field is constant throughout the course of the experiment. Over the volume occupied by the polarized target, the magnetic field is uniform to 0.1%. Hollow brass spacers are inserted in the magnet bore (see Fig. 3.6) to minimize the attenuation of the neutron beam due to LHe. The cryostat requires approximately 100 liters of LHe for the initial cooling and 30 liters per day thereafter. The maximum time between transfer is 25–30 hours.[4]

At the heart of the cryostat is the commercially-manufactured ^{3}He-^{4}He dilution refrigerator[5] that is used to cool the target below 1 K. Originally proposed by H. London in 1951 [Lon51], dilution refrigerators have been used extensively for low-temperature research since the first successful model was constructed by Das *et al.* in 1965 [Das65]. Comprehensive treatments of the principles and methods of dilution refrigeration can be found in Lounasmaa [Lou74] and Anderson [And70].

The key to the dilutive cooling of ^{3}He-^{4}He mixtures is the phase separation of the two liquids which occurs at 0.84 K. Above this temperature, liquid mixtures of ^{3}He and ^{4}He coexist in a single phase, regardless of the relative concentrations. As the mixture is cooled, however, a concentrated (^{3}He-rich) phase begins to float atop a diluted (^{4}He-rich) phase. The ^{3}He-^{4}He phase diagram (cf. page 18 [Lou74]) indicates

[3] American Magnetics Incorporated, Oak Ridge, Tennessee.

[4] A new dewar for the Spin-Spin cryostat has been recently purchased. It hoped that the new dewar will operate with approximately 48 hours between LHe transfers.

[5] S. H. E. Model 430.

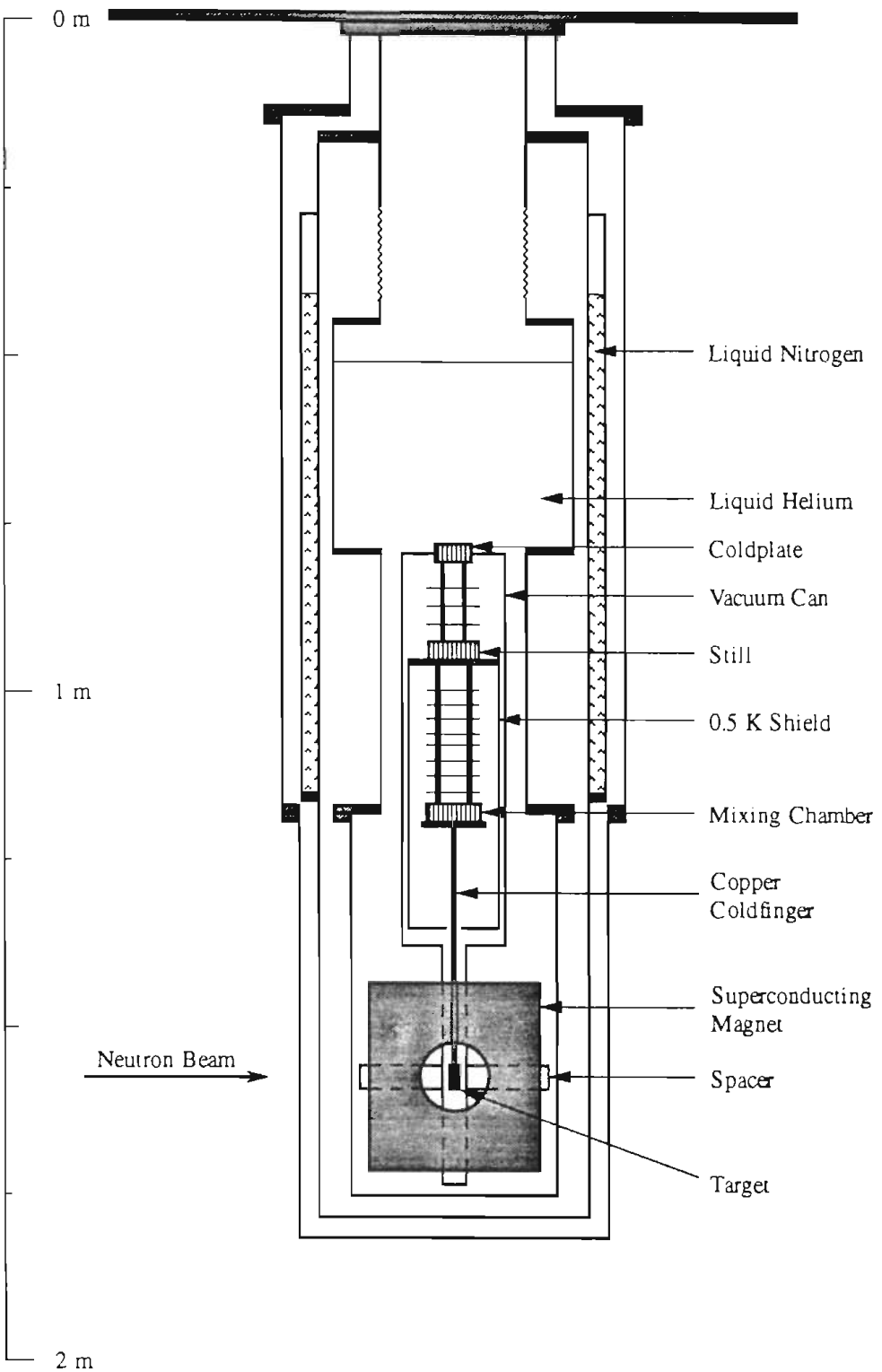

Figure 3.6: The Spin-Spin Cryostat

that the concentration of ^{3}He in the dilute phase remains non-zero even as absolute zero is approached. In fact, the limiting solubility is rather high, 6.4%.

Figure 3.7 shows a simplified model of a standard-design dilution refrigerator. The phase separation occurs in a region known as the *mixing chamber*. A distillation container (the *still*) is connected to the mixing chamber by a length of tubing that extends into the dilute portion of the ^{3}He-^{4}He mixture. Heat is applied to the still in order to maintain a temperature near 0.6 K. At this temperature the vapor pressure of ^{3}He is approximately 1000 times that of ^{4}He, so that by pumping on the still, ^{3}He atoms are preferentially removed from the dilute phase. As the ^{3}He atoms are removed by this distillation process, ^{3}He atoms from the upper, concentrated phase must cross the boundary to the lower, dilute side of the mixing chamber in order to maintain chemical equilibrium. The cooling that occurs during this process is similar to the adiabatic cooling of an expanding gas. The liquid ^{4}He is a superfluid by this point, and so exists in its quantum-mechanical ground state. When crossing the phase-separation boundary, the ^{3}He atoms are "expanding" into a mechanical vacuum of sorts. Since the entropy of ^{3}He is greater in the gas-like dilute phase than in the concentrated "liquid" phase, the dilution process involves an increase in the total entropy of the system. To compensate for the rise in entropy, heat must be extracted from the system and whatever is thermally connected to it, in this case the solid ^{3}He target.

In order to make this cooling process continuous, ^{3}He must be constantly added to the concentrated side of the mixing chamber. This is accomplished by recirculating the ^{3}He that is removed from the still. It is first re-condensed at 1 K by a pumped ^{4}He bath (the *cold plate*). The flow impedance beneath the condenser increases the condensation pressure in order to aid liquefaction. However, the returning liquid ^{3}He represents a substantial input of heat into the mixing chamber, and so heat exchangers are used to bring it into thermal equilibrium, first with the still and then with the dilute liquid that is being removed from the mixing chamber.

For the dilution refrigerator used in this experiment, a ^{3}He circulation rate of 500 μmoles/s was achieved by an Edwards 9B3 diffusion pump backed by a hermetically sealed mechanical pump (Alcatel Model 3063H). The refrigerator, as tested by the manufacturer, has a cooling power of 1.48 μW at 10 mK and an ultimate temperature of 4.5 mK.

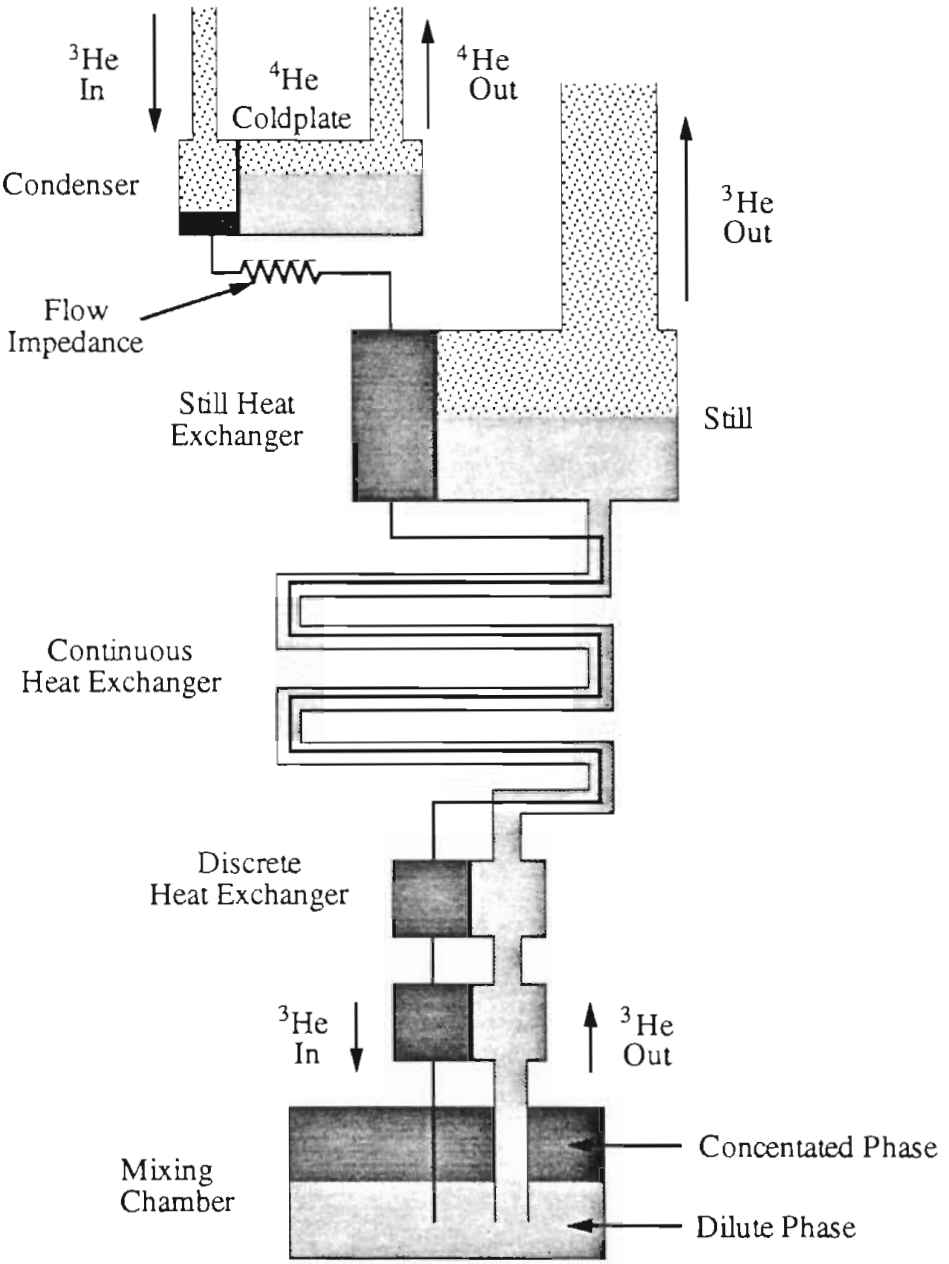

Figure 3.7: Simple model of a ^{3}He-^{4}He dilution refrigerator

3.2.2 ^{3}He Target Cell and Gas Handling System

There are three guiding concerns that have been considered in the overall design of the solid ^{3}He target. Foremost among these, the sample container must provide good thermal contact between the solid ^{3}He and the dilution refrigerator. Secondly, the design must incorporate the fact that it is intended for a neutron scattering experiment. Thirdly, the design must facilitate measurement of the ^{3}He polarization.

The ^{3}He target is shown in Fig. 3.8. The sample container was constructed by the instrument shop of North Carolina State University and is composed of three separate sections which will be referred to as top, middle and bottom. Beryllium copper (BeCu), a 2% beryllium alloy of copper, was chosen as the primary construction material because it combines excellent thermal and mechanical properties. The use of this material poses one potential problem: copper (and to a lesser extent, beryllium) may introduce an unwanted, spin-dependent neutron-transmission asymmetry in addition to the ^{3}He asymmetry of interest. This is a topic that will be addressed later. However, the search for a more suitable material should play an important role in the development of future targets.

The top portion of the target provides the most direct thermal connection between the solid ^{3}He and the dilution refrigerator. For this reason, it is constructed of annealed OFHC copper, which has greater thermal conductivity than BeCu, and is silver-soldered to the main section. The bottom section is BeCu and serves as a reusable vacuum seal.

The middle section is in the shape of a right, circular cylinder of 28.6 mm diameter and 54.0 mm long. Four flat faces were machined from the cylinder and serve two purposes. First, this reduces the amount of BeCu that is cooled by the refrigerator. More importantly, the neutron attenuation due to BeCu is thus minimized and is constant over the surface defined by the beam. The wall thickness at the flats is 1.27 mm perpendicular to the beam, and 2.54 mm parallel to the beam.

The interior sample space (shown in gray in Fig. 3.8) is a rectangular parallelpiped with a cross-sectional area 38.1×14.0 mm and 21.6 mm thick. The rectangular shape of the target maximizes the thickness of solid ^{3}He. The sample space is filled with 3 μm silver powder packed to 19% of the density of solid silver. This packing fraction was determined by weighing the cell before and after it was filled with powder and dividing by the inner volume of the cell. As indicated by Fig. 3.8, the lower portion

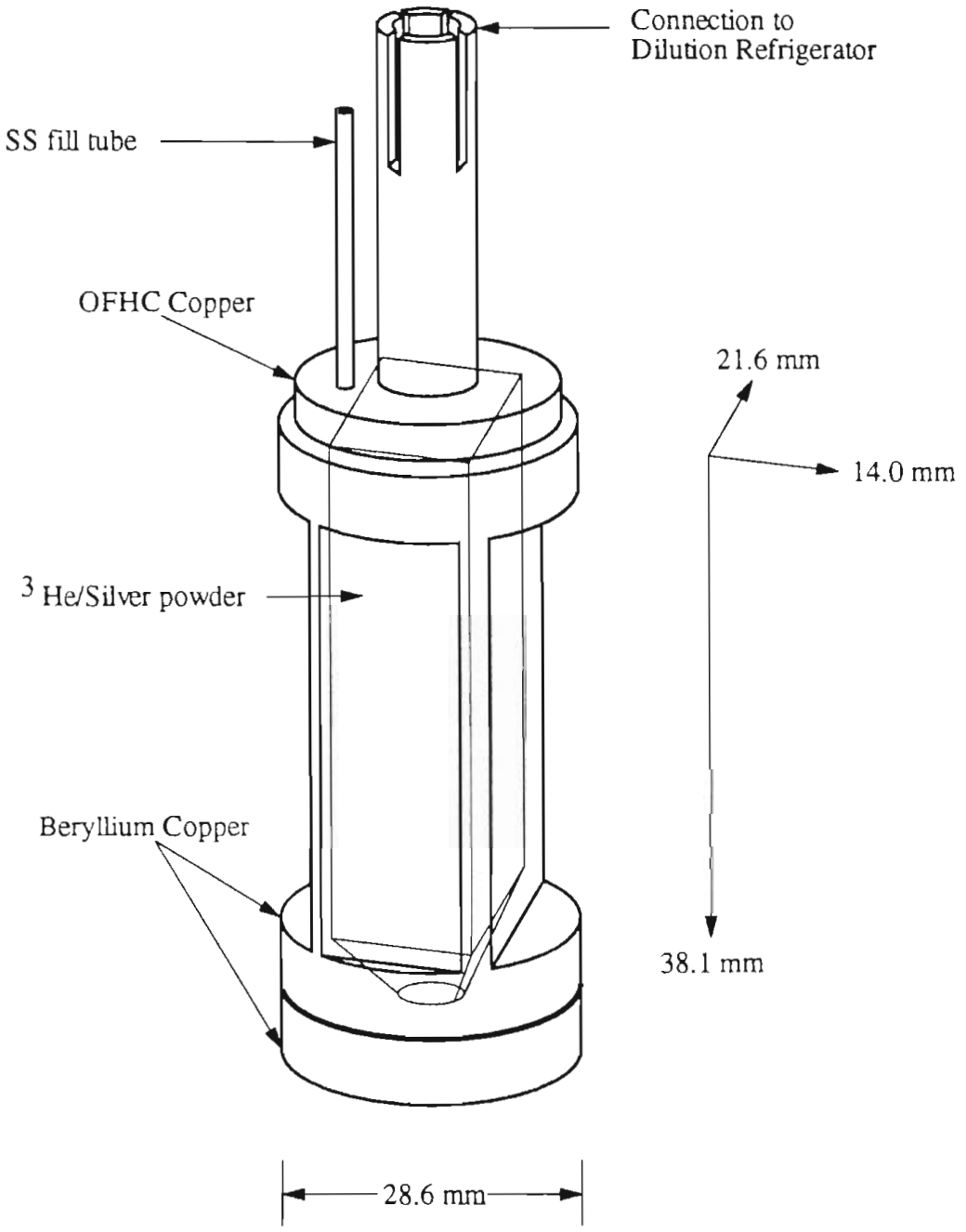

Figure 3.8: The TUNL polarized solid ^{3}He target. The sample space is indicated by the gray shaded portion. The interior dimensions of the target are shown to the right.

of the sample space is funnel-shaped to facilitate an even fill of silver powder.

The silver powder serves two purposes. First, it ensures that the temperature (and therefore the polarization) of the target is homogeneous throughout. The thermal conductivity of the silver "sponge" is estimated [Bus84] to be $\mathcal{K}_{Ag}/T = 1$ W/K^2 m. The conductivity of 24.0 cm^3/mole solid ^{3}He has been measured [Gre79] to be (roughly) $\mathcal{K}_3/T^3 = 2000$W/K^4 m. Thus, at 10 mK

$$\mathcal{K}_{Ag} = 10 \frac{\mathrm{W}}{\mathrm{K\,m}} \tag{3.7}$$

$$\mathcal{K}_3 = 2 \frac{\mathrm{W}}{\mathrm{K\,m}}. \tag{3.8}$$

The powder increases the thermal conductivity of the target by approximately a factor of five at 10 mK.

Second, the powder provides essential thermal contact between the solid ^{3}He and the copper/BeCu sample container. The greatest difficulty that must be overcome in cooling samples of solid or liquid ^{3}He is the thermal boundary, or Kapitza, resistance between the helium and the metal container. Transfer of heat between the two materials is accomplished primarily through the coupling of phonons in the helium with phonons in the metal. If, however, the phonon mean free path differs dramatically for the two materials, the phonon wave will be partially reflected at the boundary between them, and the flow of heat is consequently impeded. Acoustic mismatch theory predicts (see Section 9.6 in Lounasmaa [Lou74])

$$R_K = \frac{\mathcal{R}_K}{AT^3} \tag{3.9}$$

where $\mathcal{R}_K$ is the characteristic Kapitza resistivity between the two materials and A is the surface area between them. Experimentally, R_K has been found to vary as $1/T$ for the case of ^{3}He and sintered silver powder. Mamiya *et al.* have measured

$$R_K = \frac{2 \times 10^6}{T(\mathrm{mK})} \frac{\mathrm{m^2K}}{\mathrm{W}} \tag{3.10}$$

for the interface between solid ^{3}He and 700 Å sintered silver powder [Mam83]. We estimate that the 24 g of silver powder inside the TUNL target provides approximately 12 m^2 surface area. Using these values of A and $\mathcal{R}_K$ we conclude that the Kapitza resistance at 10 mK is about

$$R_K = 17 \frac{\mathrm{K}}{\mathrm{mW}}. \tag{3.11}$$

Due to Van der Waals forces between ^{3}He and silver, the portion of ^{3}He in "direct contact" with the powder may possess a greater density than that of the bulk solid. Such behavior has been observed [Lan79] in ^{3}He adsorbed onto carbon substrates (in the form of graphite or grafoil, which have enormous surface-to-mass ratios). However, this adsorbed phase of ^{3}He extends only a couple of monoatomic layers (say 10 Å) beyond the substrate. The volume of ^{3}He adsorbed on the 12 m^2 silver powder is then estimated to be about 1×10^{-4} cm^3—a minor fraction of the total ^{3}He volume.

After the powder is packed, the target cannot be sealed by welding or hard-soldering because the temperatures involved would very likely melt the silver powder. With this in mind, the bottom section is attached with six no. 4-40 non-magnetic stainless steel screws. This section includes a 9.4 mm diameter, 6.4 mm high cylindrical flange that is inserted in the funnel-shaped portion of the middle section and sealed with an indium O-ring. With the powder and bottom flange in place, the total volume available to the ^{3}He is 9.40 cm^3. However, a portion of this volume is contained in the funnel and does not really contribute to the neutron scattering. The available volume in the parallelpiped section is 9.00 cm^3.

The cell is thermally anchored to the mixing chamber by a 45 cm long OFHC copper rod (the *cold finger*). The diameter of this rod is 9.52 mm at the mixing chamber and 6.35 mm at the target. Since the 0.5 K heat shield in Fig. 3.6 does not extend to the level of the target, the latter is exposed to 4 K radiation from the LHe bath. To improve its emissivity, the target (and part of the coldfinger) is wrapped with one layer of 6.4 μm thick aluminized mylar.

The sample cell is filled with ^{3}He through a 0.76 mm I.D. stainless steel tube that is silver-soldered into the top section of the cell. Copper-nickel capillary (0.1 mm I.D.) is used to connect the stainless steel fill tube to a room temperature gas handling system. The capillary is heat sunk to the mixing chamber, still and cold plate.

The ^{3}He gas handling system is shown in Fig. 3.9. All tubing is 0.76 mm I.D. stainless steel. The ^{3}He is stored at approximately 10 bars in four 1/3 liter lecture bottles. The ^{3}He is pumped from these bottles and compressed into the rest of the gas handling system by the use of two adsorptive "dip-sticks" that are filled with activated charcoal. A 60 cm^3 per stroke pressure intensifier[6] is used to adjust the pressure, which is measured with a high precision 0–69 bar bourdon tube. In the

[6]High Pressure Equipment Corp., Erie, PN.

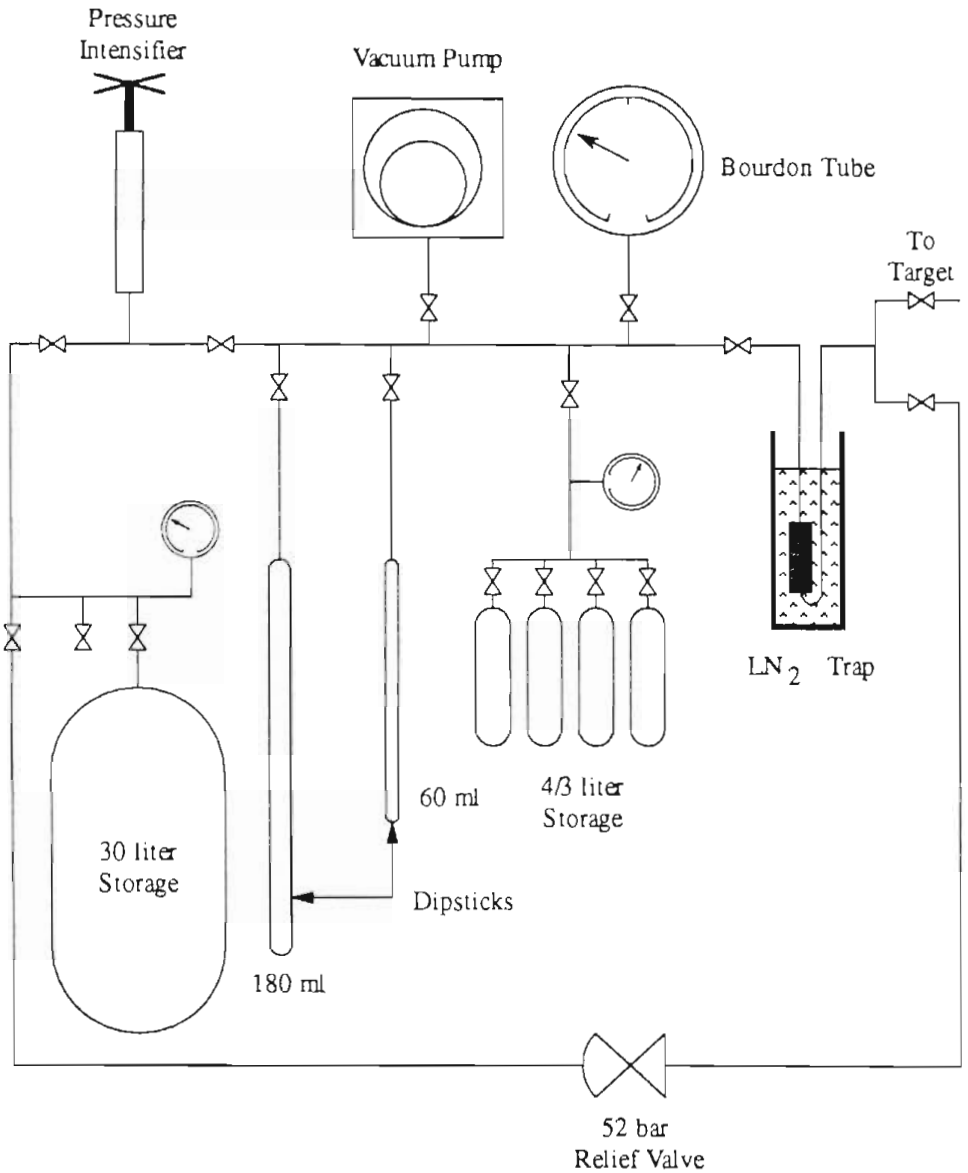

Figure 3.9: The gas handling system for the polarized ^{3}He target.

event of accidental over-pressurization of the target, a 52 bar relief valve is placed between the target and an evacuated, 30 liter container. The total volume of gas necessary to operate the TUNL target is approximately 20 liters, or about 1 mole of ^{3}He.

The target cell is filled with ^{3}He and cooled to 4 K. At this temperature, liquefacation occurs when the ^{3}He vapor pressures exceeds a few atmospheres. After the cell is completely filled with liquid, the vapor pressure is increased to 45.5 bar and the ^{3}He-^{4}He dilution refrigerator is started. Solid begins to condense inside the target at 1.2 K. The vapor pressure is maintained at 45.5 bar until the copper-nickel capillary is completely blocked with solid. At this point, a constant number of ^{3}He atoms are sealed inside the sample cell. Hence, the density of the sample remains constant even as liquid continues to solidify inside the cooling target. This method of preparing an isopycnic sample is known as the "blocked capillary" technique. Figure 3.3 indicates that the sample is completely solidified at 36 bar and 0.86 K.

The solidification process can be observed by watching the cooling rate of the target. When liquid is converted to solid, the refrigerator must carry off the resultant latent heat of solidification, about 1.5 Joules. The latent heat is completely removed when the entire target is solidified, and the cooling rate of the refrigerator increases.

3.3 Thermometry

Special attention must be shown to the thermometry used to measure the sample temperature. This is the only method used to determine the sample polarization. Great care has been taken to ensure that the solid ^{3}He is in good thermal contact with the BeCu cell, and that the temperature of the sample is constant throughout its volume. Therefore, thermometry provides an accurate measure of the bulk nuclear polarization. We have used two independent primary thermometric standards to determine the sample temperature: a ^{60}Co nuclear orientation thermometer, and a ^{3}He melting curve thermometer. Comprehensive reviews of nuclear orientation and ^{3}He melting curve thermometry can be found in Marshak [Mar83] and Greywall [Gre86], respectively. The two techniques are compared in Keith *et al.* [Kei92].

Both thermometers are mounted on a copper plate that is attached to (but thermally isolated from) the copper coldfinger. A 23 cm long copper braid provides

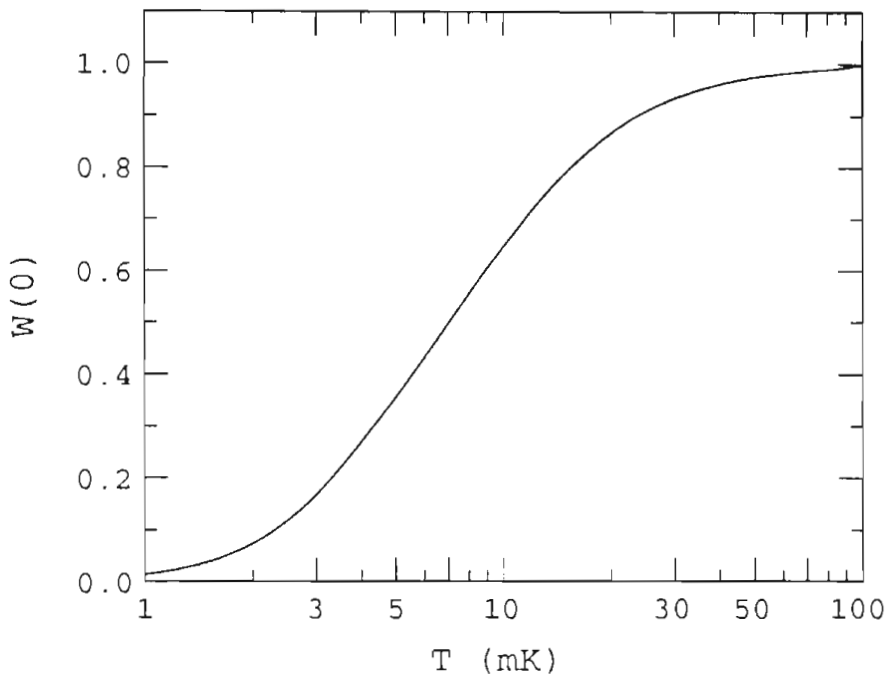

Figure 3.10: The ^{60}Co γ-ray anisotropy ratio $W(0°)$ as a function of temperature.

thermal connection between the plate and the top portion of the sample cell. The thermal conductance of the braid is calculated to be $K/T = 5.6$ mW/K^2. The field of the superconducting magnet has been measured to be 0.16 Tesla at this location and has a negligible effect on the ^{60}Co and melting curve thermometers. In addition to these two thermometers, a variety of resistive thermometers is used to monitor the temperature throughout the cryostat as well as the target.

3.3.1 ^{60}Co Nuclear Orientation Thermometry

The ^{60}Co nuclear orientation thermometer (or simply NO thermometer) consists of a small, single crystal of hcp cobalt, activated with approximately 4–6 μCi of ^{60}Co. The half-life of ^{60}Co is 5.27 years, and in the process of its β-decay into ^{60}Ni, it emits two γ-rays with energies of 1173 and 1332 keV. Both γ-rays are the result E2 transitions and display a dipole radiation pattern if the ^{60}Co nuclei are aligned about some axis. The alignment field is provided by the internal magnetic field of the cobalt crystal,

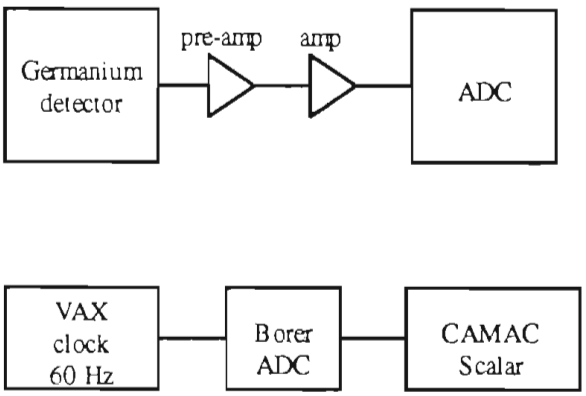

Figure 3.11: Data acquisition electronics for the nuclear orientation thermometer.

21.9 Tesla. A γ-ray detector (an intrinsic germanium detector) is placed outside the cryostat at an angle θ with respect to the cobalt c-axis. As the ^{60}Co nuclei align at low temperatures, a change in the number of γ-rays detected at θ is observed. The ratio of "warm counts" to "cold counts" is $W(\theta)$. "Warm" may be considered to be any temperature greater than approximately 0.1 K. The warm data may be acquired immediately before the sample is cooled below 0.1 K, or at the end of the experiment, when the dilution refrigerator is shut off. A graph of $W(0°)$ versus temperature is given in Fig. 3.10.

The data acquisition electronics for the γ-ray detector are shown in Fig. 3.11. To avoid damage due to background radiation, the detector must be removed during the neutron experiment. Therefore, ^{60}Co counts are recorded one hour prior to, and after, each neutron asymmetry measurement, and an average target temperature is calculated from the results. A table is mounted to the cryostat support structure that allows the detector to be consistently placed in the same location with respect to the cobalt crystal.

Typical counting rates are approximately 3 s^{-1} for either the 1173 or 1332 keV peak, and a typical γ-ray spectrum is shown in Fig. 3.12. For each peak, $W(0°)$ is determined on the basis of ten 5-minute counting intervals. The two values of $W(0°)$ are averaged, and the corresponding temperature then determined. The error in this temperature is dictated primarily by the counting statistics and is given by

$$\Delta T = \frac{\Delta W}{\partial W/\partial T} \tag{3.12}$$

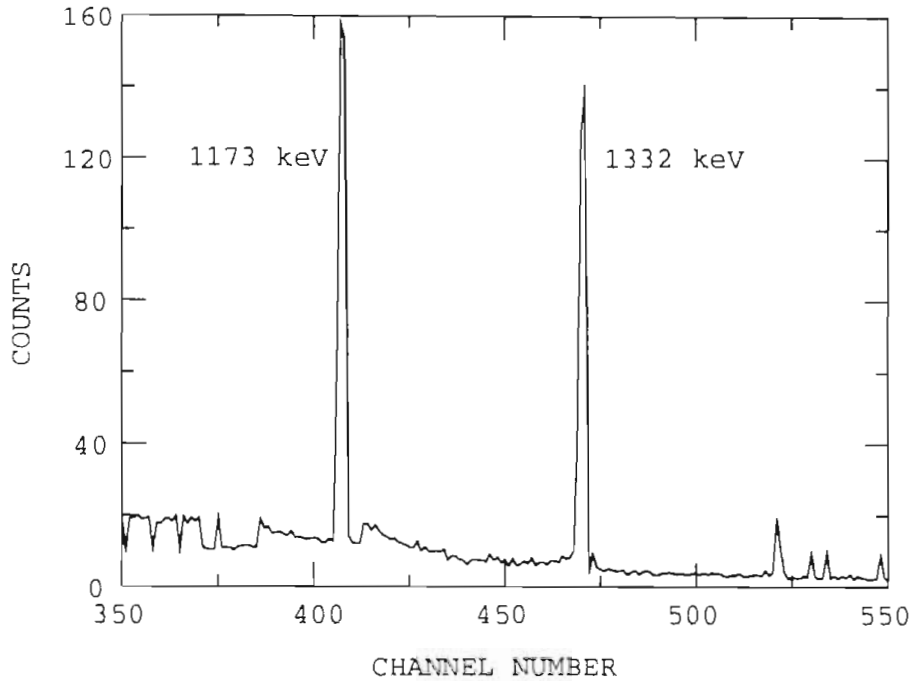

Figure 3.12: A typical γ-ray spectrum of the ^{60}Co thermometer.

where

$$\Delta W = W\,[\frac{1}{N_w} + \frac{1}{N_c}]^{1/2}. \tag{3.13}$$

The total number of warm and cold counts are N_w and N_c, respectively. Below 20 mK, a 2% measure of the temperature requires approximately 2 hours.

Because of the low activity of the cobalt crystal, radioactive heating is estimated to be quite low—0.35 nW (cf. Marshak, Section 3.7 [Mar83]).

3.3.2 ^{3}He Melting Curve Thermometry

It was noted in Section 3.1.1 that a sample of melting ^{3}He could be made to follow the melting curve all the way to absolute zero. This is the basis for the ^{3}He melting curve thermometer (MCT). As shown in Fig. 3.13, the MCT consists of a small capacitive strain gauge that is used to measure the melting pressure of ^{3}He. The pressure can be determined with a precision of a few μbar by detecting changes in capacitance

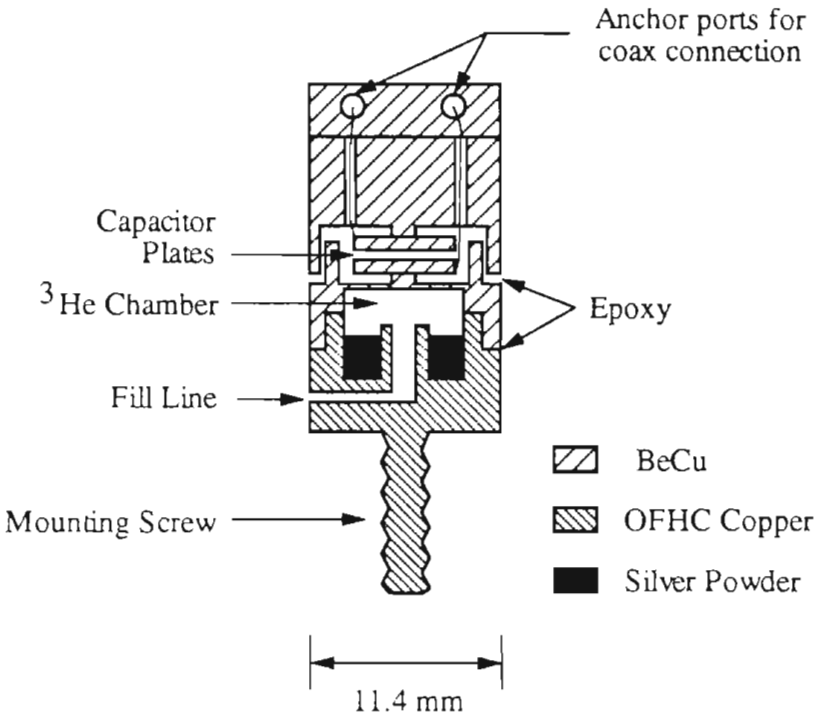

Figure 3.13: ^{3}He melting curve thermometer

as small as 5 ppm. Except for the region near P_{min}, the slope of the melting curve is quite steep, $\sim$ 30 mbar/mK, so that the MCT can provide an extremely precise measure of the temperature. At 15 mK the resolution of the TUNL melting curve thermometer is approximately 1 μK.

The MCT gas handling system is essentially identical to the one described in Section 3.2.2. A pressure *versus* capacitance calibration must be performed at 1 K over the range 27.5–35 bar. The capacitance (which is generally of order 10 pF) is measured with General Radio 1615-A capacitance bridge, while the pressure is measured with a high precision bourdon tube. A phase-sensitive lock-in amplifier is used to determine a null signal from the capacitance bridge. The P *vs.* C calibration data is then least-squares fit to the formula

$$P(C) = a_1 + a_2 C^{-1} + a_3 C^{-3}. \tag{3.14}$$

An experimental determination of P_{min} is made while the target is cooling, and the P *vs.* C calibration is adjusted to agree with the NIST-recommended value,

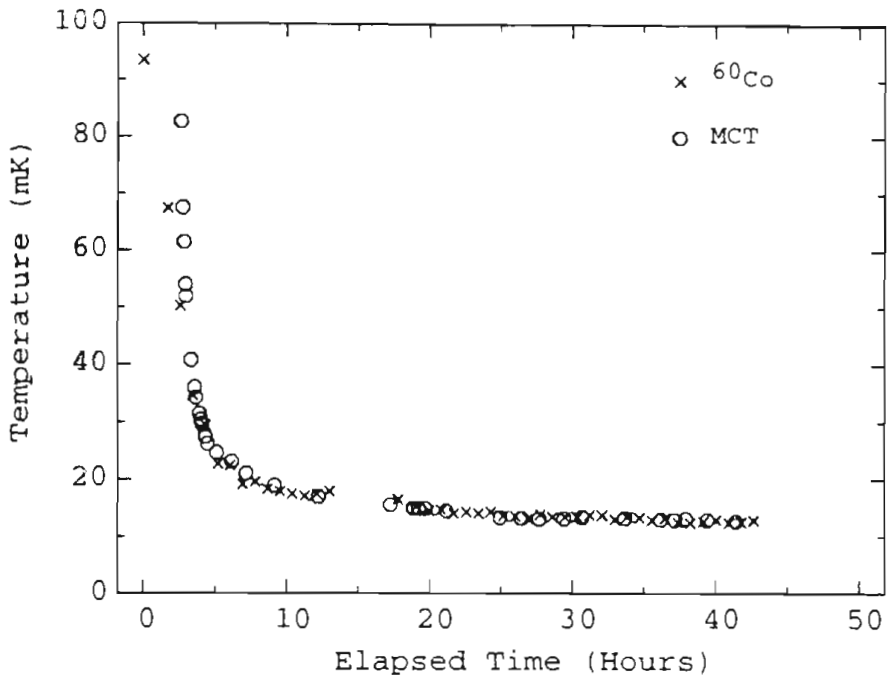

Figure 3.14: Cooling curve for the ^{3}He target. Temperatures are measured with the ^{60}Co nuclear orientation thermometer (crosses) and the ^{3}He melting curve thermometer (circles).

P_{min} = 29.3118 bar [Fog92]. The accuracy of the MCT is primarily determined by the residuals of the least-squares fit, typically less than 10 mbar. The temperature corresponding to an experimentally-determined melting pressure is based on the NIST melting curve [Fog92]. A cubic-spline interpolation routine is used. A 10 mbar pressure accuracy translates to $\Delta T/T \simeq 2\%$ in the 10–15 mK temperature region.

In addition to the high precision offered by the MCT, it has one other advantage over the ^{60}Co thermometer. Since it is largely unaffected by radiation, the MCT can be used to measure the target temperature during the actual neutron experiment. The output voltage of the lock-in amplifier is read by the TUNL data acquisition computer for each spin-flip signal generated by the TUNL spin-state controller (see Chapter 4 for additional details). The voltage can then be converted to an out-of-balance capacitance and eventually a target temperature. An average MCT temperature for each neutron asymmetry measurement can thus be determined in this manner. An

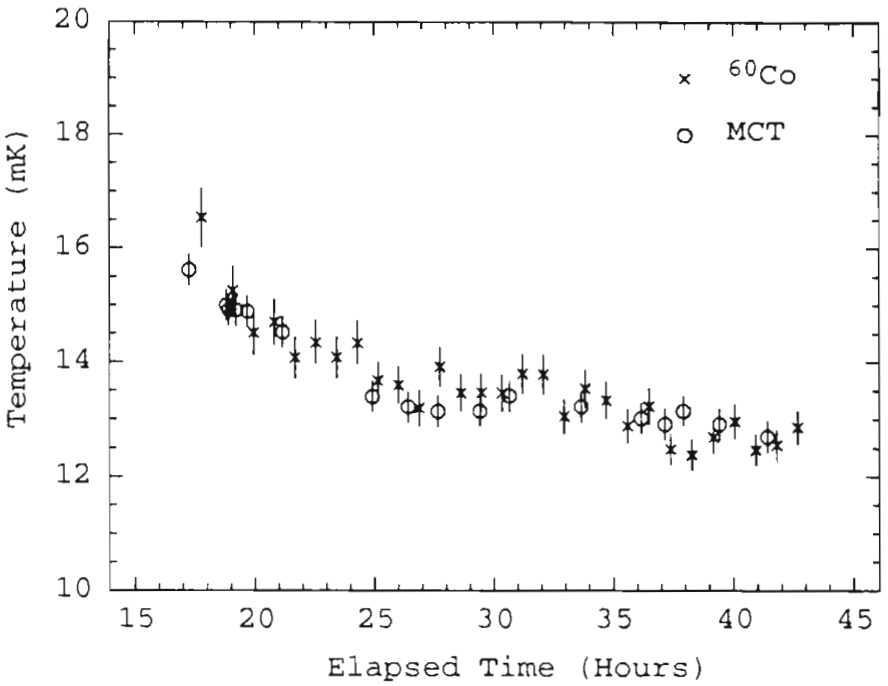

Figure 3.15: Cooling curve for the ^{3}He target below 20 mK. Temperatures are measured with the ^{60}Co nuclear orientation thermometer (crosses) and the ^{3}He melting curve thermometer (circles).

asymmetry measurement typically requires 6–12 hours. The average MCT temperature can then be compared to the average ^{60}Co temperature. The latter is average of the ^{60}Co temperature before and after the neutron asymmetry measurement. Results are discussed in Chapter 5.

A typical cooling curve for the target below 100 mK is shown in Fig. 3.14. Once circulation of the ^{3}He-^{4}He mixture is commenced at 1 K, cooling to 100 mK requires less than two hours. The low-temperature (< 20 mK) portion of Fig. 3.14 is expanded in Fig. 3.15. In this temperature range the temperatures determined by the ^{60}Co and melting curve thermometer are found to agree to within ±2%.

Nuclide	Spin I	μ (nm)	τ (10^{22} cm^{-2})	P (12 mK, 7 T)	τP (10^{22} cm^{-2})
^{3}He	1/2	-2.1276	4.34	0.371	1.610
Silver	1/2	-0.1217	2.40	0.026	0.062
Copper	3/2	2.2750	1.93	0.380	0.733
Beryllium	3/2	-1.1776	0.25	0.206	0.052
Cobalt	7/2	4.6490	0.01	0.832	0.008

Table 3.2: An inventory of materials in the BeCu sample container

3.4 Inventory of Target Materials

In addition to solid helium, the sample container contains four other elements, each of which can in principle contribute to the measured spin-spin asymmetry. The four elements are beryllium, cobalt, copper and silver. The beryllium content in BeCu is approximately 1.8%. BeCu also contains a small amount of cobalt, typically ~0.5%. Both beryllium and cobalt are monoisotopic (^{9}Be and ^{59}Co), while copper and silver each have two stable isotopes (^{63}Cu, ^{65}Cu, ^{107}Ag, and ^{109}Ag). Each isotope has a non-zero magnetic moment and is polarized to some extent by the 7 Tesla polarizing field. Note that because of its negative magnetic moment, ^{3}He polarizes in a direction opposite that of the magnetic field.

Table 3.2 lists the relevant parameters for the four nuclides mentioned above as well as ^{3}He. The areal density is calculated as

$$\tau_i = \rho_i x_i \tag{3.15}$$

where ρ_i is the density in atoms/cm^3 of the i^{th} isotope, and x_i is the thickness of material (in cm) transversed by the neutron beam. The vector polarization is calculated as[7]

$$P_i = \frac{2I_i+1}{2I_i}\coth\left[\frac{2I_i+1}{2}\frac{\mu_i B}{kT}\right] - \frac{1}{2I_i+1}\coth\left[\frac{1}{2}\frac{\mu_i B}{kT}\right], \tag{3.16}$$

assuming 12 mK and 7 Tesla. The magnetic moments μ_i listed in Table 3.2 are averaged values for all stable isotopes, weighted by their relative abundances.

In terms of density times polarization, ^{3}He is the dominant species. Evidence (or lack thereof) of unwanted contributions to ε_{ss} will be discussed in Chapter 5.

[7] Equation (3.4) is used to calculate the polarization of ^{3}He.

3.5 Sources of Beam-Related Heating

We investigate four potential sources of beam-related heating. This issue is important, owing to the low temperatures that are necessary for the operation of the polarized ^{3}He target. The cooling power of the dilution refrigerator is 1.5 μW at 10 mK, making the target polarization sensitive to heat inputs that exceed a few tenths of a microwatt. Heat is generated when high-energy (MeV) charged-particles are stopped inside the ^{3}He target or its BeCu container. The moving charged particles are either the result of neutron-induced reactions or are recoiling from an elastic scattering event.

As a starting point, we note that the total power contained in a beam of 5 MeV neutrons is approximately 1 $\dot{N}$ pW, where $\dot{N}$ is the number of neutrons per second that illuminate the polarized target. Hence a flux of 10^6 neutrons/s can produce at most 1 μW of heat.[8] For the deuterium gas cell and beam collimation system described in the next chapter, we estimate a target illumination of approximately 2×10^5 neutrons per second for each microampere of deuteron beam current. Typical beam currents during the neutron-transmission measurements were of order 1/2 μA. Additionally, the flux must be weighted by the neutron total cross, which for ^{3}He is about 2.5 b at 5 MeV. For a ^{3}He thickness of 4.3×10^{22} atoms/cm^2, only 10% of the incident neutrons are attenuated by ^{3}He. Another 15% of the neutrons are attenuated by other materials in the BeCu container (primarily silver and copper). Approximately half of the neutron total cross section is due to elastic scattering—a process that deposits little heat in the ^{3}He lattice.

The sources of beam-related heating that will be considered are:

1. The elastic scattering of MeV neutrons;

2. Compton scattering of MeV γ-rays;

3. Nuclear reactions induced by thermal and epithermal neutrons;

4. Nuclear reactions induced MeV neutrons.

We expect the first process to contribute a significant amount of heat only when the neutrons scatter from ^{3}He. In this case the nucleus is not much heavier than

[8] This estimation ignores neutron-induced reactions with positive Q-values.

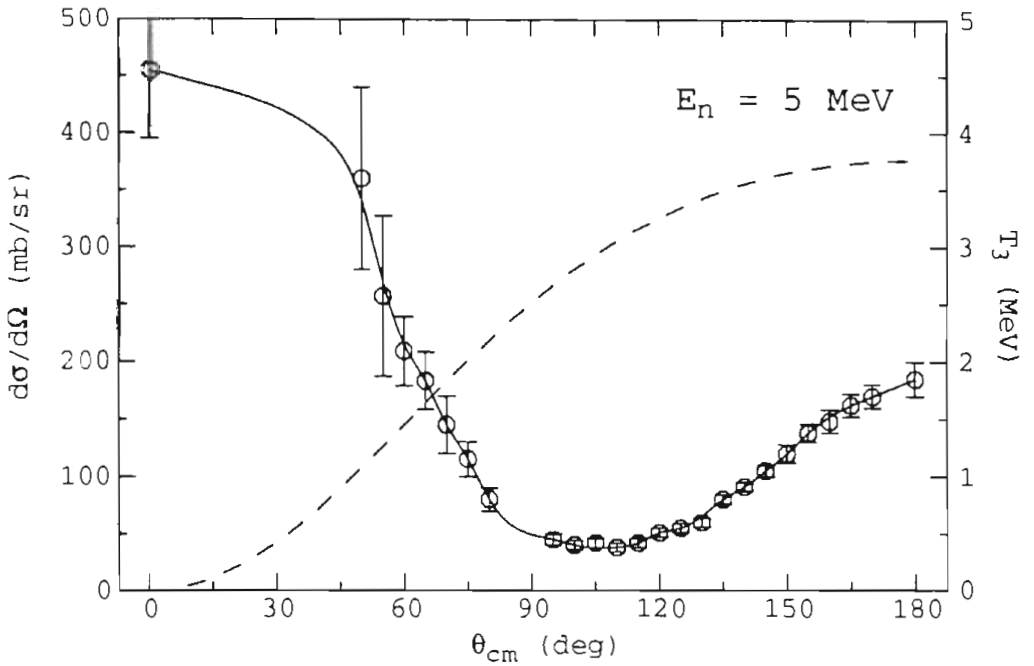

Figure 3.16: Energy of the recoiling ^{3}He nucleus, T_3, for neutron elastic scattering at 5 MeV (dashed line). The differential cross section (solid line) at 5 MeV is also shown [Say61].

the incident neutron itself, and so may recoil with a considerable portion of the beam energy. Because they are much more massive, and because their differential cross sections are forward-peaked, the copper and silver nuclei recoil with much less energy. We will calculate the heating produced by the elastic scattering of 5 MeV neutrons from solid ^{3}He.

The energy of the recoiling ^{3}He nucleus is a function of the scattering angle θ. This is shown in Figure 3.16 for an incident beam energy of 5 MeV. The probability for scattering into angle θ is given as the ratio of the differential cross section, $d\sigma(\theta)$, to the total cross section for elastic scattering, σ^e_{tot}. The differential cross at 5 MeV is also shown in Figure 3.16. The total heat produced when the recoiling ^{3}He are stopped in the target is

$$H_{n,n} = 2\pi \dot{N}(1 - e^{-\sigma^e_{tot} r_3}) Q_3 \int_0^\pi T_3(\theta) \frac{d\sigma(\theta)}{\sigma^e_{tot}} \sin(\theta)\, d\theta. \qquad (3.17)$$

The term in parenthesis is the fraction of incident neutrons that scatter elastically,

and Q_3 is the electric charge of the ^{3}He nucleus. Evaluated numerically for 5 MeV neutrons, Eq. 3.17 reduces to

$$H_{n,n} = \dot{N}\left(3.9 \times 10^{-2}\ \mathrm{pW\,s}\right), \tag{3.18}$$

or approximately 8 nW for 2×10^5 neutrons per second. This is less than 1/100 of the refrigerator's cooling power at 10 mK.

We now consider the heating due to γ-radiation. The γ-rays are produced either by neutron-induced reactions, or when the charged-particle beam is stopped at the end of the beam line (see Section 4.2.1). The latter is expected to be the dominant process. We will not attempt to make a detailed estimate of the number of γ-rays that illuminate the polarized target, or of their average energy. Time-of-flight measurements indicate that about one γ-ray is detected at 0° for every ten neutrons. The maximum energy of the γ's is probably of order 1–5 MeV, the energy of the charged-particle beam.

The three main mechanisms by which γ-rays interact with matter are the photoelectric effect, electron-positron pair production, and Compton scattering. The photoelectric effect is the dominant mechanism for γ-rays with energy less than about 500 keV. It is unlikely that these low-energy γ-rays can penetrate deeply enough into the spin-spin cryostat to pose a serious threat to the ^{3}He target. Pair production becomes the dominant mechanism only at energies above 10 MeV. Since this is greater than the energy of the charged-particle beam, pair production inside the target is extremely rare. The third process, Compton scattering, is important for E_γ between 0.1–10 MeV. We will investigate the heat generated by Compton scattering on copper, silver, and helium at the center of the polarized target. That is, we will assume that the γ-rays are as tightly collimated as the incident neutron beam. The validity of this assumption is certainly questionable, but our calculation will give a rough idea of the amount of heating that can be expected.

Compton scattering is the scattering of photons from free electrons, and is described by the Klein-Nishina formula (see [Leo87] for additional details). The total cross section for this process is

$$\sigma_c^t = 2\pi\left(\frac{e^2}{m_e c^2}\right)\left\{\frac{1+x}{x^2}\left[\frac{2(1+x)}{1+2x} - \frac{1}{x}\ln(1+2x)\right] + \frac{1}{2x}\ln(1+2x) - \frac{1+3x}{(1+2x)^2}\right\}, \tag{3.19}$$

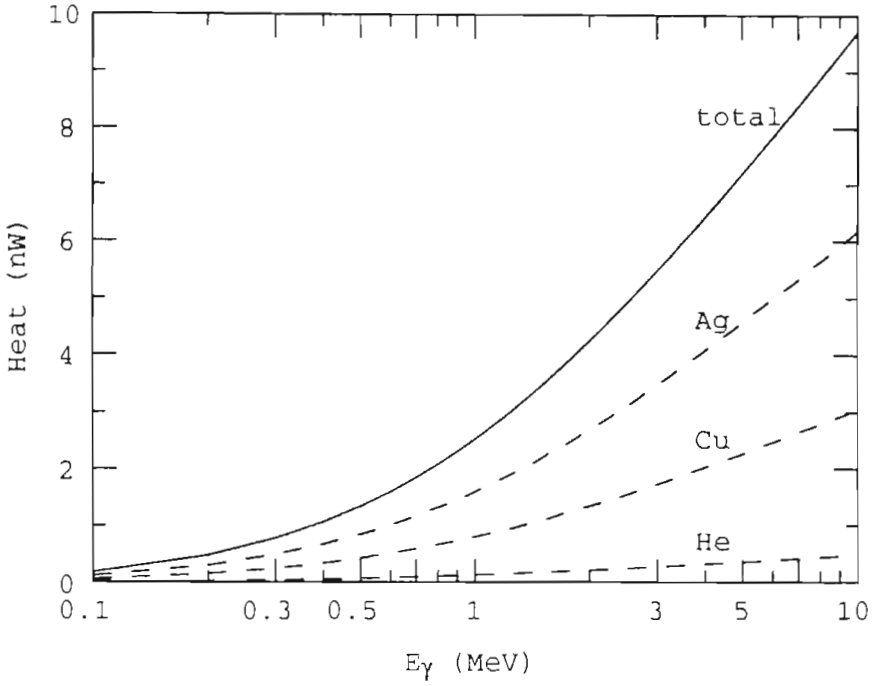

Figure 3.17: Heat generated by Compton scattering in the polarized ^{3}He target. Results assume an incident γ-flux of 10^5 s^{-1}.

where $x = E_\gamma/m_e c^2$. The average fraction of the total energy contained in the scattered photon is the Compton *scattered* cross section,

$$\sigma_c^s = \pi \left(\frac{e^2}{m_e C^2}\right) \left[\frac{1}{x^3}\ln(1+2x) + \frac{2(1+x)(2x^2-2x-1)}{x^2(1+2x)^2} + \frac{8x^2}{3(1+2x)^3}\right]. \quad (3.20)$$

The average energy that the photon imparts to the recoiling electron is the Compton *absorbed* cross section,

$$\sigma_c^a = \sigma_c^t - \sigma_c^s. \quad (3.21)$$

The Compton cross sections scales linearly with the atomic number Z of the element from which the photons scatter, so that the heat is

$$H_c = \dot{N}_\gamma e E_\gamma \left(1 - e^{-Z\tau\sigma_c^a}\right), \quad (3.22)$$

where τ is the areal density of the scattering material. Results for silver, copper, and helium are shown in Fig. 3.17. The areal densities chosen for these materials are

those from Table 3.2. The figure indicates that Compton-induced heating is a few nanowatts.

Perhaps the greatest source of potential heating is due to reactions induced by thermal neutrons on ^{3}He. The cross section for the $^3\mathrm{He}(n_{th},p)^3\mathrm{H}$ reaction is enormous (5300 barns). The Q-value for the reaction is 0.764 MeV, so the heat generated by each thermal-neutron capture inside the target is

$$H_{th} = 0.1\,\dot{N}_{th}\ \mathrm{pW\,s}. \tag{3.23}$$

We will make no estimate of $\dot{N}_{th}$. Neutrons are thermalized as they multiply-scatter from objects inside the experimental hall. Eventually, the room is filled with a "sea" of low-energy neutrons. Therefore, the dilution refrigerator's mixing chamber is as sensitive to this heat source as the ^{3}He target. One nW is generated by 10^4 thermal-neutron captures per second.

As a precaution, the lower part of the cryostat's vacuum can (see Fig 3.6) is wrapped with one layer of 0.5 mm thick cadmium foil. The thermal-neutron capture cross section of cadmium is also large, 2700 barns, primarily due to a resonance in the ^{114}Cd compound nucleus. The $n + {}^{113}$Cd reaction produces a variety of γ-rays as it decays to the ground state of ^{114}Cd. Over 90% of the γ's are below 5 MeV, with a maximum energy of 9 MeV. We have shown that the heating due to MeV γ-rays is not large.

Neutron-induced reactions at MeV energies are probably not so great a problem. Here the inelastic cross sections for ^{3}He, copper, and silver are respectively, 0.7, 3, and 2 barns, and the total attenuation of the neutron beam due to these cross sections is only 13%. If we take the incident beam energy (5 MeV) as the average value of the energy released during the inelastic collision, the total heat generated is

$$H_{inelas} = 0.1\,\dot{N}\ \mathrm{pW\,s}, \tag{3.24}$$

or about 20 nW for $\dot{N} = 2 \times 10^5$ neutrons per second.

All told, we expect a beam-related heat load less than 50 nW during the neutron transmission measurements.[9] This additional heat load should not severely affect the ultimate temperature of the ^{3}He target. We should assign about half of this heat load

[9]This assumes that the cadmium foil adequately shields the target and refrigerator from thermal neutrons.

directly to the ^{3}He, and the rest to the copper and silver inside the BeCu container. Assuming 20 nW is applied to the solid ^{3}He (at 12 mK) and using the Kapitza resistance measurements of Mamiya *et al.* [Mam83], we calculate a temperature difference between the ^{3}He and silver powder of less than 0.3 mK. This is within the errors assigned to T_3 in Section 5.3.

Chapter 4

The Polarized Neutron Beam

The majority of this chapter concerns the polarized neutron beam, how it is produced and how it is detected. Since the polarized neutrons result from reactions involving polarized charged particles, the chapter can be separated into two parts. We begin by describing the production and transport of the charged-particle beam. The production and detection of the secondary beam (the neutron beam) is described later.

4.1 Charged-Particle Beams

Two charged-particle reactions are used in this experiment to generate the polarized neutrons. To obtain polarized neutrons with energy 5 MeV or greater, the ^{2}H$(\vec{d},\vec{n})^3$He reaction is used. The ^{3}H$(\vec{p},\vec{n})^3$He reaction is used to create lower-energy neutrons. Because the deuteron possesses a nuclear spin of 1, the formalism that describes a polarized deuteron beam is slightly more complicated than that of the spin-1/2 proton. We will therefore concentrate on the former, and include additional information pertaining to the proton beam whenever the extrapolation is not obvious. In any event, the reader is referred to Ohlsen [Ohl72] for a comprehensive review of polarization in nuclear reactions.

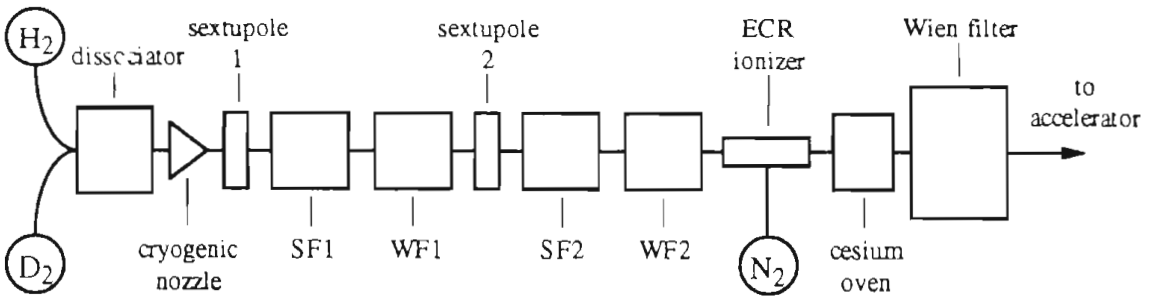

Figure 4.1: Block diagram for the Atomic Beam Polarized Ion Source. The strong field 1 cavity (SF1) is no longer in operation and has been removed.

4.1.1 The TUNL Polarized Ion Source

The TUNL Atomic Beam Polarized Ion Source (ABPIS) is capable of providing intense beams of vector- and/or tensor-polarized deuterons, as well as vector-polarized protons. Refer to Section 2.1 for the difference between vector and tensor polarization. This source is used in the majority of all experiments at TUNL nowadays, and so a short summary of its operation is in order. A simple block diagram is shown in Fig. 4.1. A more detailed description is given by Clegg *et al.* [Cle93].

Deuterium (or hydrogen) gas is injected into a water-cooled pyrex tube, where a 200 Watt discharge dissociates the D_2 (or H_2) molecules. The atoms are then slowed by drifting them through a copper nozzle cooled to 30 K. From the cold-nozzle, the atoms pass through the bore of a tapered sextupole magnet which serves as a Stern-Gerlach separator for the hydrogen or deuterium atoms. The magnetic field splits the atomic beam into two substates, depending upon the orientation of the electron's magnetic moment. The energy of the splitting is

$$W = \pm \mu_B B \tag{4.1}$$

where μ_B is the Bohr magneton, B is the magnitude of the magnetic field, and the $\pm$ sign depends on whether the electron has spin-projection m_j parallel or anti-parallel to the field direction. Because the sextupole's field is directed radially outward, W becomes a function of the atom's distance from the axis of the sextupole. Each atom then experiences a force

$$F = -\nabla W \tag{4.2}$$

which either pulls the atom towards the axis or pushes it away, depending on the

sign of W. In effect, the sextupole focuses atoms that are in one of the two electronic substates and defocuses the others. As a result, an "atomic-polarized" beam emerges from the sextupole. Since the sextupole's axis is along the direction of the beam, it prepares a beam that possesses cylindrical symmetry and whose spin-axis is also parallel to the direction of the beam.

Next the beam enters a series of cavities where radio-frequency (RF) oscillators are used to transfer the atomic polarization to nuclear polarization via the hyperfine coupling between electronic and nuclear spins. These RF oscillators can be tuned to frequencies that correspond to the difference in energy between certain hyperfine states, and hence induce transitions between the states. There are four of these RF transition units (with a second sextupole magnet placed between the second and third RF unit), so that a variety of final nuclear-spin states can be produced depending on the frequencies chosen for each transition unit. We shall refer to the four units as strong field-one and -two (SF1[1] and SF2), and weak field-one and -two (WF1 and WF2). The transition schemes that are used for this experiment are shown in Figs. 4.2 and 4.3 for the case of a deuterium beam, and in Fig. 4.4 for a hydrogen beam. Arrows are used in the figures to indicate the z-component of both the electron (small arrow) and nuclear (large arrow) spins in a given substate. The figures indicate that by toggling certain transition units on and off, the final direction of the nuclear spin is reversed. The TUNL spin-state controller (see Section 4.3) is used to control the toggling sequence.

The beam that exits the final RF transition unit is now nuclear-spin polarized and next enters the ECR ionizer region, where a plasma discharge is used to remove the electrons. The plasma is composed primarily of nitrogen, heated by microwave radiation. Electrons in this buffer gas are excited to high enough energies to strip the electrons from the deuteron (or hydrogen) beam. However, the tandem Van de Graaff requires negatively-charged ions for acceleration. The D^+ (H^+) beam is converted to D^- (H^-) through double charge exchange as it passes through a cloud of cesium vapor in the cesium oven indicted in Fig. 4.1. The slowly moving atoms are accelerated to 30 keV as they exit the cesium oven.

We have already noted that the first sextupole magnet defines a spin-axis that

[1]Actually, SF1 has been removed, but the remaining strong field transition unit continues to be referred to as strong field-*two*.

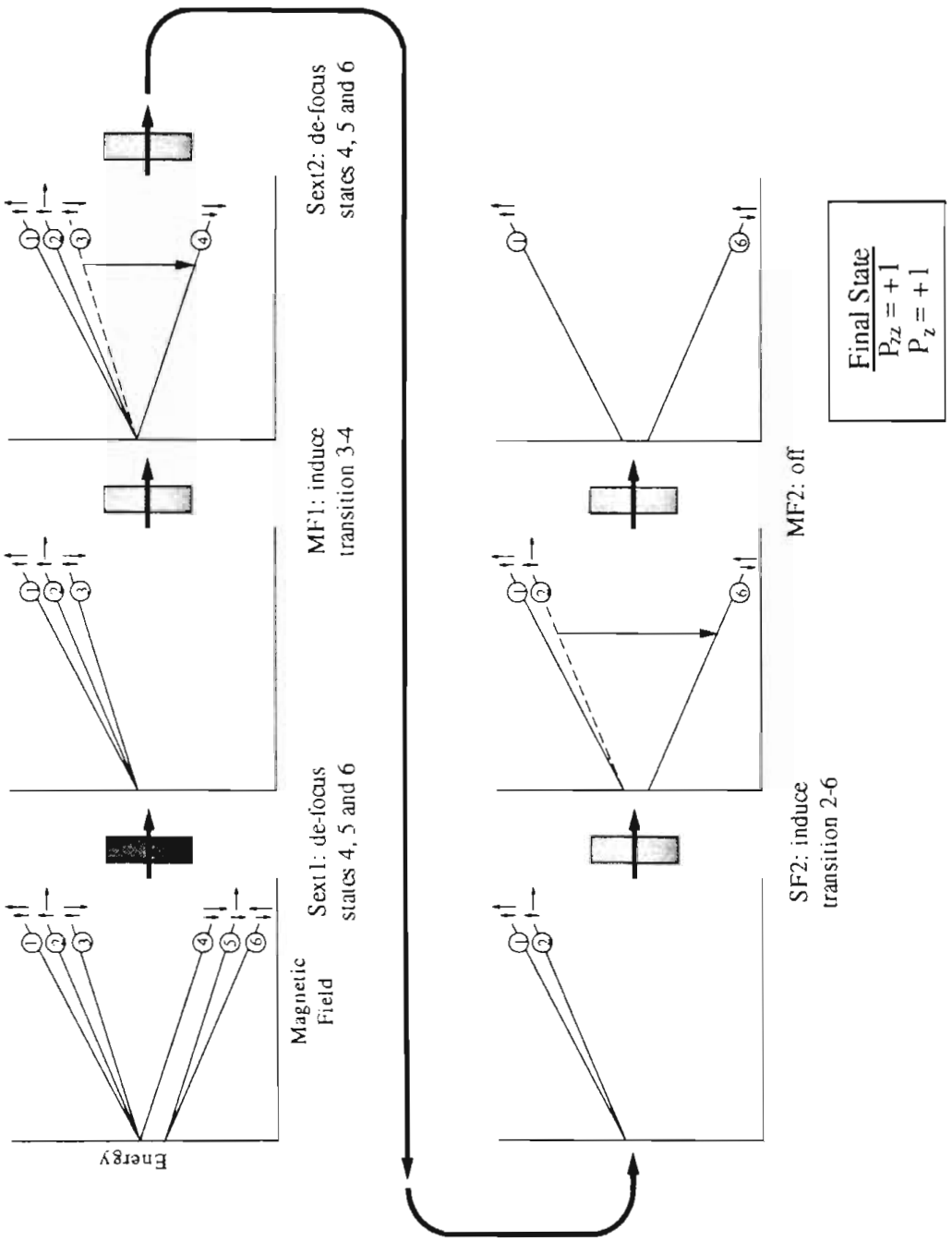

Figure 4.2: The ABPIS transition scheme used to produce a "spin-up" polarized deuteron beam. Strong field one is not used, and does not appear in the figure.

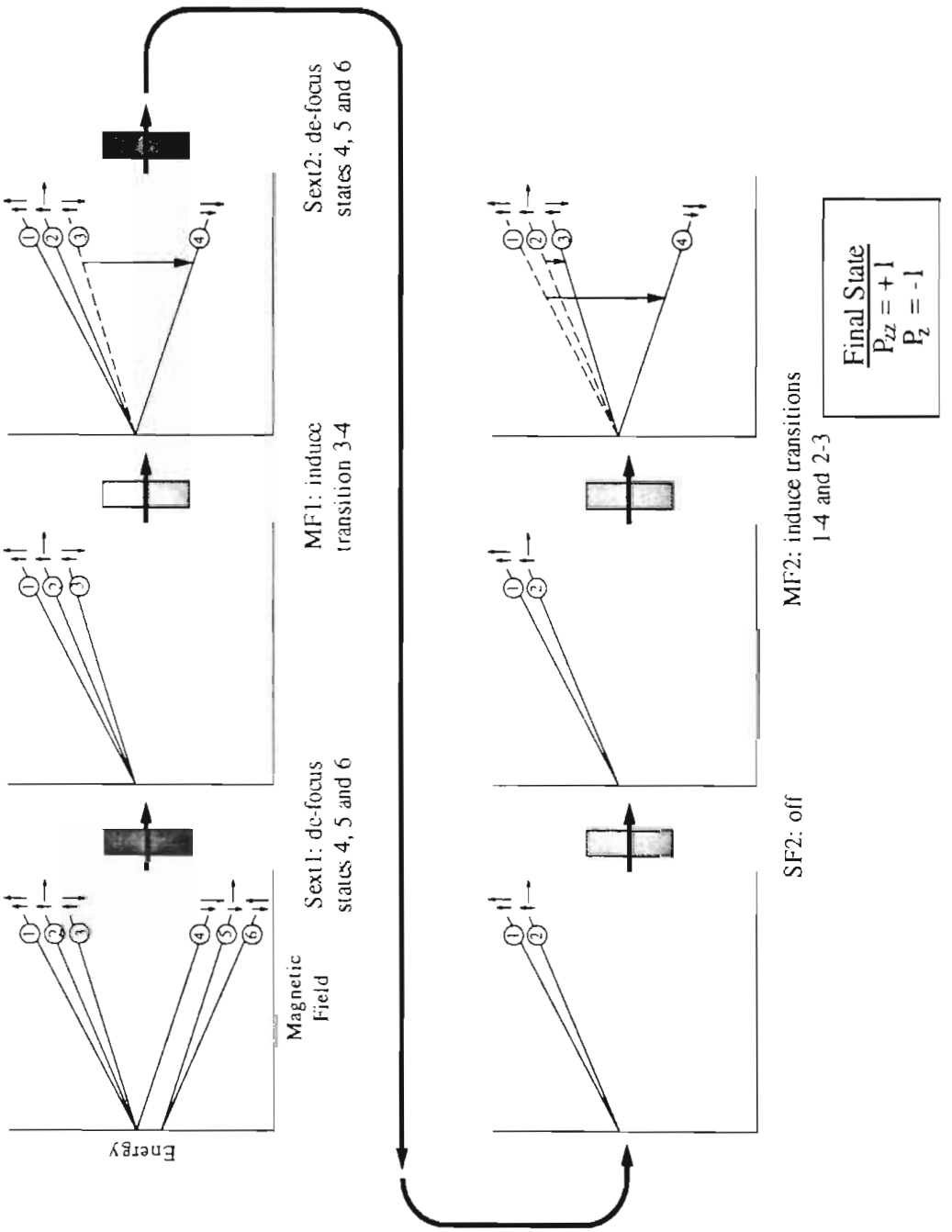

Figure 4.3: The ABPIS transition scheme used to produce a "spin-down" polarized deuteron beam. Strong field one is not used, and does not appear in the figure.

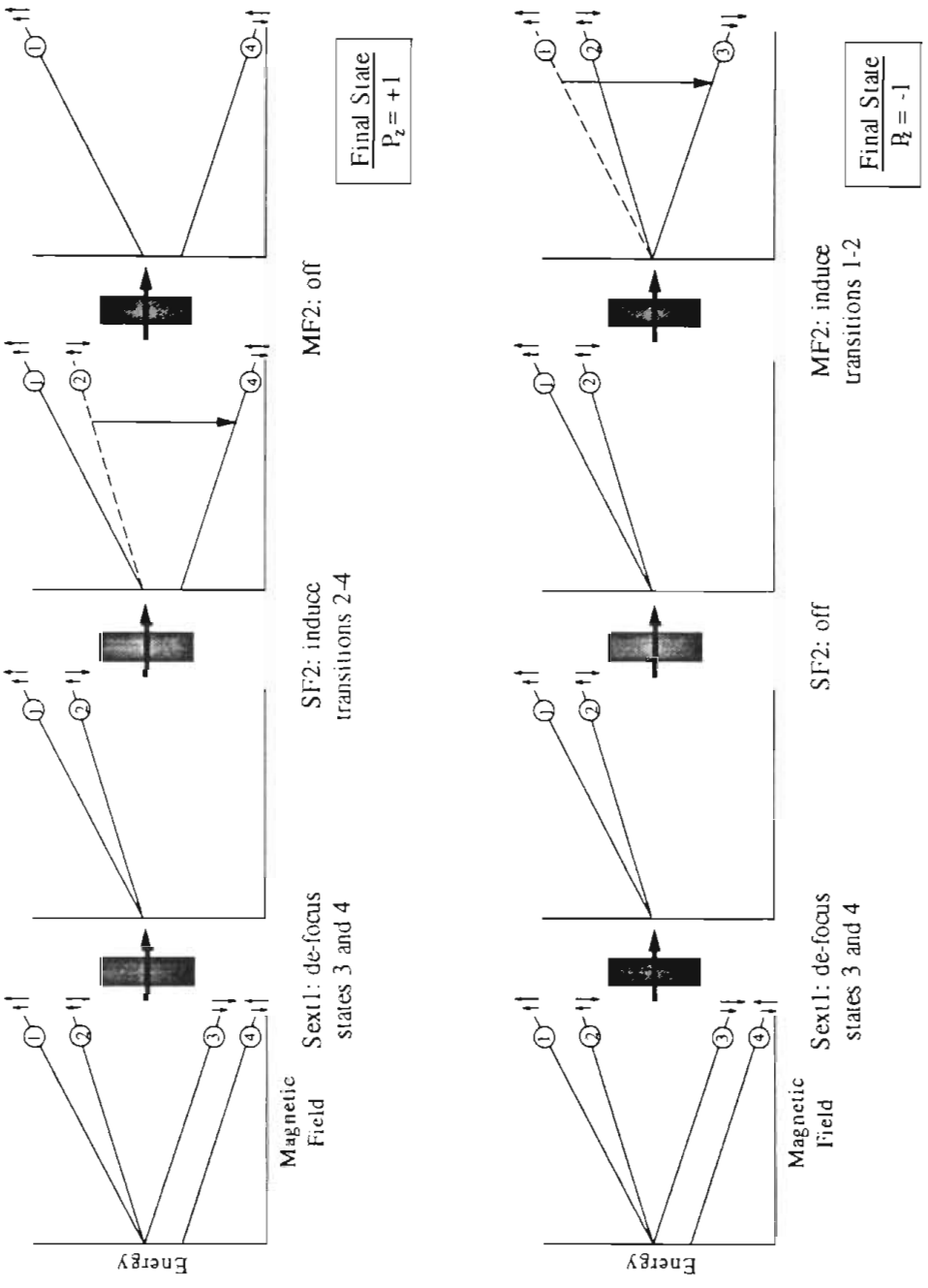

Figure 4.4: The ABPIS transition schemes used to produce "spin-up" (top) and "spin-down" (bottom) polarized proton beams. Strong field one, weak field one, and sextupole two are not used, and do not appear in the figure.

is parallel to the beam direction. Many experiments (including this one) require particles that are polarized in some other direction. A Wien filter is used to precess the spins to the desired direction. The Wien filter consists of a set of crossed electric and magnetic fields. The magnetic field can be used to precess the spins, but also tends to steer the negatively-charged beam in a direction determined by the Lorentz force. The purpose of the electric field is to steer the beam back on course. The beam receives an additional acceleration as it exits the Wien filter, so that the final energy of the particles leaving the ABPIS is 80 keV.

The matter of the spin-axis is complicated further when we realize that its orientation is not constant as the beam is steered throughout the lab by several bending magnets. Suppose a particle with non-zero spin I is deflected through an angle θ as it passes through a magnetic field. If that particle is part of a polarized beam whose spin-axis is oriented at angle β with respect to the original direction of the beam, then the spin-axis will precess about the field by an angle α given by

$$\begin{aligned} \alpha &= \frac{\mu m}{I\hbar q}\theta \\ &= g\theta \end{aligned} \tag{4.3}$$

where μ is magnetic moment of the particle, m is its mass and q its electric charge. For the special case of $g = 1$, the precession angle equals the bending angle, and so β remains constant.[2]

In the case of the deuteron, $g_d = 0.857$, while for the proton $g_p = 2.79$. Note that the precession is independent of the particle's velocity, so that the energy of the beam does not factor into the calculation of the Wien filter setting. After bending, the angle between the spin-axis and the new beam direction $\vec{k}'$ is β',

$$\beta' = \beta + \theta(1 - g). \tag{4.4}$$

Figure 4.5 indicates the orientation of the proton and deuteron spin-axes as the beams are transported to the polarized target area.

[2]If the spin-axis is parallel (or antiparallel) to $\vec{B}$, there will be no precession, so β is a constant here as well.

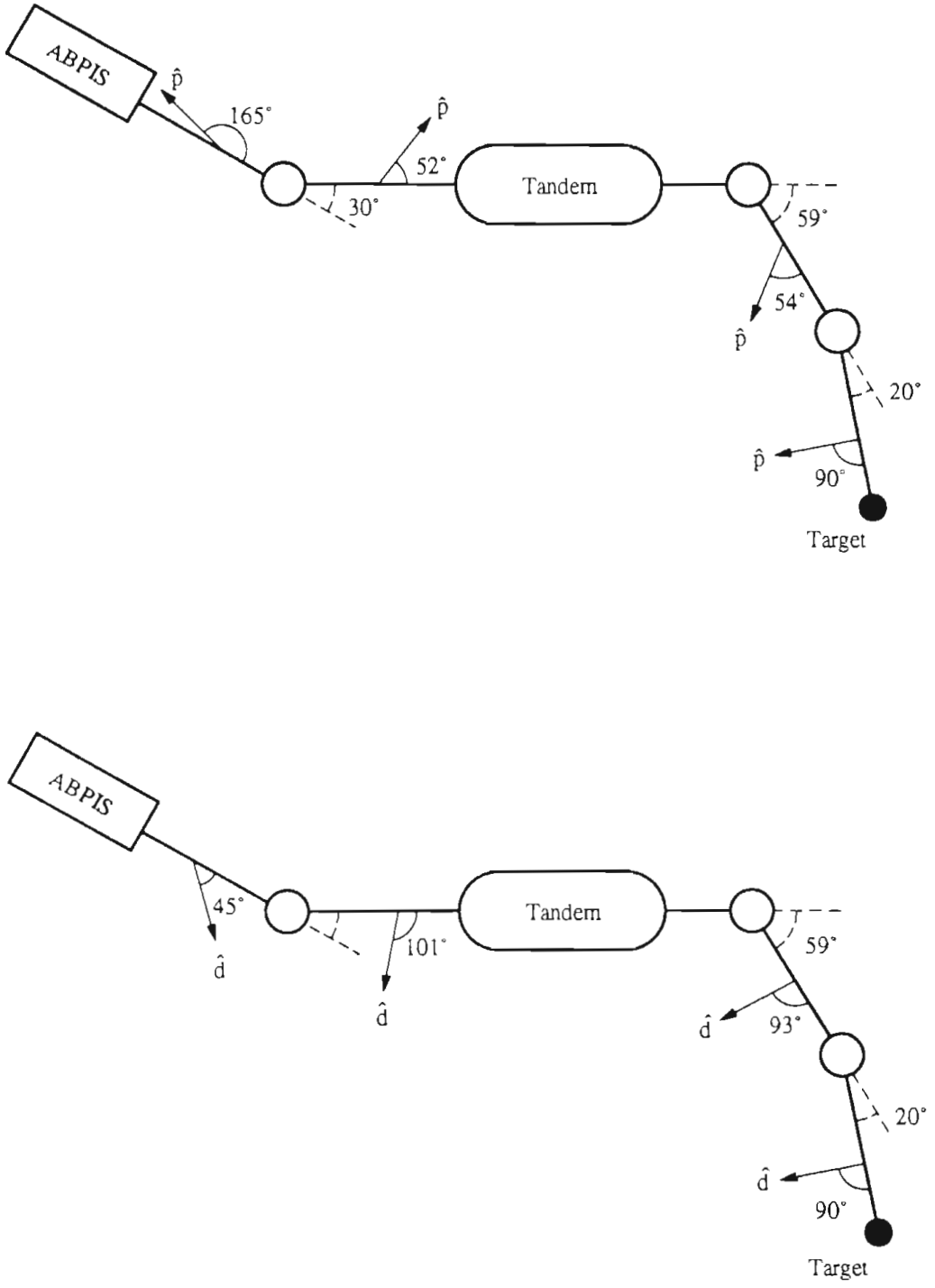

Figure 4.5: Precession of the proton spin-axis ($\hat{p}$, top) and the deuteron spin-axis ($\hat{d}$, bottom) during beam transport.)

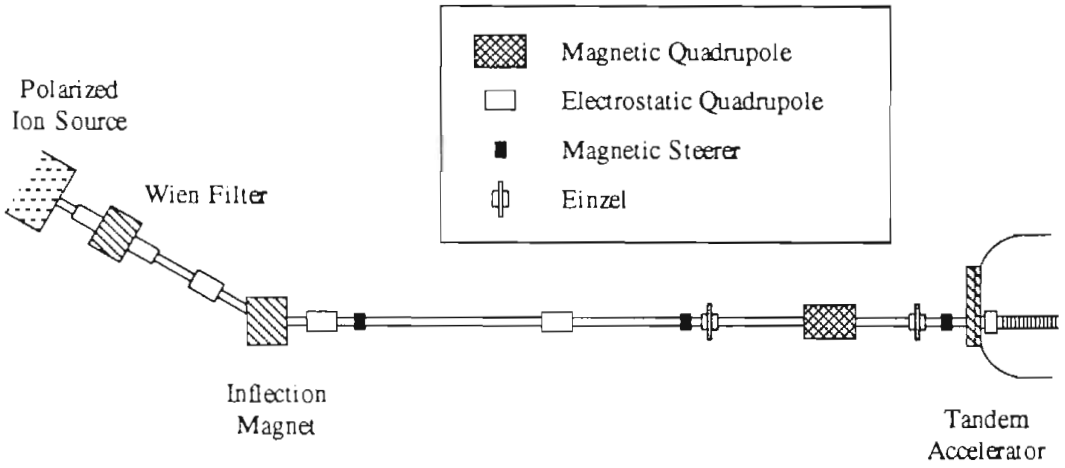

Figure 4.6: Low energy beam transport

4.1.2 Charged-Particle Beam Transport

Transport of the charged-particle beam from the polarized source to the polarized target is shown in Figs. 4.6 and 4.7. After the beam exits the ABPIS, it is bent 30° by an analyzing magnet before being ejected into a tandem Van de Graaff.[3] A carbon stripping foil, located at the center of the tandem's high-voltage terminal, removes the two electrons from the D^- (or H^-) particles in the beam, and so positively-charged deuterons (or protons) exit the high-energy end of the tandem.

Next, the beam is bent 59° by a second analyzing magnet (the "20–70" magnet). Horizontal slits are located after this magnet and measure a portion of the beam current. The signal from these slits is fed back to the tandem control circuit in order to maintain a constant beam energy.

A final bend of 19.82° is performed before the beam impacts the deuterium-gas cell or tritiated-titanium foil, at which point polarized neutrons are produced (Section 4.2.1). In addition to the 20–70 slits, there are three other sets of slits used for steering the charged-particle beam (Fig. 4.7). Each set consists of four slits—two horizontal and two vertical. The slits are used in conjunction with steering magnets located approximately two meters "upstream". A slit/magnet combination constitutes a feedback steering loop. The current measured by each slit determines how much steering is necessary to keep the beam centered at the slits.

[3]Model FN, High Voltage, Inc.

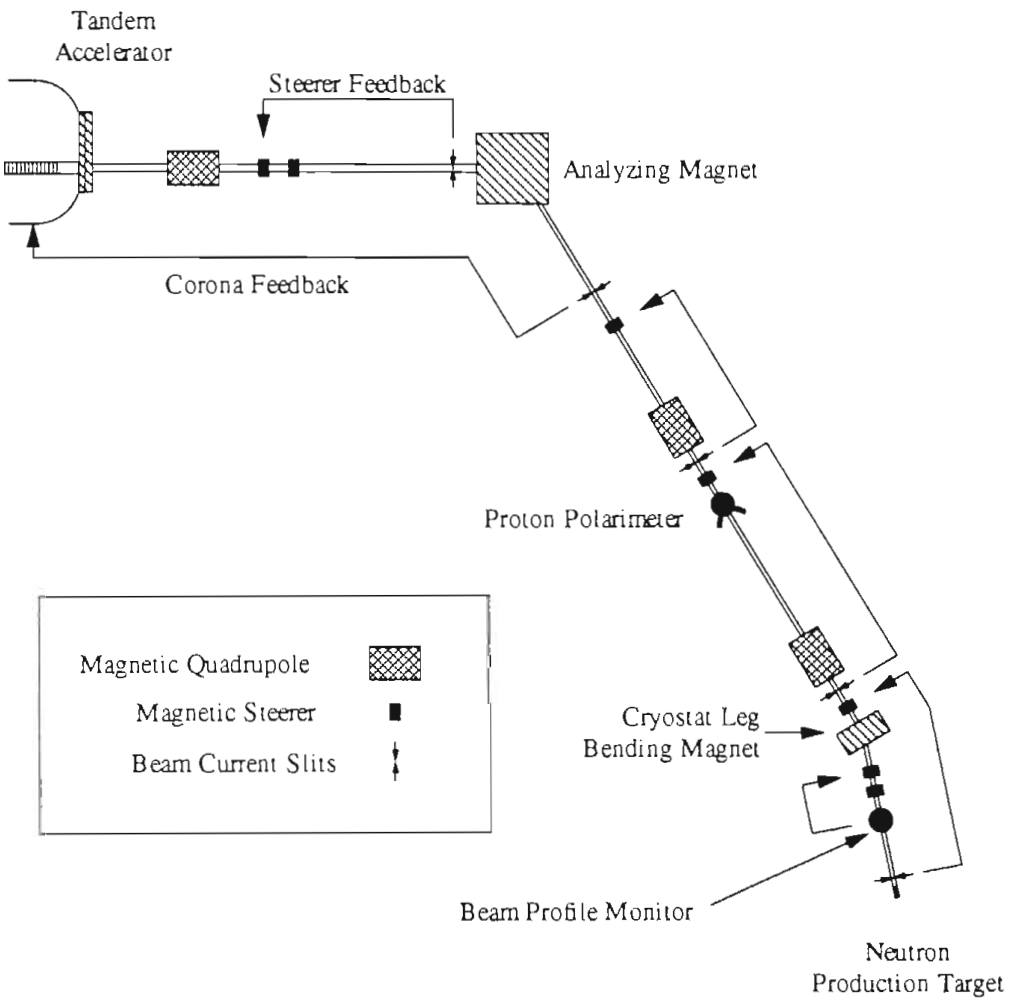

Figure 4.7: High energy beam transport

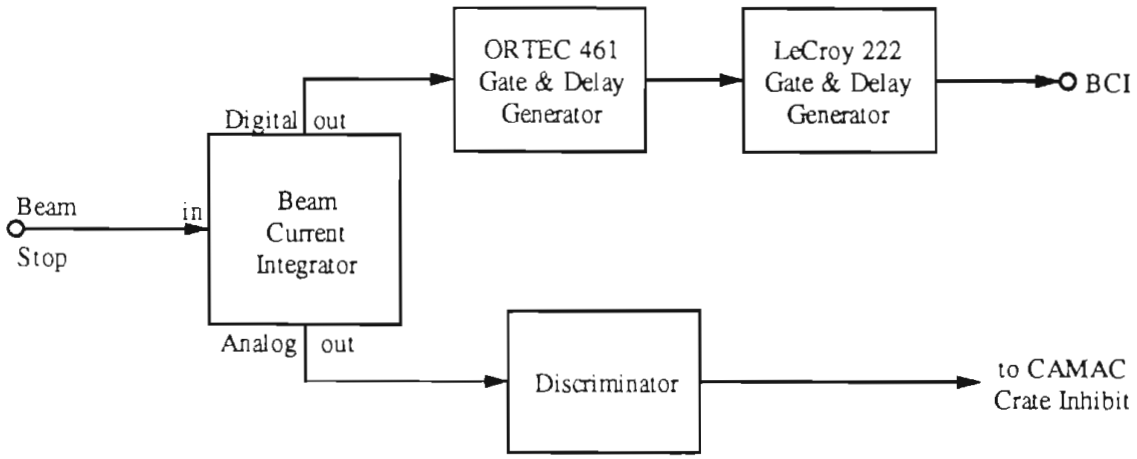

Figure 4.8: Beam current integration electronics

An beam-profile monitor (a rotating, helically-shaped wire) allows the shape of the beam to be displayed on an oscilloscope. The output of the beam-profile monitor is also read into the data-acquisition computer to calculate centroid of the beam. Based upon the position of the centroid, a signal is sent to a steering magnet in order to keep the centroid located at the center of the beam pipe. Additional details on the feedback-steering can be found in Gould *et al.* [Gou84].

Since the fringing field of the 7 Tesla polarizing magnet is perpendicular to the beam, it causes considerable deflection of the charged particles during the last meter of beam transport. To minimize this deflection, the end of the beamline is made of a 1.2 m long tube of iron, with high permeability foil wrapped inside the iron.

The total current striking the end of the beam-line is measured using a Brookhaven Nuclear Instruments Model 1000 current integrator. The beam current may be used to normalize the observed neutron-transmission asymmetries to the incident neutron flux (see Sections 4.2.1 and 4.3). The electronics for reading the beam current into the data acquisition computer are shown in Fig. 4.8. The upper and lower levels of the discriminator are used to set a "window" around the beam current. The data acquisition process is automatically halted whenever the current falls outside this window.

The charged-particle polarimeter indicated in Fig. 4.7 is the subject of the next section.

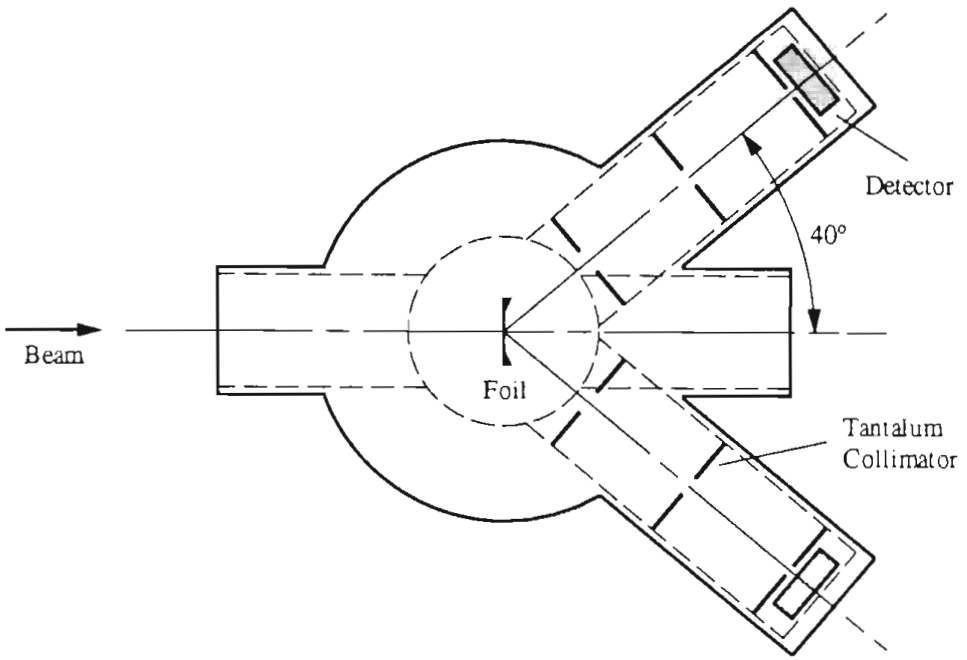

Figure 4.9: The charged-particle beam polarimeter. Same as Fig. 3.8 in [Wil93a].

4.1.3 Charged-Particle Polarimeter

The polarization of the charged-particle beam is determined by measuring left-right[4] scattering asymmetries from a carbon-foil polarimeter located between the 20-70 analyzing magnet and final bending magnet (Fig. 4.7). Once the polarization of the charged-particle beam has been determined, it is possible to calculate the polarization of the neutron beam using known values of the zero-degree polarization-transfer coefficients $K_y^{y'}(0°)$ (see Section 4.2.1). The polarimeter, as shown in Fig. 4.9, consists of a thin carbon foil mounted in the center of a scattering chamber with two silicon charged-particle detectors located at lab angles $\pm 40°$ (see [Wil93a] for additional details). The data acquisition electronics for the polarimeter are pictured in Fig. 4.10.

When determining the polarization of a proton beam, a left-right asymmetry in

[4]Due to the design of the spin-spin cryostat, it is necessary to prepare the beam with spin-axis in the horizontal plane. Therefore the scattering in the polarimeter actually occurs in the vertical plane. We will continue to call this *left-right* scattering since *up-down* is too easily confused with spin-*up* and spin-*down*.

E_p	A_y	ΔA_y
4.66	−0.496	0.022
5.04	−0.724	0.009
5.41	−0.535	0.024
5.78	−0.775	0.015
5.89	−0.812	0.022
6.18	−0.851	0.009
6.77	−0.520	0.009

E_p	A_y	ΔA_y
7.21	−0.278	0.015
7.55	−0.339	0.016
7.99	−0.131	0.017
8.66	−0.015	0.014
8.90	0.125	0.041
9.15	−0.010	0.015
9.60	−0.348	0.054

Table 4.1: Analyzing powers for the $^{12}C(p,p_0)^{12}C$ reaction at $\theta_{lab} = 40°$. Table taken from [Wil93a].

the elastic scattering of protons from ^{12}C is measured

$$\begin{aligned} \varepsilon_p^{\pm} &= \frac{N_L^{\pm} - N_R^{\pm}}{N_L^{\pm} + N_R^{\pm}} \\ &= A_y P_p \sin\beta. \end{aligned} \tag{4.5}$$

Here $N_L^{\pm}$ ($N_R^{\pm}$) are the number of elastically scattered protons detected in the left (right) silicon detector, and the $\pm$ superscript indicates the spin state of the polarized ion source. The proton polarization is P_p, while A_y is the analyzing power for the $^{12}C(p,p_0)^{12}C$ reaction at 40°, and β is the azimuthal angle between the spin-axis and incident beam direction. The analyzing powers are obtained by fitting published values of A_y as a function of energy ([Mos65, Ter68]). Values for several energies are given in Table 4.1.

The polarizations for both the up- and down-spin states are thus determined, and an average value is calculated. A highly precise (better than 1%) measurement of ε_p requires approximately 15 minutes, and is performed every 2–4 hours. We find that the beam polarization remains very constant ($\Delta P/P \leq 1\%$) over the course of our neutron scattering experiments, which typically require 12–24 hours. The greatest source of error in the determination of P_p results from the accuracy of the A_y values (see Table 4.1).

The situation for polarized deuteron beams is slightly different. Here, an asymmetry for the $^{12}C(d,p)^{13}C$ reaction is measured. This asymmetry depends not only upon the vector polarization of the deuteron beam, but upon its tensor polarization

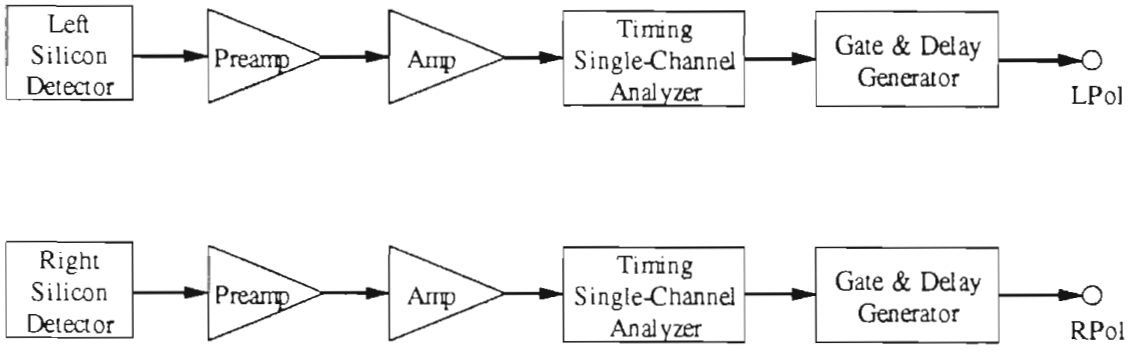

Figure 4.10: Electronics for the charged-particle beam polarimeter

as well. Ohlsen writes (Eq. (4.23) in Ref. [Ohl72])

$$\begin{aligned} \varepsilon_d &= \frac{N_L^{\pm} - N_R^{\pm}}{N_L^{\pm} + N_R^{\pm}} \\ &= \frac{\frac{3}{2} A_y P_d \sin\beta}{1 + \frac{1}{2} P_{dd} (A_{yy} \sin^2\beta + A_{zz} \cos^2\beta)}. \end{aligned} \tag{4.6}$$

Here, P_d and P_{dd} are the vector and tensor polarizations of the deuteron beam as defined at the end of Section 2.1. The angle between the deuteron spin-axis and the beam direction at the polarimeter is β, and A_y, A_{yy} and A_{zz} are vector- and tensor-analyzing powers for the $^{12}\mathrm{C}(d,p)^{13}\mathrm{C}$ reaction. The subscripts correspond to a coordinate system with z axis parallel to the incident beam momentum and y axis parallel to the deuteron's spin-axis (in the limit $\beta = 0$).

Unfortunately, we have one equation but two unknowns (P_d and P_{dd}), so it is not possible to uniquely extract both the tensor and vector components of the beam's polarization. Also, the tensor analyzing powers for the $^{12}\mathrm{C}(d,p)^{13}\mathrm{C}$ reaction are not accurately known below 10 MeV. However, a calibration of the polarimeter asymmetry ε_d versus neutron polarization has been performed [Wil] prior to this experiment. The neutron polarization was determined by the elastic scattering of polarized neutrons from ^{4}He [Tor74, Wil93a]. This calibration allows us to write the neutron polarization in terms of ε_d via an "effective" analyzing power A_{eff}:

$$\varepsilon_d = \chi A_{eff} P_n. \tag{4.7}$$

The correction factor χ must be included in Eq. (4.7) because the calibration was performed using a deuteron beam whose tensor polarization P_{dd} was very close to

zero, whereas the beam used in this experiment had $P_{dd} \sim +1$. For the sake of brevity, we leave a more detailed discussion of the calibration (and the correction factor χ) to Appendix A.

4.2 Neutron Beam

Polarized neutrons are produced as secondary beams utilizing the ^{2}H$(d,n)^3$He and ^{3}H$(p,n)^3$He reactions. Both reactions have high polarization-transfer coefficients at 0°, and have been used extensively during the last three decades as sources of polarized neutrons in the 1–20 MeV energy range. The production of polarized neutrons is reviewed by Walter [Wal71].

We begin by discussing the ^{3}H$(p,n)^3$He and ^{2}H$(d,n)^3$He reactions (Section 4.2.1), followed by the collimation and detection of the neutrons (Section 4.2.2), and finally, the data acquisition electronics (Section 4.3).

4.2.1 Neutron Beam Production

The 0° differential cross sections for the ^{3}H$(p,n)^3$He and ^{2}H$(d,n)^3$He reactions are shown in Fig. 4.11 [Lis73]. The ^{3}H$(p,n)^3$He reaction is chosen as the source of low-energy (<5 MeV) neutrons because it has a negative Q-value of -0.764 MeV. In contrast, the ^{2}H$(d,n)^3$He reaction has a positive Q-value, 3.269 MeV, making the production of neutrons below approximately 5 MeV extremely difficult. Both the ^{3}H$(p,n)^3$He and ^{2}H$(d,n)^3$He reactions may be used as sources of monoenergetic neutrons up to their three-body break-up thresholds of 8.35 and 4.45 MeV, respectively. The latter threshold was exceeded during the course of this experiment. However, the neutrons produced by the break-up reaction are ejected with at least 5.5 MeV less energy than the main group of neutrons and so the two groups can be easily discriminated (see Section 4.2.2).

For reasons of radiation safety, the tritium is adsorbed into a thin layer of titanium that has been evaporated onto a 1.9 mm diameter, 0.51 mm thick copper disk[5] (Fig. 4.12). As an additional precaution, a 1 bar ^{4}He gas cell separates the tritiated disk from the beam-line. The gas cell is sealed with a 2.54 μm Havar window. The

[5]Safety Light Corp., Bloomsburg, PA.

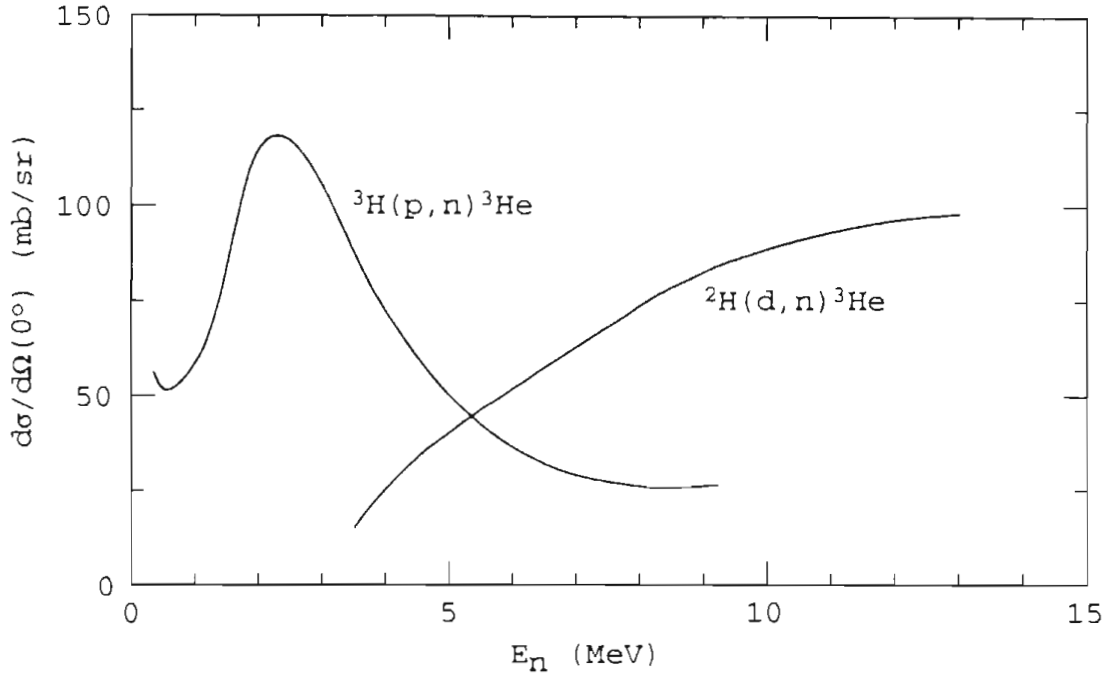

Figure 4.11: The 0° differential cross sections for the $^3\mathrm{H}(p,n)^3\mathrm{He}$ and $^2\mathrm{H}(d,n)^3\mathrm{He}$ reactions.

energy loss of the protons as they pass through the various components of the tritium target cell has been calculated using the FORTRAN code BABEL [Bow82]. The results, given in Table 4.2, are used to determine the average energy of the neutrons as well as their energy spread. The energy spread is mostly due to the finite thickness of the TiT_2 layer. Additionally, a spread equal to 10% of the proton energy loss is included. Results are compared to experimentally measured values (based on the attenuation of neutrons through oxygen and carbon [Wil93a]) in Table 4.2 as well.

The deuterium target consists of a 60 mm long, 1.9 mm diameter gas cell, filled to a deuterium gas pressure of 4 bars (Fig. 4.13). A 6.35 μm Havar window seals the gas cell from the beam-pipe, while the deuteron beam is stopped in a 0.51 mm thick tantalum disc. Energy losses for the D_2 gas cell are tabulated in 4.3. Cooling for both the tritium and deuterium targets is provided by blowing compressed air onto the back of the copper or tantalum discs.

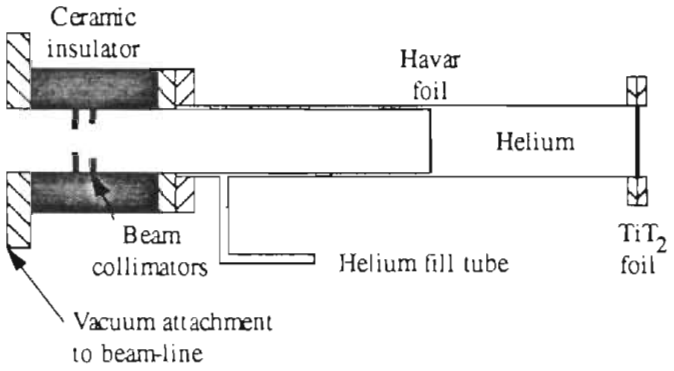

Figure 4.12: Tritiated-Titanium foil holder

Beam location	E_p	E_n	E_p	E_n
Havar Entrance	3.02	—	4.66	—
Havar Exit	2.87	—	4.56	—
^{4}He Entrance	2.87	—	4.56	—
^{4}He Exit	2.81	—	4.51	—
TiT_2 Entrance	2.81	2.02	4.51	3.74
TiT_2 Center	2.77	1.99	4.48	3.71
TiT_2 Exit	2.72	1.94	4.45	3.68
$\bar{E}_n$ (spread)	1.99 (0.083)		3.71 (0.062)	
$\bar{E}_n$ (measured)	1.94		3.65	

Table 4.2: Energy losses in the TiT_2 neutron-production target

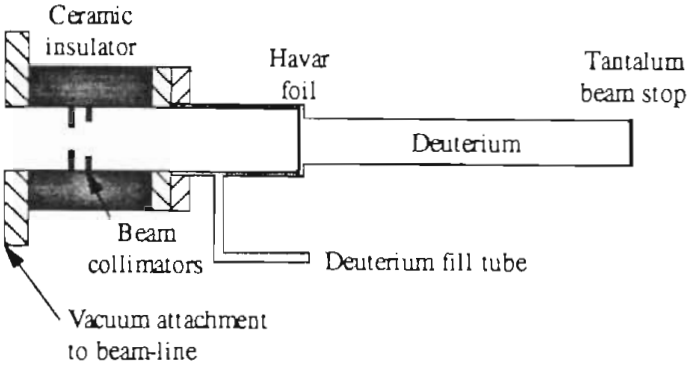

Figure 4.13: Deuterium gas cell

Beam location	E_d	E_n	E_d	E_n
Havar Entrance	3.00	—	5.00	—
Havar Exit	2.42	—	4.59	—
D_2 Entrance	2.42	5.68	4.59	7.84
D_2 Center	1.72	4.95	4.20	7.46
D_2 Exit	0.63	3.68	3.79	7.06
$\bar{E}_n$ (spread)	4.95 (1.79)		7.46 (0.781)	

Table 4.3: Energy losses in the deuterium gas cell

Although their 0° reaction cross sections are of the same magnitude, the amount of tritium contained in the TiT_2 disc is quite low (approximately 1 Ci/cm^2), and so the neutron yields from the ^{3}H$(p,n)^3$He reaction are considerably lower than the ^{2}H$(d,n)^3$He yield. Typical counting rates for this experiment were 8500 s^{-1} for the ^{2}H$(d,n)^3$He reaction and 400 s^{-1} for ^{3}H$(p,n)^3$He. These are counting rates for one neutron detector and reflect the attenuation of neutrons through the cryostat as well as the detector efficiency.

The polarization of the neutron beam is related to the charged-particle polarization by the relations [Ohl72]

$$P_n = K_y^{y'} P_p \tag{4.8}$$

when the ^{3}H$(\vec{p},\vec{n})^3$He reaction is used, and

$$P_n = \frac{\frac{3}{2}K_y^{y'}P_d}{1-\frac{1}{4}P_{dd}A_{zz}} \tag{4.9}$$

for the case of the ^{2}H$(\vec{d},\vec{n})^3$He reaction. Refer to the end of Section 2.1 for definitions of P_n, P_p, etc. A_{zz} is one of the ^{2}H$(\vec{d},\vec{n})^3$He reaction's tensor analyzing powers. The quantity $K_y^{y'}$ is a measure of how much of the incident vector polarization gets transferred to the outgoing neutron beam, and is referred to as the *polarization transfer coefficient*. In accordance with the Madison convention [Sat71], the labels y and y' refer to projections along axes that are perpendicular to the incoming and outgoing beam directions, z and z'. Since we are only concerned with polarization transfer at 0° (where $y = y'$ *etc.*) the prime on indices will henceforth be dropped.

Measurements of K_y^y for the ^{3}H$(\vec{p},\vec{n})^3$He reaction, as well as K_y^y and A_{zz} for the ^{2}H$(\vec{d},\vec{n})^3$He reaction have been made at this laboratory and elsewhere [Wil93a, Hai72, Lis75]. These values are listed in Tables 4.4, 4.5, and 4.6. For the neutron energies under consideration in this experiment, the transfer coefficients range from 0.51 to 0.65. Determination of the charged-particle polarization was discussed in Section 4.1.3. Tables 4.4, 4.5, and 4.6.

The number of neutrons produced along the incoming beam direction is called the zero-degree yield and is a measure of each reaction's zero-degree differential cross section $d\sigma/d\Omega(0°)$ (see Fig 4.11).

When the ^{3}H$(\vec{p},\vec{n})^3$He reaction is used to make neutrons, the yield is independent of the proton-beam polarization. In this case, it is sufficient to normalize the neutron yield to the number of incident protons, i.e. the beam current. The situation is different for the ^{2}H$(\vec{d},\vec{n})^3$He reaction. Here, the zero-degree yield is given by (again [Ohl72]),

$$I(0°) = I_0(1-\frac{1}{4}A_{zz}P_{dd}) \tag{4.10}$$

where I_0 is the neutron yield corresponding to a completely unpolarized beam. Ideally, P_{dd} should remain constant when we flip the deuteron spin in the ABPIS (see Figs. 4.2 and 4.3). Experimentally, we have determined that the neutron yield at 0° fluctuates by about 0.5% when the spin is flipped. Since we aim to measure spin-spin asymmetries with an instrumental precision of a few parts in 10^{-4}, it is necessary to normalize the neutron yield to some quantity besides the beam current. As will be

Deuteron Energy (MeV)	Analyzing Power A_{zz}	Uncertainty ΔA_{zz}	Deuteron Energy (MeV)	Analyzing Power A_{zz}	Uncertainty ΔA_{zz}
0.93	-0.637	0.021	7.54	-0.448	0.008
1.28	-0.597	0.012	8.06	-0.457	0.009
1.54	-0.554	0.030	8.58	-0.451	0.009
1.64	-0.535	0.011	9.10	-0.477	0.009
1.84	-0.520	0.024	9.61	-0.466	0.013
2.10	-0.499	0.019	10.12	-0.473	0.010
2.56	-0.480	0.018	10.64	-0.459	0.013
3.11	-0.475	0.010	11.15	-0.458	0.016
3.59	-0.474	0.007	11.78	-0.438	0.014
4.12	-0.475	0.011	12.17	-0.470	0.011
4.65	-0.438	0.013	12.68	-0.468	0.011
5.18	-0.456	0.011	13.19	-0.458	0.016
5.68	-0.465	0.013	13.70	-0.468	0.016
6.20	-0.434	0.010	14.21	-0.470	0.016
6.48	-0.461	0.009	14.82	-0.486	0.016
7.07	-0.454	0.008	15.22	-0.468	0.016

Table 4.4: Measured values of A_{zz} for the $^2\mathrm{H}(\vec{d},\vec{n})^3\mathrm{He}$ reaction. From Lisowski *et al.* [Lis75].

Deuteron Energy (MeV)	Neutron Energy (MeV)	Transfer Coefficient K_y^y	Uncertainty ΔK_y^y
0.91	3.92	0.425	0.054
1.40	4.56	0.510	0.033
2.01	5.24	0.577	0.017
2.47	5.70	0.598	0.020
2.96	6.27	0.610	0.035
3.59	6.85	0.638	0.008
4.11	7.37	0.632	0.012
4.65	7.90	0.655	0.009
5.08	8.32	0.650	0.010
5.64	8.86	0.663	0.008
6.12	9.33	0.634	0.008
6.59	9.78	0.631	0.008
7.10	10.27	0.648	0.009
7.50	10.65	0.644	0.010
7.97	11.10	0.642	0.005
8.50	11.60	0.626	0.010
8.97	12.07	0.627	0.011
9.54	12.59	0.652	0.010
10.06	13.14	0.636	0.008
10.57	13.57	0.639	0.010
11.09	14.06	0.624	0.008
11.56	14.50	0.628	0.011
12.11	14.98	0.630	0.013
12.59	15.47	0.616	0.010
13.14	15.99	0.615	0.007
13.67	16.44	0.605	0.012
14.12	16.92	0.605	0.012
14.64	17.41	0.615	0.012

Table 4.5: Measured values of K_y^y for the $^2\mathrm{H}(\vec{d},\vec{n})^3\mathrm{He}$ reaction. From Lisowski *et al.* [Lis75].

Proton Energy (MeV)	Neutron Energy (MeV)	Transfer Coefficient K_y^y	Uncer-tainty ΔK_y^y	Ref.
2.72	1.94	0.635	0.036	TUNL
2.96	2.12	0.632	0.048	LANL
3.96	3.12	0.661	0.033	LANL
5.00	4.15	0.719	0.052	LANL
5.52	4.66	0.681	0.031	LANL
6.03	5.16	0.724	0.036	LANL
6.08	5.21	0.789	0.046	TUNL
6.55	5.67	0.788	0.037	LANL
6.69	5.81	0.806	0.066	TUNL
7.05	6.17	0.828	0.045	LANL
7.56	6.67	0.808	0.040	LANL
8.07	7.17	0.789	0.047	LANL
8.45	7.68	0.769	0.048	LANL
8.95	8.18	0.785	0.043	LANL
9.95	9.18	0.670	0.050	LANL
10.96	10.19	0.681	0.048	LANL
11.95	11.18	0.567	0.043	LANL
12.95	12.18	0.551	0.056	LANL
13.95	13.18	0.444	0.046	LANL
14.96	14.19	0.509	0.039	LANL
15.96	15.19	0.393	0.036	LANL

Table 4.6: Measured values of K_y^y for the $^3\mathrm{H}(\vec{p},\vec{n})^3\mathrm{He}$ reaction. From Haight*et al.* [Hai72] (LANL) and Wilburn [Wil93a] (TUNL).

discussed in the following section, the normalization is provided by a small neutron detector—located between the polarized target and neutron production target.

4.2.2 Neutron Collimation and Detection

In order to maximize the counting rate, it is advisable to place the neutron production target as close as possible to the polarized ^{3}He target. The geometry is shown in Fig. 4.14. The collimation has been discussed in detail elsewhere (see [Wil93a]), and only a brief synopsis is offered here.

A copper pre-collimator is located between the cryostat and the end of the beam-line. Its purpose is to reduce the number of particles that enter the main neutron detectors without first passing through the polarized target. The bulk of the beam collimation is accomplished by polyethylene, which is also used to shield the neutron detectors from background radiation. The pre/post-collimator combination defines a 9.4 $\times$ 25.7 mm beam-spot at the center of the polarized target.

As indicated in Fig. 4.14, the back of the detector shield is open, allowing us to sight through the shield and collimator in the process of aligning the polarized target, collimator, and shielding with the beam-line. At room temperature, the polarized target hangs 3.2 mm below the axis of the beam-line. This distance corresponds to the experimentally-determined contraction that occurs inside the cryostat when it is cooled to liquid nitrogen temperature.[6] X-ray techniques have been used to verify that the target, when cooled to low temperatures, remains centered in the beam-spot [Wil93a].

The neutrons that are transmitted through the polarized target are detected by a pair of liquid scintillation detectors, optically coupled to photomultiplier tubes (PMT). These will be referred to as the "main" detectors, or as "top" and "bottom". The scintillation liquid (Bicron BC-501) contains a hydrogen-rich organic compound. As the protons recoil from n-p elastic scattering, they can partially ionize or excite atoms in the liquid. Photons are subsequently produced, either in the de-excitation or recombination process. In turn, the photons[7] produce electrons as they strike the 127 mm dia. photocathode in the PMT (Hammamatsu R1250). The number

[6] Any further contraction that occurs below this temperature is minimal.

[7] To maximize light output, the inner walls of the liquid's container (127 mm dia., 127 mm long) are coated with a highly reflective paint.

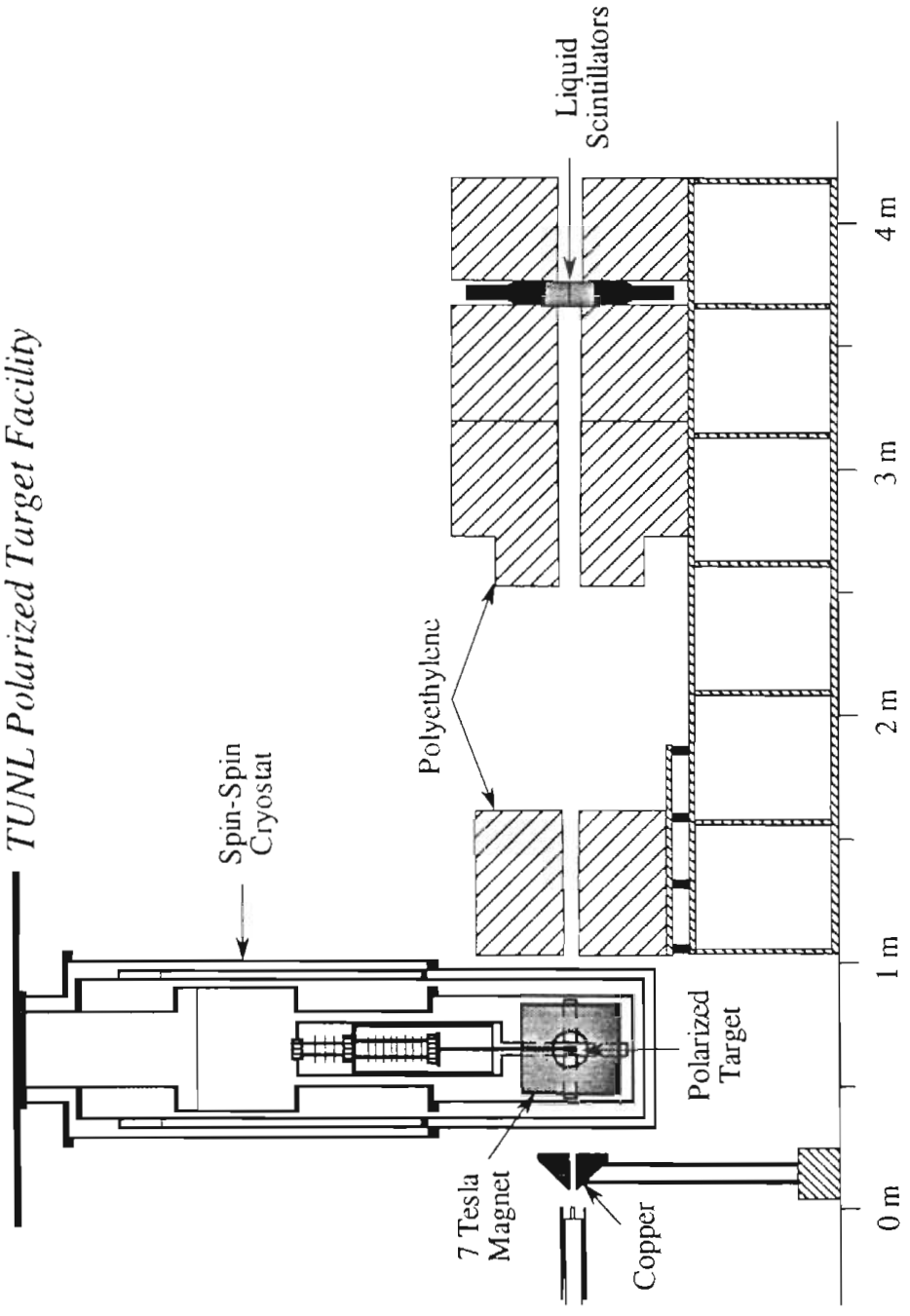

Figure 4.14: The TUNL polarized target facility

of electrons that reach the PMT's anode is increased ("multiplied") several-fold by a chain of 14 dynodes along the way (see Chapter 8 in Ref. [Leo87]). The PMTs are operated in pulsed mode. That is, each ionization event that in turn produces a sufficient number of photons is responsible for an electrical pulse emitted from the anode.

In addition to neutrons, γ-rays are produced by the charged-particle beam and also produce scintillations in the organic liquid. In this case, however, ionization is induced by Compton-scattered electrons—a process which may be distinguished from proton-recoil since the light (and therefore the PMT pulse) emitted in the latter case exhibits slower decay rates. This technique of discriminating between neutron and gamma events based upon their timing characteristics is known as *pulse-shape discrimination* or *PSD* [Leo87].

Amplification of the anode signal, as well as PSD, is performed by a commercially-manufactured PSD module (Link Analytical PSD 5020). The PSD module also functions as a single-channel analyzer, allowing the user to set energy thresholds above and below the primary (polarized) neutron group. Two output signals are recorded from the PSD module—one corresponding to the neutron event (neutron out), and a live-time signal. The neutron output is converted to a fast NIM signal (using a LeCroy 222 gate and delay generator) before it is sent to the data acquisition electronics. The live-time signal is ANDed with a 100 kHz pulser. Since the live-time signal is inhibited whenever the PSD module is busy, a dead-time correction δ for the PSD module can be determined by the ratio of pulser counts to pulser/live-time coincidences (gated counts),

$$\delta = \frac{N_{pulser}}{N_{gated}}. \tag{4.11}$$

The PSD module requires at least 260 ns to distinguish between neutron and gamma-events [Kos90] and is the greatest source of dead-time in the data acquisition process. The only dead-time correction applied to the data is the one given by Eq. (4.11).

In addition to the top and bottom detectors, a third liquid scintillator is in operation whenever the $^2\mathrm{H}(d,n)^3\mathrm{He}$ reaction is used to produce the polarized neutron beam. This "monitor" detector is necessary to normalize the neutron yield, which can fluctuate due to variations of the tensor component in the polarized deuteron beam (Section 4.1.3). The scintillator (NE-213) is contained within a small aluminum box (25.4 $\times$ 11.1 $\times$ 22.2 mm) with a single glass window. The window is optically cou-

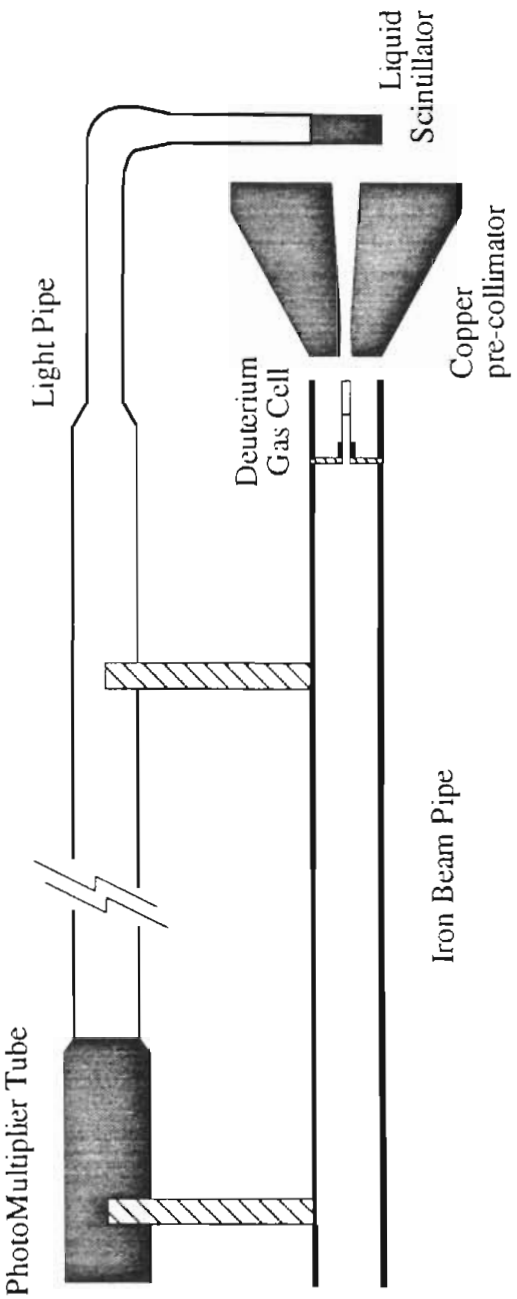

Figure 4.15: The neutron monitor detector

pled to a 51 mm dia. PMT (Hammamatsu R329-02) through a 1 m long light pipe (Fig. 4.15). The entire assembly mounts directly above the beam-line, with the scintillator hanging between the copper pre-collimator and the outside of the spin-spin cryostat. A long light pipe is necessary to ensure that the PMT is located beyond the strong magnetic field of the superconducting magnet.

Thus located, the monitor detector is sensitive to any changes in neutron flux that arise due to fluctuations in P_{dd}, but is it not sensitive to spin-dependent interactions in the polarized target. While it has PSD capability, we have found that a properly set discriminator threshold renders the detector virtually insensitive to γ-rays. This should not be too surprising, considering the 22 mm length of the detector, and the energy loss of the Compton-scattered electrons (see Section 3.5 for a discussion of Compton scattering).

The data acquisition electronics for the two main detectors as well as the monitor detector are shown in Fig. 4.16.

4.3 Data Acquisition Electronics

A measurement of the spin-spin asymmetry ε consists of counting the number of neutron events that occur in the two main detectors (previous section) as the spin of the neutron beam is reversed. Data collection and signal processing are accomplished by a system of CAMAC modules. The modules are controlled by a MBD-11 Multiple-Branch Driver [Rob81] which also serves as the interface between the modules and one of two dedicated Digital Electronics Corporation VAXstation 3200 computers. In addition, the computer is responsible for part of the feedback steering of the charged-particle beam (see Section 4.1.2). All data acquisition, sorting, and on-line analysis are performed using the software package TUNL XSYS [Gou81].

A number of techniques are employed to achieve an instrumental precision of a few parts in 10^{-5}. First, the beam is monitored in order to normalize both spin states to the same incident neutron flux. Secondly, to eliminate false asymmetries that may arise due to slow variations in detector efficiency, the neutron spin is reversed at the rate of 10 Hz. Moreover, the spins are flipped according to a special 8-step sequence that cancels any effects due to detector drifts that are either linear or quadratic in time. Precision timing is used to ensure that equal amounts of time are spent in both

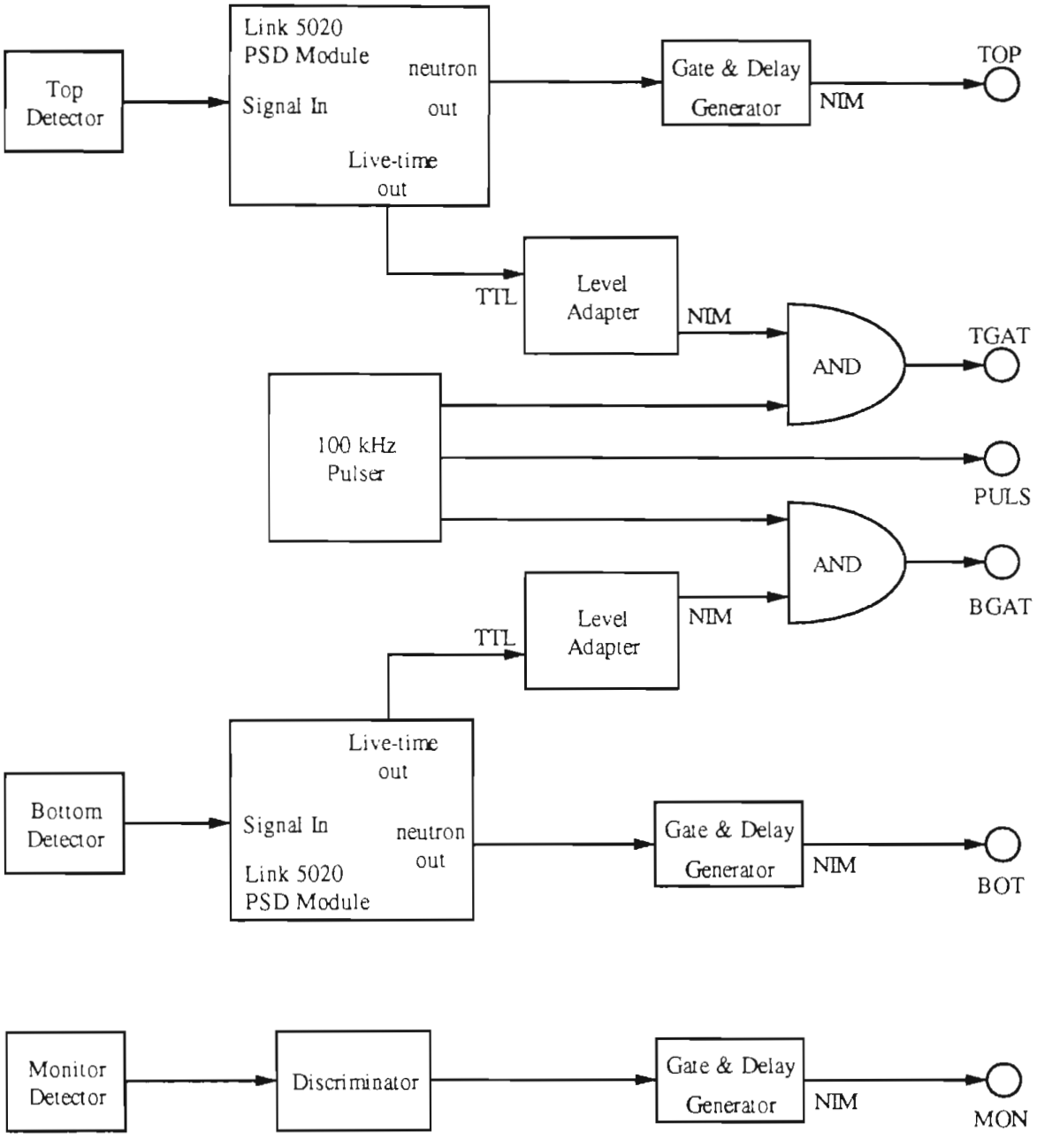

Figure 4.16: Block diagram for the top-, bottom-, and monitor-detector electronics. Signals from the PMT anodes enter on the left. All output signals—sent to the computer interface on the right—have 75 ns widths.

spin-states. Finally, the temperature of the target is monitored on-line, allowing for a highly accurate determination of its polarization.

A detailed, pedagogical discussion of the fast-spin flip technique has been given by Koster [Kos90]. Another former student of the polarized target group has described the beam-profile monitor [Wil93a] (see also Section 4.1.2).

The only substantial difference between the measurements made above 5 MeV and those made at lower energies concerns the normalization of the incident neutron flux. In either case, the data acquisition electronics are virtually identical—a beam current integrator (BCI) replaces the monitor detector that is used at the higher energies. All signals fed to the data acquisition system pass through a Phillips 706 sixteen-channel discriminator. A schematic of the data acquisition electronics is shown in Fig. 4.17.

A CAMAC-compatible NIM module, constructed by the TUNL electronics shop, is used to control the spin-state of the polarized beam. This "Spin-State Controller" (SSC) is located in the laboratory control room and connects the MBD to the polarized ion source's RF units through a system of fiber-optic cables. The SSC is designed to produce TTL-level signals in the above-mentioned 8-step sequence: $+--+-++-$. The TTL signals are used to toggle the proper RF units (chosen by the user) so that the spin of the charged-particle beam is flipped according to the same 8-step sequence. The signals are produced every 100 ms, and are controlled by a precision oscillator (the "VAX clock").

The SSC also produces duplicates of the "+" and "−" signals to be used for the spin-routing information. An analog-to-digital converter (ADC) reads the "+" signal and alerts the MBD that a spin-reversal has occurred. The ADC uses this signal to tag the incoming data according to the appropriate spin-state. If for any reason the data acquisition process is stopped, the SSC turns itself off and restarts at the same point in its 8-step sequence when the data acquisition resumes.

When the end of each 8-step sequence is reached, the SSC triggers a count-down scaler, which has been initialized by the XSYS software to a preset value of 1024. Data is thus stored in the computer buffer as a spectrum of counts versus time, each 8-step sequence compromising one channel. When the count-down scaler reaches zero, the "run" is over. Data acquisition is inhibited, and the computer writes the data to disk. Multiplying 800 ms by 1024 reveals that each run requires approximately 15 minutes. This method of acquiring data permits both the online and offline data analysis to be

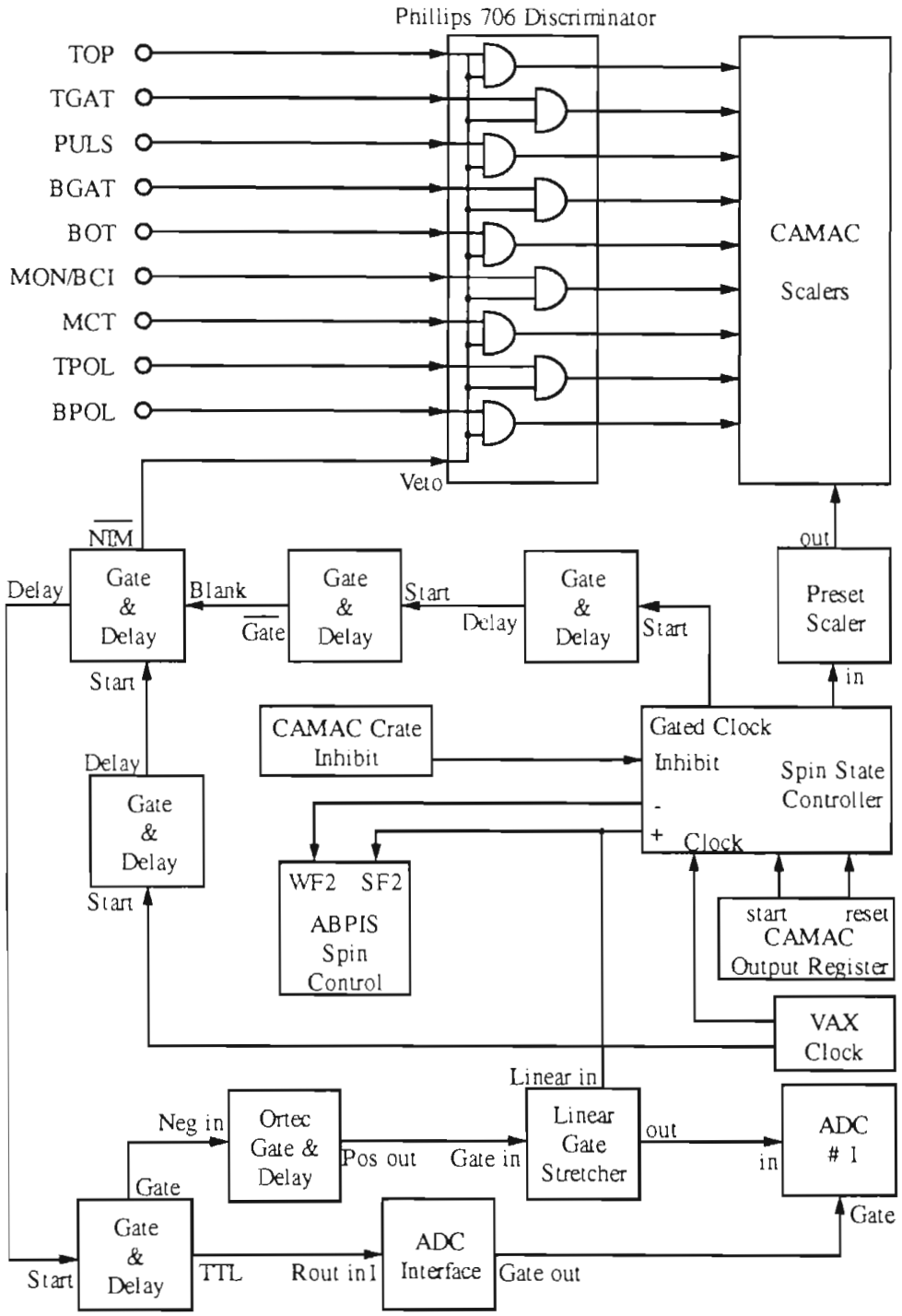

Figure 4.17: Block diagram for the data acquisition electronics. Signals from the neutron detector electronics, melting curve thermometer, *etc.* enter the Phillips 706 module from the upper-left corner.

performed in intervals of 800 ms. In fact, all data analysis, including normalization of the detector yields to beam flux, dead-time corrections, and calculation of target polarization, is performed in this channel-by-channel fashion.

All data that arrive 2 ms prior to, and 7 ms after each spin-signal, are ignored. This is the amount of time that is necessary for the polarization to stabilize after a spin-flip [Kos90]. A pair of gate and delay generators produce a veto signal that inhibits the Phillips 706 during this time. A second pair of gate and delays operate in parallel with the first, blanking its output whenever the Phillips 706 is inhibited. (The Phillips and thus the data acquisition is stopped whenever the beam current falls below a pre-set value, or whenever the computer buffer is flushed.) In this manner, the timing circuits of the first set of gate and delays run continuously and are not subject to drifts that may occur when they are switched on and off. The timing circuit for the spin-flip electronics is shown in Fig. 4.18.

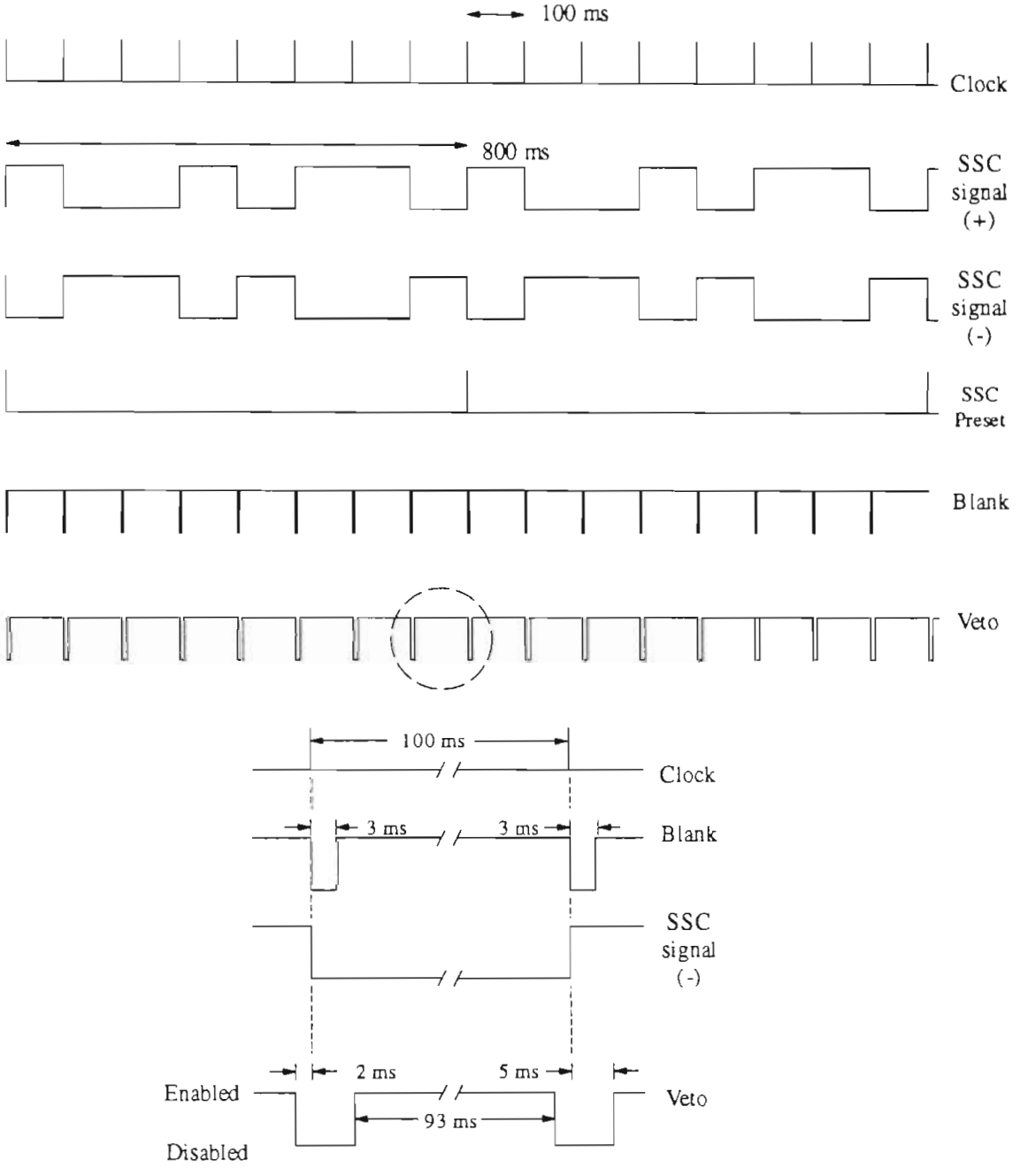

Figure 4.18: A logic diagram for data acquisition during two complete eight-step sequences. The time scale for the two indicated veto signals (circled) is expanded at the bottom to detail the 7 ms period during which data acquisition is inhibited.

Chapter 5

Experimental Procedure and Results

Spin-spin asymmetries were measured with a polarized solid ^{3}He target at neutron energies of 1.94, 3.65, 4.95 and 7.46 MeV. These measurements are designated "cold solid" in Table 5.1. This table summarizes all transmission measurements made with the ^{3}He target to date. As indicated, asymmetries were also measured at each of the four energies after the target had been unpolarized by warming it to 1 K. Designated "warm liquid", these measurements are used to determine the "false" asymmetries that arise from instrumental effects (see Section 5.5). The false asymmetries must be subtracted from the "cold solid" measurements to determine the true asymmetry that is due to the spin-spin cross section of ^{3}He.

There are materials in the BeCu that also become polarized at low temperatures (Section 3.4). Additional neutron-transmission measurements were made to determine whether these materials make any contribution to the "cold solid" asymmetries. These "background" measurements consisted of emptying the cell and measuring the transmission asymmetry with the cell cold (< 20 mK) or warm (1 K). These are designated "cold empty" and "warm empty" in Table 5.1.

Finally, measurements were made at two energies with a cell filled with polarized liquid ^{3}He. As discussed in Section 3.1.3, the polarization of the liquid phase is very small (about 3%) even at the lowest temperatures. These measurements were conducted because it is much quicker to melt the solid sample and then re-cool it below

E_n (MeV)	Target Cell	^{3}He Polarization	Asymmetry (10^{-4})
1.94	Cold Solid	0.37	-42.94 ± 1.86
	Cold Liquid	0.03	-5.12 ± 2.62
	Warm Liquid	0.00	3.15 ± 2.34
3.65	Cold Solid	0.35	-45.52 ± 2.50
	Cold Liquid	0.03	-5.90 ± 2.58
	Warm Liquid	0.00	0.66 ± 2.40
4.95	Cold Solid	0.31	-30.22 ± 1.04
	Cold Empty	0.00	-0.98 ± 0.97
7.46	Cold Solid	0.35	-23.57 ± 0.65
	Cold Empty	0.00	-2.51 ± 0.57
	Warm Empty	0.00	-3.76 ± 0.64
	Warm Liquid	0.00	-3.17 ± 0.59

Table 5.1: A summary of the twelve $\vec{n}$-$^3\vec{\text{He}}$ asymmetry measurements.

20 mK in the liquid phase.[1] Pumping the ^{3}He from the BeCu cell is time-consuming (3 hours) and requires heating the sample to 3 K. The results of these measurements are discussed in Section 5.7. In all, a total of twelve asymmetry measurements were made.

We begin with a brief synopsis of the experimental procedure. This has been discussed in more detail in the preceding chapters.

5.1 Experimental Procedure

The spin-spin cross sections are extracted from differences in neutron transmission through the polarized target when the spin of the incident neutron beam is reversed. The neutron spin is flipped according to a special eight-step sequence that is designed to eliminate the effects of short-term changes in detector efficiency (Section 4.3). The transmission of polarized neutrons through the polarized target depends on the spin-

[1] Because the ^{3}He melting curve has a negative slope below 300 mK, the solid sample warms upon melting to approximately 100 mK.

spin cross section in the following way.

The number of neutrons that pass unscattered through the target is given by

$$N = N_0 e^{-\sigma_{tot}\tau}, \tag{5.1}$$

where N_0 are the number of incident neutrons, and τ is the thickness of the target expressed in atoms per barn. If the beam and target are both polarized (P_n and P_T, respectively), the total cross section for scattering becomes

$$\sigma_{tot} = \sigma_0 + \sigma_{ss} P_n P_T \tag{5.2}$$

See Section 2.2.3 for more details and definitions. We can define an average beam polarization so that reversing the spin of the beam simply changes the sign of P_n. The neutron-transmission (or "spin-spin") asymmetry is then defined to be

$$\begin{aligned} \varepsilon &= \frac{N_+ - N_-}{N_+ + N_-} \\ &= \frac{e^{+\sigma_{ss} P_n P_T \tau} - e^{-\sigma_{ss} P_n P_T \tau}}{e^{+\sigma_{ss} P_n P_T \tau} + e^{-\sigma_{ss} P_n P_T \tau}} \\ &= -\tanh\left(\frac{1}{2}\Delta\sigma_T \; P_n P_T \tau\right), \end{aligned} \tag{5.3}$$

where $\pm$ refers to the sign of P_n. In the final step we have substituted the fact that the total cross section *difference* $\Delta\sigma_T$, is equal to twice the spin-spin cross section. The asymmetry is independent of the unpolarized cross section. However, the incident beam flux may not be the same for both spin states, and therefore must be measured.[2] In addition to measuring the incident fluxes and the spin-spin asymmetry, determination of $\Delta\sigma_T$ requires measuring P_n, P_T, and τ. Each of these will be discussed in turn.

In the present experiment, the charged-particle beam currents range from 0.7 μA to 0.2 μA and depend on both the beam energy and type of charged particle (p or d). A typical count rate for each of the two main neutron detectors is 8700 s^{-1} when using a 0.4 μA deuteron beam and 4 bar of D_2 in the gas cell. At this count rate, the spin-spin asymmetry can be determined to a statistical accuracy of $\pm 0.5 \times 10^{-4}$ in approximately 8 hours. The counting rates corresponding to the proton beam are

[2] Actually, it is sufficient to measure the ratio of the two fluxes.

considerably lower, 400 s^{-1}. In this case the measurements are halted after achieving an accuracy of $\pm 1.5 \times 10^{-4}$ (18 hours).

At each energy the neutron detector PSD and high voltage settings must be adjusted. Similar adjustments are made to the solid state detectors inside the charged-particle polarimeter. When the charged-particle beam is switched from deuterons to protons, the deuterium gas cell must be replaced by the TiT_2 foil (Section 4.2.1). The gas pressures in both neutron production targets are checked about once per day when the spin-spin cryostat is filled with LHe. The 7 Tesla magnetic field is left on for all asymmetry measurements, including the "background" measurements.

Transmission asymmetries from a polarized target are begun when the melting curve thermometer indicates a target temperature less than about 15 mK. Before and after each "cold" asymmetry measurement, γ-rays from the nuclear orientation thermometer are counted for a period of time sufficient for a $\sim 2\%$ determination of the temperature. In most cases the corresponding "warm" counts for the NO thermometer are obtained immediately afterward, when the target is warmed above 100 mK. When beam is on target (cold target), the melting curve thermometer is used to monitor the temperature. In all but one case, these MCT values are used to calculate an average target polarization during the asymmetry measurement.

5.2 Data Analysis

The data acquisition system has been discussed previously (Section 4.3). Some data analysis is performed on-line, during the experiment, and the results written to the computer video screen in order to monitor the experiment. An example of the video screen "boxdump" is shown in Table 5.2. The final analysis, from which the values of $\Delta\sigma_T$ are extracted, is done off-line.

Section 4.3 discussed the precautions that are taken to ensure that equal amounts of time are spent acquiring neutron counts in both the *up* and *down* spin-states. However, there are times during which the data acquisition process is temporarily halted in the middle of the eight-step spin sequence (e.g. the beam current falls outside the discriminator window). All data taken during this sequence should be rejected. Such events can be detected in the off-line analysis by examining the spectra produced by the 100 kHz pulser. The pulser is stable to within a few parts in 10^4 and is used

Run # 1057		Energy 7.500000		Sum_Ay -23.8700		Dif_Ay 81.76000	
BCI_up	Puls_up	Mon_up	Top_up	Bot_up	Tpol_up	Bpol_up	P_Ay_up
24950	38300584	23439494	3851774	3789058	7585	9559	-0.11514
BCI_dn	Puls_dn	Mon_dn	Top_dn	Bot_dn	Tpol_dn	Bpol_dn	P_Ay_dn
24927	38300452	23194656	3767969	3829404	9605	7673	0.111818
	Tdtc_up	Bdtc_up	Myld_up	Tyld_up	Byld_up	Mon_Ay	Register
	1.004861	1.003199	2.34E+07	0.165127	0.162170	52.50187	1024
Volt	Tdtc_dn	Bdtc_dn	Myld_dn	Tyld_dn	Byld_dn	Sum_Ay	Dif_Ay
0.449219	1.004781	1.003234	2.32E+07	0.163227	0.165633	-23.8742	87.76006
				——	Avg Ay	+/- Stat	Std Dev
13:40:35				SUM	-24.30	+/- 1.97	(0.74)
				DIF	83.38	+/- 1.97	(1.66)
Run Started		8-Feb-1994 13:26:24		MON	-50.23	+/- 1.04	(2.31)
Run Halted		8-Feb-1994 13:40:09		Asymmetries calculated OK			

Table 5.2: An example of the on-line analysis that is written to the data acquisition computer screen. This particular example corresponds to data obtained from a polarized, solid target at $E_n = 7.46$ MeV.

to determine the deadtime corrections for the neutron detectors (Section 4.2.2). If the data acquisition process is halted, one of the two pulser spectra (one for spin-up, one for spin-down) will exhibit a discontinuity—a dip or a spike (Fig. 5.1). During the off-line analysis, channels in which the number of pulser counts is more than four standard deviations away from the mean value are tagged, and all data in these channels are rejected. Typically this represents less than 1% of the data.

The neutron transmission asymmetries are then determined from the remaining data. First, the number of raw neutron counts observed during each step of the eight-step sequence is normalized to the incident neutron flux and is multiplied by the deadtime correction δ (Eq. (4.11)),

$$\tilde{N} = \frac{N}{I}\delta, \tag{5.4}$$

where the normalization factor I is either the integrated proton current or the neutron yield into the monitor detector (Section 4.2.2).

The asymmetry for one detector is then

$$\varepsilon = \frac{\tilde{N}_+ - \tilde{N}_-}{\tilde{N}_+ + \tilde{N}_-} \tag{5.5}$$

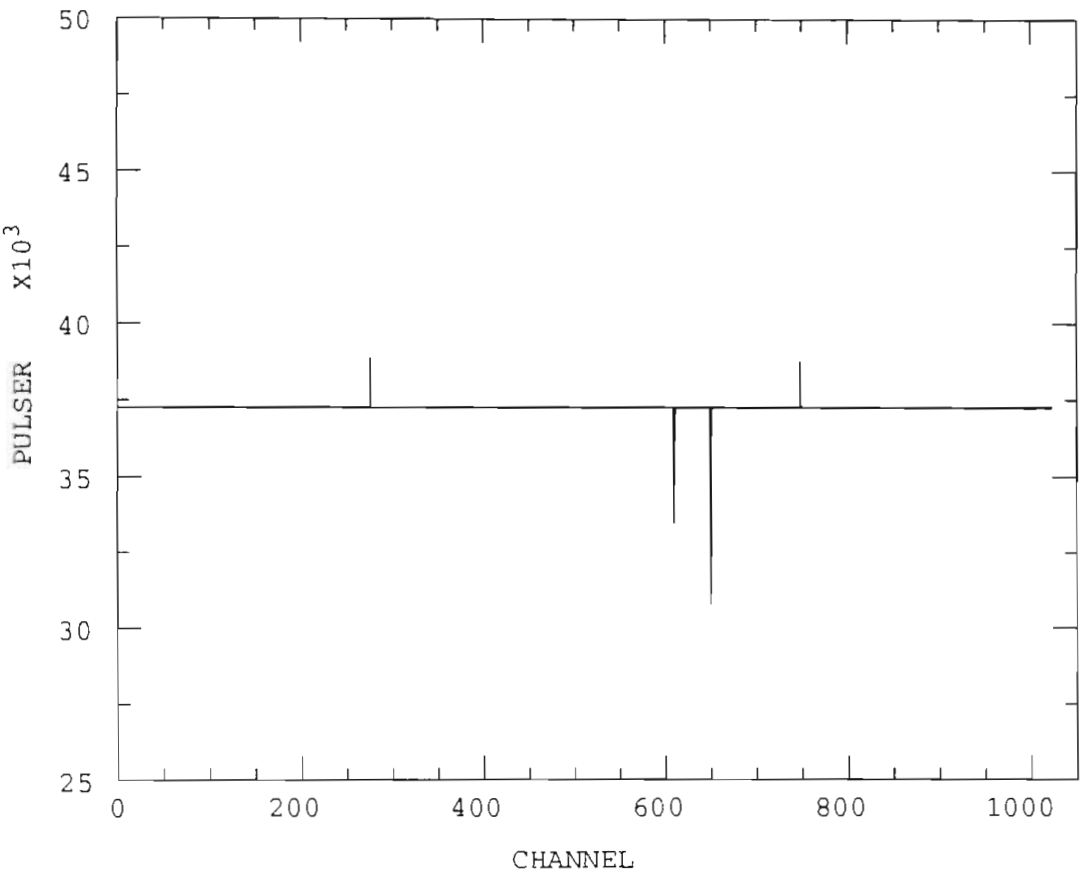

Figure 5.1: An example of the spectra produced by the 100 kHz dead-time pulser. Each channel consists of 1 eight-step spin sequence. All data corresponding to channels 260, 600, 632, and 751 are rejected in the off-line analysis.

and its error

$$\Delta\varepsilon = \left[\left(\frac{\partial\varepsilon}{\partial N_+}\Delta N_+\right)^2 + \left(\frac{\partial\varepsilon}{\partial N_-}\Delta N_-\right)^2 + \left(\frac{\partial\varepsilon}{\partial I_+}\Delta I_+\right)^2 + \left(\frac{\partial\varepsilon}{\partial I_-}\Delta I_-\right)^2\right]^{1/2}. \tag{5.6}$$

The $\pm$ subscripts label the spin-state of the polarized ion source, $+$ indicating that the beam spin is parallel to the target spin, and $-$ antiparallel. Since the number of counts in the neutron detector follows a Poisson distribution, we have

$$\Delta N_\pm = \sqrt{N_\pm}. \tag{5.7}$$

The uncertainty in the normalization factor $I_\pm$ depends on whether the BCI or the monitor detector is used. In the latter case

$$\Delta I_\pm = \sqrt{M_\pm}, \tag{5.8}$$

$M_\pm$ being the number of neutron counts in the monitor detector. In this case, the asymmetry error for one detector is

$$\Delta\varepsilon = \frac{2\tilde{N}_+\tilde{N}_-}{(\tilde{N}_+ + \tilde{N}_-)^2}\left[\frac{1}{N_+} + \frac{1}{N_-} + \frac{1}{M_+} + \frac{1}{M_-}\right]^{1/2}. \tag{5.9}$$

When the BCI is used to normalize the neutron counts, the uncertainty in $I_\pm$ does not follow from a Poisson distribution. The error arises during the digitization of the BCI signal. Each time the spin of the charged-particle beam is flipped, there is an uncertainty of $1/2$ count associated with I. There are three such spin flips in each eight-step sequence $(+--+-++-)$, and adding the errors in quadrature gives

$$\Delta I_\pm = \frac{\sqrt{3}}{2}. \tag{5.10}$$

Substitution into Eq. (5.6) yields the error corresponding to the BCI-normalized asymmetry measured by one detector,

$$\Delta\varepsilon = \frac{2\tilde{N}_+\tilde{N}_-}{(\tilde{N}_+ + \tilde{N}_-)^2}\left[\frac{1}{N_+} + \frac{1}{N_-} + \frac{3}{4}\left(\frac{1}{I_+^2} + \frac{1}{I_-^2}\right)\right]^{1/2}. \tag{5.11}$$

The asymmetry that is used to determine $\Delta\sigma_T$ is the average value of ε measured by the top and bottom neutron detectors,

$$\varepsilon_{sum} = \frac{\varepsilon_t + \varepsilon_b}{2}. \tag{5.12}$$

E_n	Target	n	$\bar{\varepsilon}_{sum}$	$\pm$	$\Delta\bar{\varepsilon}_{sum}$	$(\sigma_{\bar{\varepsilon}_{sum}})$	$\bar{\varepsilon}_{diff}$	$\pm$	$\Delta\bar{\varepsilon}_{diff}$	$(\sigma_{\bar{\varepsilon}_{diff}})$
1.94	Cold Solid	70484	-42.94	$\pm$	1.72	(1.86)	68.86	$\pm$	1.63	(1.64)
	Cold Liquid	37394	-5.12	$\pm$	1.90	(2.62)	71.78	$\pm$	1.51	(1.52)
	Warm Liquid	29658	3.15	$\pm$	2.15	(2.34)	70.84	$\pm$	1.71	(1.71)
3.65	Cold Solid	55633	-45.52	$\pm$	2.16	(2.49)	-37.14	$\pm$	1.89	(1.90)
	Cold Liquid	58036	-2.69	$\pm$	1.33	(1.52)	-30.35	$\pm$	2.04	(2.03)
	Warm Liquid	25321	0.66	$\pm$	2.09	(2.40)	-30.80	$\pm$	1.87	(1.87)
4.95	Cold Solid	24049	-30.22	$\pm$	1.05	(1.04)	53.88	$\pm$	0.93	(0.93)
	Cold Empty	12384	-0.98	$\pm$	0.98	(0.97)	55.39	$\pm$	0.86	(0.86)
7.46	Cold Solid	25433	-23.57	$\pm$	0.64	(0.65)	84.83	$\pm$	0.56	(0.56)
	Cold Empty	33712	-2.51	$\pm$	0.57	(0.57)	87.37	$\pm$	0.49	(0.57)
	Warm Empty	21476	-3.76	$\pm$	0.64	(0.64)	86.69	$\pm$	0.55	(0.55)
	Warm Liquid	33569	-3.17	$\pm$	0.59	(0.59)	85.73	$\pm$	0.51	(0.51)
	CE + WE + WL	88757	-3.10	$\pm$	0.35	(0.35)	86.61	$\pm$	0.30	(0.30)

Table 5.3: Measured values of the neutron-transmission asymmetries. n is the total number of eight-step sequences used in each analysis. All units are 10^{-4}. The final row, (CE + WE + WL), is the result of treating the Cold Empty, Warm Empty, and Warm Liquid asymmetries as equivalent measurements.

The total error for both detectors is then

$$\Delta\varepsilon_{sum} = \frac{1}{2}\left[(\Delta\varepsilon_t)^2 + (\Delta\varepsilon_b)^2 + \frac{6\tilde{N}_+^t\tilde{N}_-^t\tilde{N}_+^b\tilde{N}_-^b}{(\tilde{N}_+^t+\tilde{N}_-^t)^2(\tilde{N}_+^b+\tilde{N}_-^b)^2}\left(\frac{1}{I_+^2}+\frac{1}{I_-^2}\right)\right]^{1/2} \tag{5.13}$$

when the asymmetries are BCI-normalized, and

$$\Delta\varepsilon_{sum} = \frac{1}{2}\left[(\Delta\varepsilon_t)^2 + (\Delta\varepsilon_b)^2 + \frac{8\tilde{N}_+^t\tilde{N}_-^t\tilde{N}_+^b\tilde{N}_-^b}{(\tilde{N}_+^t+\tilde{N}_-^t)^2(\tilde{N}_+^b+\tilde{N}_-^b)^2}\left(\frac{1}{M_+}+\frac{1}{M_-}\right)\right]^{1/2} \tag{5.14}$$

when they are normalized by the monitor detector. The superscripts t and b in these equations refer to the top and bottom detectors, respectively. The final terms in Eqs. (5.13) and (5.14) reflect the correlation that results from normalizing both the top and bottom detector to the same value of I_+ and I_- (or M_+ and M_-).

In the off-line analysis, the asymmetries (and their uncertainties) are calculated on a channel-by-channel basis. Each channel refers to one complete eight-step sequence. For each asymmetry measurement there are n eight-step sequences. The results are weighted by the uncertainties, and the average asymmetry $\bar{\varepsilon}$ and its standard devia-

tion $\sigma_{\bar{\varepsilon}}$ are calculated. Results are shown in Table 5.3.

$$\Delta\bar{\varepsilon} = \left[\sum_{i=1}^{n} \frac{1}{\Delta\varepsilon_i^2}\right]^{-1/2} \tag{5.15}$$

$$\bar{\varepsilon} = \left[\sum_{i=1}^{n} \frac{\varepsilon_i}{\Delta\varepsilon_i^2}\right] \Delta\bar{\varepsilon}^2 \tag{5.16}$$

$$\sigma_{\bar{\varepsilon}} = \left[\frac{\sum_{i=1}^{n}(\varepsilon_i - \bar{\varepsilon})^2}{n(n-1)\Delta\bar{\varepsilon}^2}\right]^{1/2} \tag{5.17}$$

The difference between the top and bottom detector asymmetries ε_{diff} is also tabulated. The error in this case is calculated in a manner identical to Eqs. (5.13) and (5.14) except that the correlation terms subtract from the total error, rather than adding to it.

5.3 Target Polarization

The solid ^{3}He sample is grown from a starting pressure of 46.16 bars. Under this pressure, liquid ^{3}He begins to solidify at a temperature of 1.2 K. The blocked-capillary method is used to confine the sample to a molar volume of 24.08 cm^3/mole (0.125 g/cm^3). Cooling along the melting curve, the 0.4 mole sample is completely solidified at 0.87 K and 35.72 bars. Based on the dimensions of the BeCu container and the measured packing fraction for the silver powder, the resulting thickness of solid ^{3}He is

$$\tau_3 = (4.34 \pm 0.09) \times 10^{22} \text{ atoms/cm}^2. \tag{5.18}$$

The 2% uncertainty in τ_3 is based on the combined uncertainties in the silver packing fraction and molar volume of ^{3}He [Gri71]. The entire solidification process requires less than one hour.

When a cold, liquid target is used to measure spin-spin asymmetries, the ^{3}He vapor pressure is reduced to slightly below that of the ^{3}He melting curve minimum, 29.31 bars. The target is then cooled below the temperature minimum of 316 mK, and the pressure increased in order to seal the sample at a molar volume of 26.18 cm^3/mole. This is the molar volume of liquid ^{3}He at the melting curve minimum.

The sample cell can be evacuated of ^{3}He by pumping on it with the activated-carbon dipsticks (Section 3.2.2). This process requires approximately three hours and

E_n (MeV)	T_3	$\pm$	ΔT_3	P_3	$\pm$	ΔP_3	method
1.94	12.27	$\pm$	0.25	0.365	$\pm$	0.006	MCT
3.65	12.88	$\pm$	0.26	0.351	$\pm$	0.006	MCT
4.95	15.27	$\pm$	0.31	0.307	$\pm$	0.005	MCT
7.46	13.16	$\pm$	0.30	0.345	$\pm$	0.007	NO

Table 5.4: Average temperature (in mK) and polarization of the solid ^{3}He target.

is facilitated by heating the sample above 3 K with a 500 Ω resistor attached to the top of the cell.

The polarization of the solid ^{3}He target P_3 is determined by measuring the temperature of the BeCu sample container and using Eq. (3.4). It is assumed that the solid ^{3}He is in adequate thermal contact with the BeCu container. The temperature is measured by either the ^{3}He melting curve thermometer (MCT) or the ^{60}Co nuclear orientation thermometer (NO) (Section 3.3).

The NO measurements are made prior to and immediately after the neutron asymmetry measurements[3]. The melting curve thermometer was used to monitor the temperature during the actual asymmetry measurement. In all cases where a direct comparison was possible, the two thermometric standards never disagreed by more than about 3%, with 2% being typical below 20 mK.

The average ^{3}He polarization listed in Table 5.4 is calculated from the average value of T_3 recorded by the melting curve thermometer during the neutron asymmetry measurement. An exception to this is the value of P_3 for the 7.46 MeV measurement. Due to operator error, the MCT did not function properly. Instead, P_3 is determined from the average value of the nuclear orientation thermometer. The temperature is measured immediately before (13.48 mK) and after (12.83 mK) beam was put on target.

[3]The necessary "warm" counts are obtained prior to cooling the target, or when the target is warmed to 1 K after the neutron asymmetry measurement. See Section 3.3.1.

5.4 Beam Polarization

The average polarization of the charged-particle beam is measured with a carbon-foil analyzer (Section 4.1.3). Because the carbon foil increases the emittance of the charged-particle beam, the beam intensity is reduced by as much as 50% whenever the foil is in place. Thus, measurements of the $^{12}C(p,p_0)^{12}C$ (or $^{12}C(d,p_0)^{13}C$) left-right asymmetries are taken every 2–3 hours and the foil is subsequently removed from the path of the beam. Each measurement consists of one 1024-channel run and requires approximately 15 minutes. The vector polarization of the charged-particle beam is then extracted from the corresponding value of the $^{12}C(p,p_0)^{12}C$ (or $^{12}C(d,p_0)^{13}C$) analyzing power. In the latter case, a correction factor must be included to account for the tensor polarization of the deuteron beam. Additional details are given in Appendix A.

The statistical accuracy obtained during one 15 minute measurement of P_p or P_d is far better than the accuracy of the corresponding analyzing power. Hence, the values of ΔP_n reported in Tables 5.5 and 5.6 are entirely due to the uncertainty in the various analyzing powers and polarization transfer coefficients. See Appendix A for a detailed discussion concerning the error associated with P_d and P_n.

In order to produce 1.94 MeV neutrons, the energy of the incident proton beam must be 3.02 MeV (Table 4.2). The carbon-foil analyzing power at this energy is small (approximately -0.15), making precise measurements of P_p difficult. Instead, the proton polarization is measured (immediately before and after the 1.94 MeV spin-spin measurements) at a proton energy of 4.66 MeV. The 1.94 MeV neutron polarization is calculated from the average of these two measurements of P_p. The same is true for the neutron polarization at 4.95 MeV ($E_d = 3.00$ MeV). The beam polarization for these asymmetry measurements is determined from the polarization of 5.00 MeV deuterons. Again, these polarimeter measurements are taken immediately before and after the 4.95 MeV spin-spin measurements.

Once the polarization of the charged-particle beam has been determined, the neutron polarization can be calculated using Eq. (4.8) or Eq. (4.9). The spin-axis of the neutron beam is parallel to the field of the superconducting magnet. In principle, this means that the magnet does not affect the neutron polarization. However, due to its finite extent, portions of the beam do encounter non-zero, perpendicular components

E_n (MeV)	Target	ε_p	P_p	$\pm$	ΔP_p	η	P_n	$\pm$	ΔP_n
1.94	Cold Solid	-0.303	0.752	$\pm$	0.034	0.978	0.482	$\pm$	0.035
	Cold Liquid	-0.303	0.752	$\pm$	0.034	0.978	0.482	$\pm$	0.035
	Warm Liquid	-0.303	0.752	$\pm$	0.034	0.978	0.482	$\pm$	0.035
3.65	Cold Solid	-0.314	0.780	$\pm$	0.035	0.984	0.530	$\pm$	0.040
	Cold Liquid	-0.295	0.731	$\pm$	0.032	0.984	0.500	$\pm$	0.038
	Warm Liquid	-0.292	0.725	$\pm$	0.033	0.984	0.492	$\pm$	0.038

Table 5.5: Average polarizations of the proton and neutron beams. All polarization measurements were made at $E_p = 4.66$ MeV.

E_n (MeV)	Target	ε_d	P_d	$\pm$	ΔP_d	η	P_n	$\pm$	ΔP_n
4.95	Cold Solid	-0.117	0.718	$\pm$	0.012	0.987	0.521	$\pm$	0.043
	Cold Empty	-0.117	0.718	$\pm$	0.012	0.987	0.521	$\pm$	0.043
7.46	Cold Solid	-0.116	0.715	$\pm$	0.012	0.990	0.632	$\pm$	0.051
	Cold Empty	-0.118	0.724	$\pm$	0.012	0.990	0.639	$\pm$	0.052
	Warm Empty	-0.117	0.717	$\pm$	0.012	0.990	0.634	$\pm$	0.052
	Warm Liquid	-0.114	0.703	$\pm$	0.012	0.990	0.622	$\pm$	0.049

Table 5.6: Average polarizations of the deuteron and neutron beams. All polarization measurements were made at $E_d = 5.00$ MeV.

of the superconducting field. The subsequent spin precession tends to depolarize the neutrons. This effect has been calculated by Wilburn [Wil93a] and found to be small (<3%). The final polarization of the neutron beam is then

$$P_n = \eta P_n' \tag{5.19}$$

where η is the depolarization factor calculated by Wilburn, and P_n' is the neutron polarization resulting from Eq. (4.8) or Eq. (4.9). The results are tabulated in Tables 5.5 and 5.6 for each of the twelve asymmetry measurements. The depolarization factor η has been included in the values listed for P_n.

5.5 Calculation of $\Delta\sigma_T$

At each energy, the spin-spin asymmetry is taken to be the difference between the cold (target polarized) and warm (target unpolarized) transmission asymmetries. To put the two measurements on more equal footing, we normalize each to the beam polarization during the respective measurement, and label the result y:

$$y = \frac{\bar{\varepsilon}_{cold}}{P_{n,cold}} - \frac{\bar{\varepsilon}_{warm}}{P_{n,warm}}. \tag{5.20}$$

The uncertainty associated with y should not include separate contributions from both $\Delta P_{n,cold}$ and $\Delta P_{n,warm}$. For a given energy, both $\Delta P_{n,cold}$ and $\Delta P_{n,warm}$ arise from uncertainties in the same analyzing powers and transfer coefficients. Instead, we can define average values $\bar{P}_n$ and $\Delta\bar{P}_n$ and write

$$(\Delta y)^2 = (\frac{\sigma_{\bar{\varepsilon}_{cold}}}{P_{n,cold}})^2 + (\frac{\sigma_{\bar{\varepsilon}_{warm}}}{P_{n,warm}})^2 + y^2(\frac{\Delta\bar{P}_n}{\bar{P}_n})^2, \tag{5.21}$$

where $\sigma_{\bar{\varepsilon}}$ is the standard deviation of the neutron-transmission asymmetry (Table 5.3). The first two terms on the right of Eq. (5.21) are statistical uncertainties, while the third term contributes a systematic uncertainty to $\Delta\sigma_T$.

$$\Delta y_{stat} = \sqrt{(\frac{\sigma_{\bar{\varepsilon}_{cold}}}{P_{n,cold}})^2 + (\frac{\sigma_{\bar{\varepsilon}_{warm}}}{P_{n,warm}})^2}. \tag{5.22}$$

$$\Delta y_{sys} = (\frac{\Delta\bar{P}_n}{\bar{P}_n})y. \tag{5.23}$$

In cases where more than one "warm" measurement was made, we use the warm liquid result to represent the instrumental aymmetry. At $E_n = 4.95$ MeV, the cold empty asymmetry is taken to be a measure of the background. Values of y and Δy are given Table 5.7.

Once the spin-spin asymmetry has been determined, $\Delta\sigma_T$ follows from

$$\Delta\sigma_T = -2\frac{y}{\tau_3 P_3}, \tag{5.24}$$

τ_3 being the thickness of the polarized target (4.34×10^{22} atoms/cm^2) and P_3 its polarization. One might wonder why we do not normalize Eq. (5.20) to the target thickness as well. This is a valid concern, since the density of a liquid target is

E_n (MeV)	y	$\pm$	Δy_{sys}	$\pm$	Δy_{stat}	unit
1.94	-94.15	$\pm$	7.16	$\pm$	5.39	10^{-4}
3.65	-87.23	$\pm$	6.66	$\pm$	6.77	10^{-4}
4.95	-56.12	$\pm$	4.63	$\pm$	2.73	10^{-4}
7.46	-32.20	$\pm$	2.57	$\pm$	1.40	10^{-4}

Table 5.7: Beam-normalized spin-spin asymmetries. See Eqs. (5.20–5.23) for definitions.

E_n (MeV)	$\Delta\sigma_T$ (b)	$\pm$	Δ_{sys}	$\pm$	Δ_{stat}	Δ_{tot}
1.94	1.190	$\pm$	0.092	$\pm$	0.066	0.113
3.65	1.144	$\pm$	0.089	$\pm$	0.086	0.124
4.95	0.843	$\pm$	0.071	$\pm$	0.040	0.081
7.46	0.431	$\pm$	0.036	$\pm$	0.018	0.040

Table 5.8: Measured values of $\Delta\sigma_T$.

approximately 8% less than a solid target. Before we can address this concern, we should investigate the possible sources of the intrumental asymmetries.

A plausible explanation is that the instrumental asymmetries are due to left-right[4] analyzing powers associated with the ^{3}H$(p,n)^3$He and ^{2}H$(d,n)^3$He source reactions. The collimation system defines an acceptance angle of $\pm 1.36°$ in the vertical plane. Since two neutron detectors are used (top and bottom), a non-zero analyzing power would cause the top detector to record more spin-up neutrons than the bottom detector[5]. However, the difference between ε_{top} and ε_{bot} should cancel if the two neutron detectors are centered precisely about 0°. The observed values of ε_{diff} (Table 5.3) indicate that this is probably not the case. We see however, that for a given beam energy, ε_{diff} does not depend upon the ^{3}He polarization or density or upon the polarization of any other material in the BeCu container. We conclude that the background asymmteries have little or nothing to do with the target.

Table 5.8 lists the values of $\Delta\sigma_T$ calculated according to Eq. (5.24). For each

[4]As was the case in Section 4.1.3, the scattering asymmetry would actually occur in the vertical plane, not the horizontal as "left-right" appears to indicate.

[5]Or *vice versa*, depending upon the sign of the analyzing power.

value of $\Delta\sigma_T$ three uncertainties are quoted — systematic and statistical,

$$\Delta_{sys} = \Delta\sigma_T\sqrt{(\frac{\Delta P_3}{P_3})^2 + (\frac{\Delta\tau_3}{\tau_3})^2 + (\frac{\Delta y_{sys}}{y_{sys}})^2} \quad (5.25)$$

$$\Delta_{stat} = \Delta\sigma_T\frac{\Delta y_{stat}}{y} \quad (5.26)$$

— as well as the total error, which is given by

$$\Delta = \sqrt{(\Delta_{sys})^2 + (\Delta_{stat})^2}. \quad (5.27)$$

5.6 Comparison to Phase-Shift Predictions

The $\Delta\sigma_T$ experimental results are plotted in Fig. 5.2. Also shown are the predictions of $\Delta\sigma_T$ using the four sets of n-^{3}He phase shifts discussed in Section 2.3. The phase shifts generated by Hale's R-matrix analysis clearly provide the best overall description of $\Delta\sigma_T$. Above 6 MeV, the MCRGM calculation is equally satisfactory. Neither the phase-shift analysis of Jany *et al.* or Lisowski *et al.* provide an adequate description of the data. This should be considered somewhat surprising, considering that both sets of phase shifts were generated as fits to n-^{3}He cross section and polarization data.

The agreement of the MCRGM calculation with our data is somewhat surprising as well. The unpolarized total cross section that results from the MCRGM phase shifts does not agree with experiment (Fig. 2.7). Our conclusion in Section 2.3.2 was that the MCRGM lacked sufficient P-wave amplitudes. The agreement with the $\Delta\sigma_T$ data is probably the result of a weak $^1P_1$ partial wave cancelling an equally weak $^3P_2$ partial wave. The former makes a negative contribution to $\Delta\sigma_T$, while the latter makes a positive contribution.

As discussed in Section 2.2.4, three total cross sections must be measured to fully specify the forward elastic-scattering amplitude. One of these, the unpolarized cross section, has been measured several times and over a wide range of energies [Til92]. The present results for $\Delta\sigma_T$ provide the second cross section, and plans to measure the final cross section, $\Delta\sigma_L$, have been made.

We have also discussed how combinations of these three cross sections can yield information concerning specific partial waves. We will now discuss two combinations

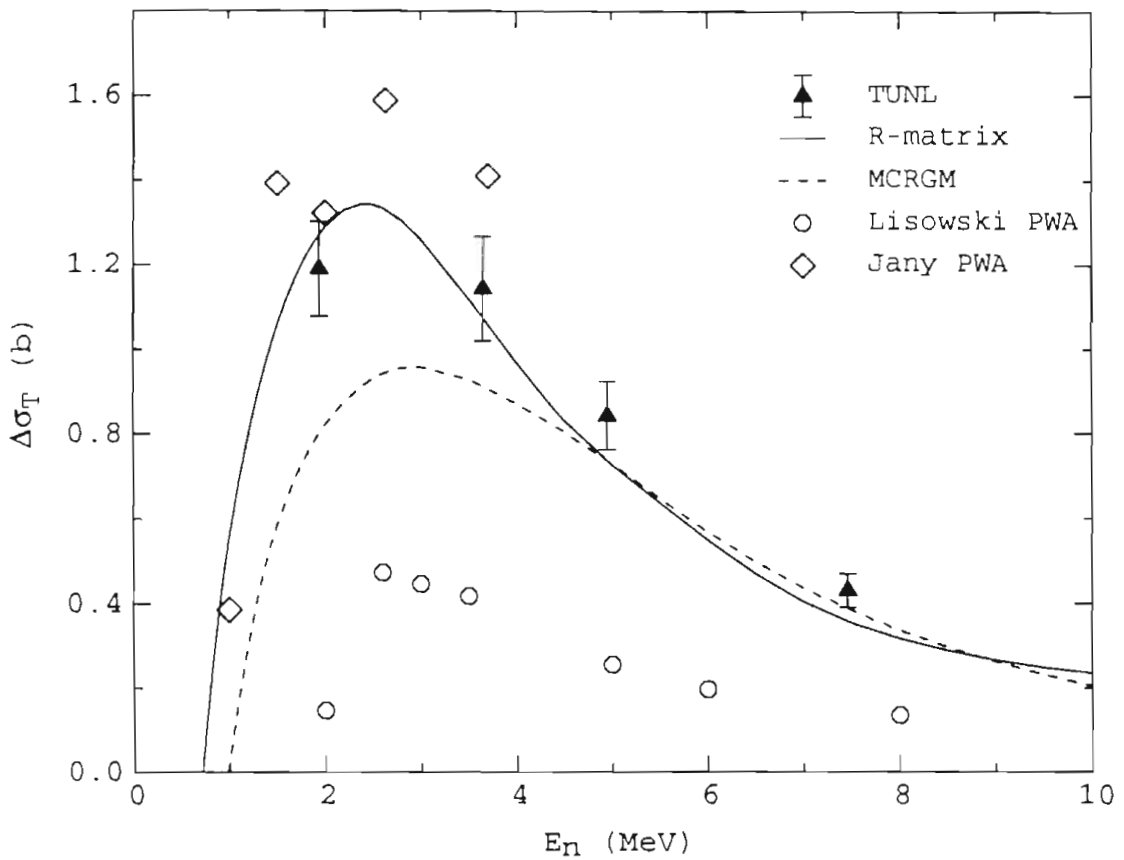

Figure 5.2: Comparison of $\Delta\sigma_T$ measurements with the phase-shift predictions of Section 2.3.

of the unpolarized total cross section, σ_0, with the present measurements of $\Delta\sigma_T$. The sum of these two cross sections, $(\sigma_0 + \Delta\sigma_T)$, is shown in Fig. 5.3. Values of σ_0 are obtained at 1.94, 3.65, 4.95,and 7.46 MeV from the ENDF/B-VI polynomial fit to the experimental results [Hal91a]. The fit has a quoted accuracy of 2%. Because this combination practically doubles the $^3P_2$ partial-wave cross section (see Eq. (5.28)), it effectively separates the phase-shift predictions into two categories. The R-matrix and Jany partial-wave analyses predict large $^3P_2$ contributions to the total cross section. Therefore, their predictions of $(\sigma_0 + \Delta\sigma_T)$ are also large and do a good job of describing the experimental results. The MCRGM and Lisowski PWA have smaller $^3P_2$ partial waves, and correspondingly smaller predictions of this particular cross section combination.

$$\begin{aligned}\sigma_0 + \Delta\sigma_T &= -\sigma(^1S_0) + \frac{5}{3}\sigma(^3S_1) - \sigma(^1P_1) \\ &\quad +3\sigma(^3P_0) + \sigma(^3P_1) + \frac{9}{5}\sigma(^3P_2) + \ldots \end{aligned} \tag{5.28}$$

$$\begin{aligned}\sigma_0 - \Delta\sigma_T &= 3\sigma(^1S_0) + \frac{1}{3}\sigma(^3S_1) + 3\sigma(^1P_1) \\ &\quad +\sigma(^3P_0) + \sigma(^3P_1) + \frac{1}{5}\sigma(^3P_2) + \ldots \end{aligned} \tag{5.29}$$

On the other hand, the combination $(\sigma_0 - \Delta\sigma_T)$ (Fig. 5.4) is relatively insensitive to the $^3P_2$ partial wave (Eq. (5.29)). None of the four sets of phase shifts exactly reproduce this combination. This is a bit perplexing, considering the R-matrix analysis' success in predicting $\Delta\sigma_T$. We see in Fig. 2.7 that the R-matrix over-predicts the *unpolarized* cross section in the 2–5 MeV region.

One possible explanation is that the R-matrix $^3P_1$ partial wave is too strong. At 5 MeV, this partial wave contributes more than 400 mb to the unpolarized cross section. However, the $^3P_1$ partial wave does not contribute to $\Delta\sigma_T$ at all. If we assume that the R-matrix over-estimate of σ_0 is mostly due to the $^3P_1$ partial wave, we arrive at the modified version of $\sigma(^3P_1)$ shown in Fig. 5.5. This "modification" has no effect on the R-matrix prediction of $\Delta\sigma_T$. On the other hand, $\Delta\sigma_L$ is highly sensitive to such changes, as evidenced by Fig. 5.6. The dip in the modified $^3P_1$ cross section at 2.5 MeV indicates that not all of the R-matrix overestimate of σ_0 can

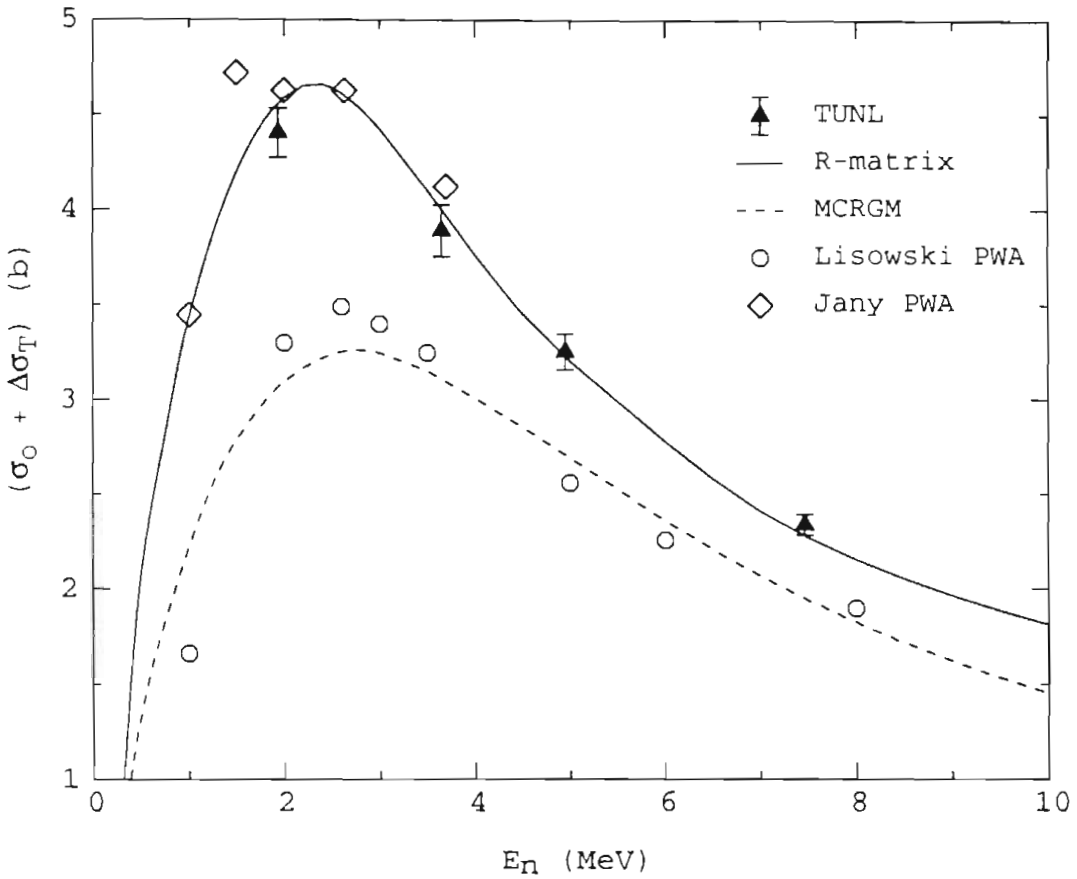

Figure 5.3: Sum of the unpolarized total cross section, σ_0 and $\Delta\sigma_T$. Symbols same as Fig. 5.2.

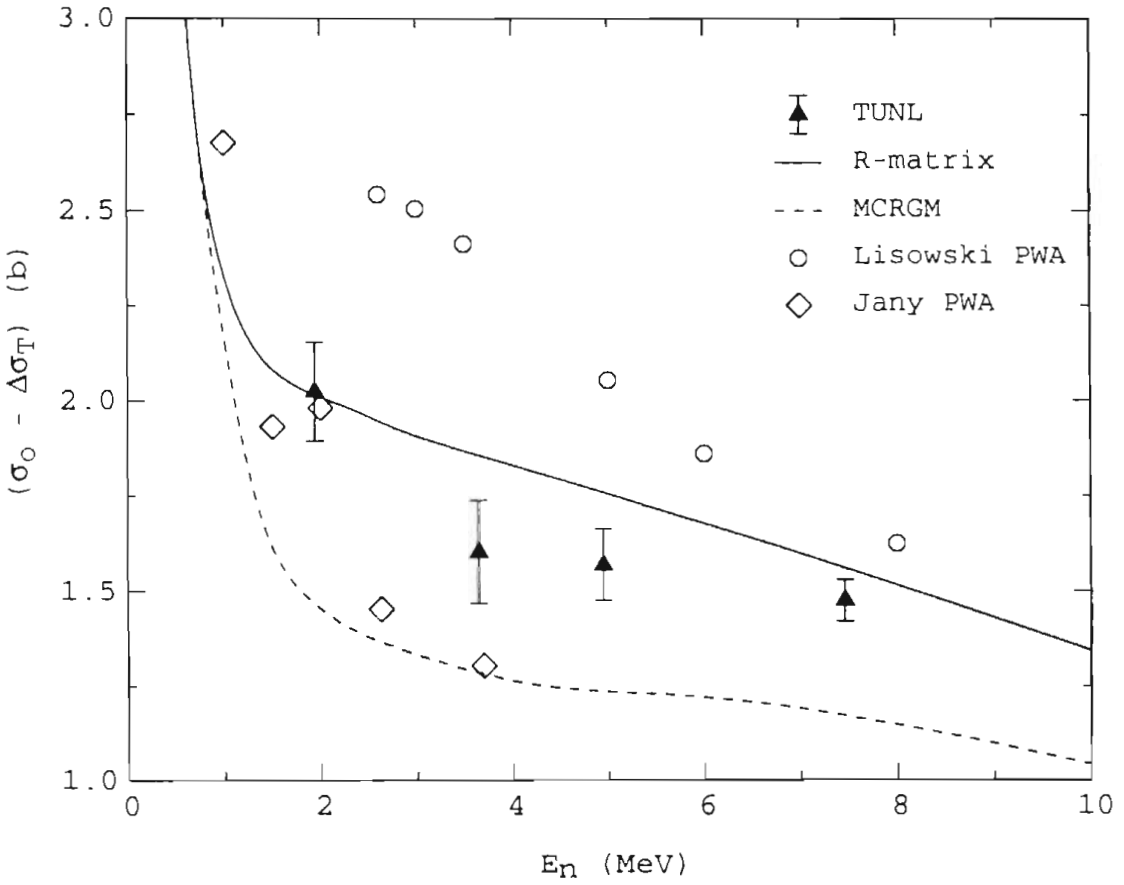

Figure 5.4: Difference between the unpolarized total cross section, σ_0 and $\Delta\sigma_T$. Symbols same as Fig. 5.2.

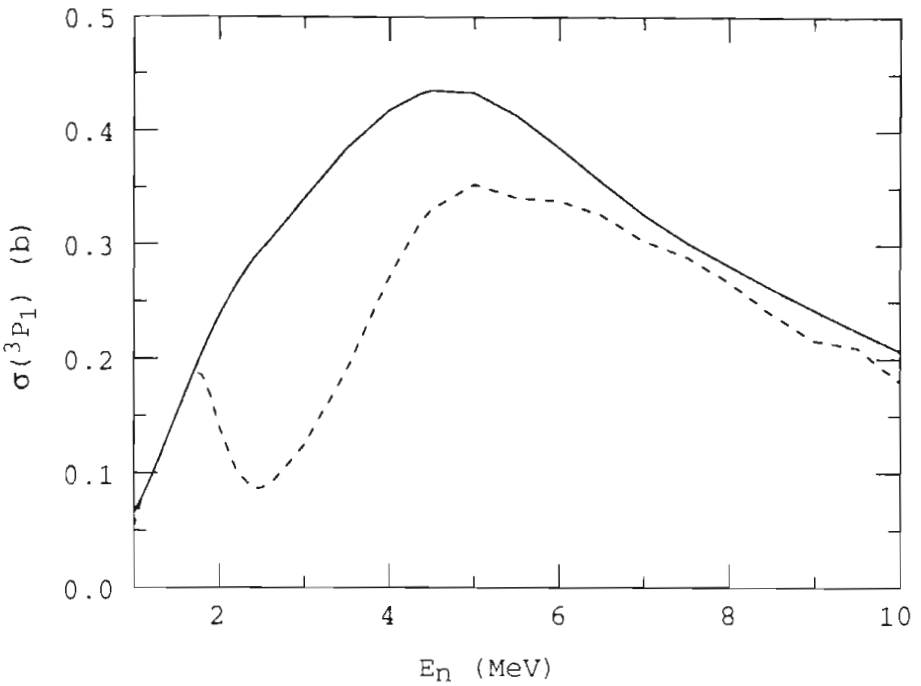

Figure 5.5: Modification of the $^3P_1$ partial-wave cross section. The $^3P_1$ partial wave of the R-matrix analysis (solid line) has been adjusted (dashed line) to fit the experimental values of the unpolarized total cross section between 1 and 10 MeV.

be attributed to this particular partial wave. However, this modification has been made to illustrate that a measurement of $\Delta\sigma_L$ can be used to better determine the resonance parameters of two particular excited states of ^{4}He.

The most dominant sources of the $^3P_1$ partial wave are two 1^- resonances at 23.6 MeV ($T = 1$) and 24.2 MeV ($T = 0$). Neither of these resonances were present in the earlier R-matrix analysis of Fiarman and Meyerhof [Fia73]. According to Hale's R-matrix analysis, both of these levels are predominately spin-triplet in the nucleon-trinucleon channels, and like most of the excited states of ^{4}He, they are extremely broad, 6 MeV.

Because they both overlap with the d-d threshold located at $E_x = 23.8$ MeV, the positions of these levels play an important role in fusion reactions. One of the most attractive methods to generate power is the ^{3}H$(d,p)^4$He reaction, because it does not produce neutrons. However, in a plasma, the deuterons are more likely

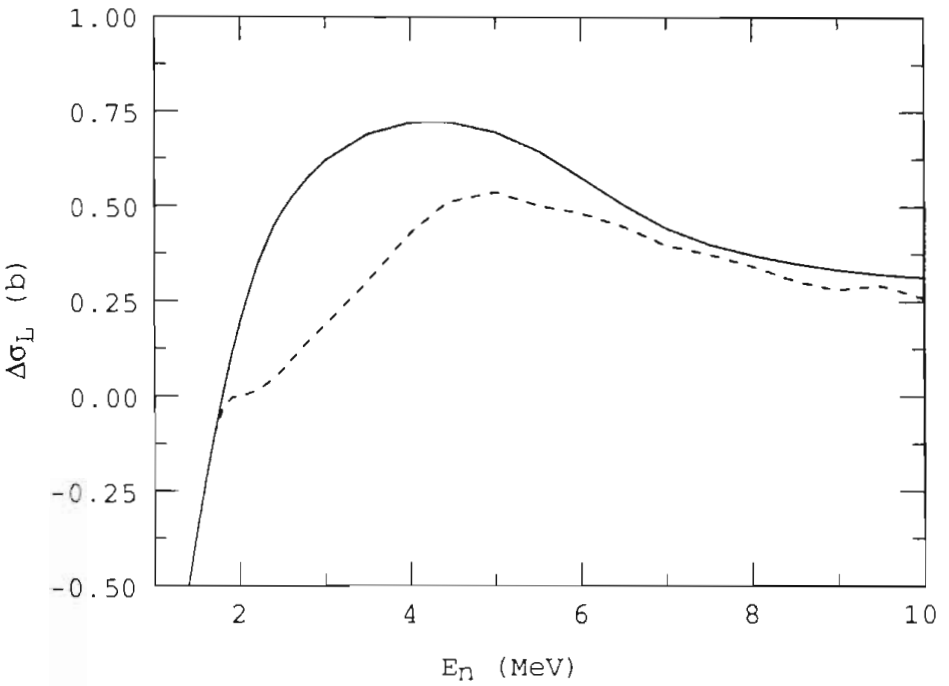

Figure 5.6: Sensitivity of $\Delta\sigma_L$ to modification of the $^3P_1$ partial wave. R-matrix predictions of $\Delta\sigma_L$ are shown using the original (solid line) and modified (dashed line) versions of the $^3P_1$ partial wave.

to fuse with other deuterons instead of ^{3}H. The competing reactions are $^2\mathrm{H}(d,p)^3\mathrm{H}$ and $^2\mathrm{H}(d,n)^3\mathrm{He}$. The latter reaction is especially troubling because the neutrons in the exit channel pose several technical problems. For many years it was believed that the neutron yield could be suppressed by polarizing the deuterons in the plasma [Kul82]. If at low energies, the $^2\mathrm{H}(d,n)^3\mathrm{He}$ and $^2\mathrm{H}(d,p)^3\mathrm{H}$ reactions are dominated by S waves, the entrance channel is a Pauli-forbidden state whenever both deuteron spins are parallel. Futhermore, the spin of one of the nucleons must flip in the exit channel.

However, the d-d threshold is located between two negative-parity resonances, and P waves contribute significantly to the $^2\mathrm{H}(d,p)^3\mathrm{H}$ and $^2\mathrm{H}(d,n)^3\mathrm{He}$ cross sections, even at center-of-mass energies below 50 keV [Fle94]. This suggests that polarizing the plasma in a $^3\mathrm{H}(d,p)^4\mathrm{He}$ reactor would not suppress the neutron yield.

The fact that the R-matrix phase shifts cannot reproduce σ_0 in the E_x = 22–

24 MeV region while it excels in predicting $\Delta\sigma_T$ indicates that modification of the resonance parameters for these 1^- levels may be necessary. Because of its sensitivity to the $^3P_1$ partial wave, an experimental determination of $\Delta\sigma_L$ might be used to resolve this discrepancy.

5.7 Additional Neutron-Transmission Asymmetry Measurements

In addition to the neuton-transmission measurements made with an unpolarized target or with a polarized target of solid ^{3}He, measurements were made with an empty target, or with polarized liquid ^{3}He. Refer to Table 5.1 for a complete summary of the measurements. The results are used to determine what, if any, contributions to the spin-spin asymmetries come from polarizable materials in the BeCu sample container.

At 7.46 MeV, measurements were made with a empty target cell — both cold ($\sim$15 mK) and warm (1 K) — and with a target cell filled with warm, liquid ^{3}He. All three results are identical to within the statistical accuracy of the measurements (Table 5.1). We conclude that the spin-spin asymmetry due to BeCu or silver powder is zero at the 6×10^{-5} level. The cold empty asymmetry obtained at $E_n = 4.95$ MeV, is consistent with the same measurement at 7.46 MeV. No additional "background" measurements were made at this energy.

Three background asymmetries were measured at each of the two lowest energies, 1.94 and 3.65 MeV. Here, the ^{3}He spin-spin cross section is quite large, 500 mbarn, and we expect to observe a spin-spin asymmetry due to polarized liquid ^{3}He. The polarization of the liquid is only about 2.9% (see Section 3.1.3), and its density is 8% less than that of the solid. Assuming 37% polarization of the solid, the liquid asymmetry should be of order 1/14 that of the solid.

If we plot the quantity ε_{sum}/P_n versus $\tau_3 P_3$, for each of the three asymmetry measurements, the result should be a straight line whose slope is simply the spin-spin cross section of ^{3}He[6]. This assumes that the only contribution to either the cold liquid or cold solid asymmetry is due to polarized ^{3}He. Any contribution due to polarized BeCu (or polarized silver) will cause the asymmtries to deviate from

[6]Actually, the slope is the *negative* of the spin-spin cross section, $-\sigma_{ss}$.

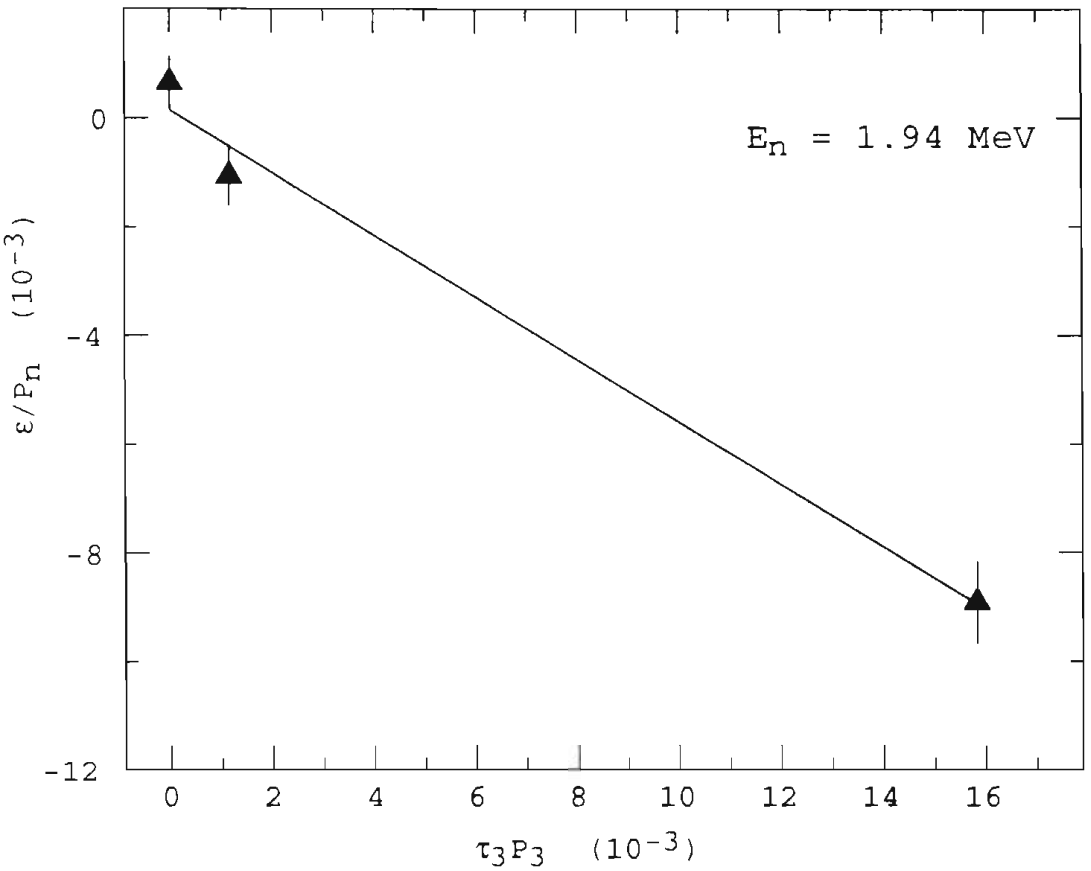

Figure 5.7: A linear least-squares fit to the neutron transmission asymmetries at 1.94 MeV. The ratio of transmission asymmetry to beam polarization ($\bar{\varepsilon}/P_n$) is plotted as a function of ^{3}He thickness times polarization ($\tau_3 P_3$). Data is shown for (left to right) warm liquid, cold liquid, and cold solid targets.

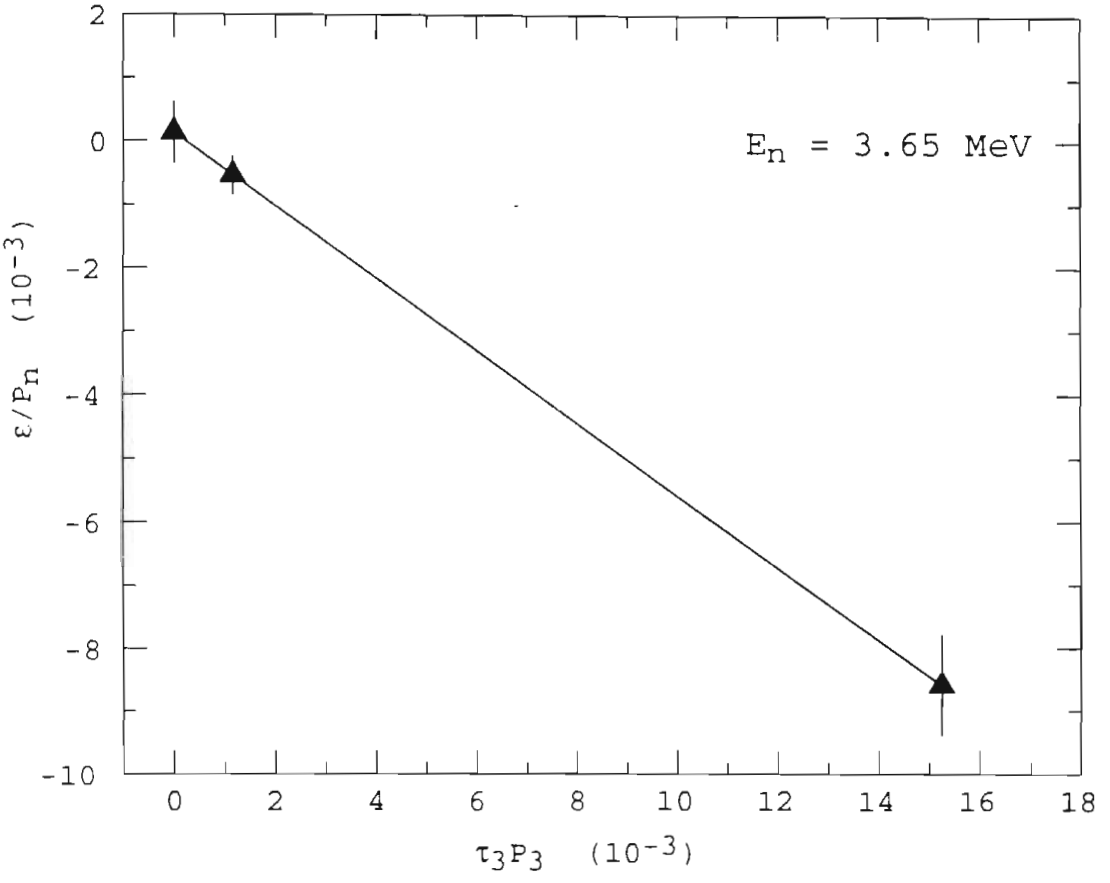

Figure 5.8: Same as Fig. 5.7 but $E_n = 3.65$ MeV.

this linear behavior. The results of this procedure are shown in Figs. 5.7 and 5.8. Least-squares fitting to the data yields the lines shown in the figures. The results, along with the total χ^2 for the fit, are

$$\begin{aligned} \frac{\bar{\varepsilon}_{sum}}{P_n} &= (-0.575)\,\tau_3 P_3 + 1.48 \times 10^{-4} \\ \chi^2 &= 2.29 \end{aligned} \tag{5.30}$$

for the 1.94 MeV data, and

$$\begin{aligned} \frac{\bar{\varepsilon}_{sum}}{P_n} &= (-0.572)\,\tau_3 P_3 + 1.29 \times 10^{-4} \\ \chi^2 &= 0.004 \end{aligned} \tag{5.31}$$

at 3.65 MeV.

Equation 5.31 yields a result for $\Delta\sigma_T$ of 1.144 b — in agreement with Table 5.8. The result from the linear fit at 1.94 MeV ($\Delta\sigma_T$ = 1.150 b) is within the ±113 mb error quoted in Table 5.8. We again conclude that spin-spin asymmetries due to any material other than ^{3}He are absent during the neutron transmission measurements.

5.8 Evaluation of Target Performance

The thickness of of the TUNL polarized solid ^{3}He target (4.34×10^{22} atoms/cm^2) is an order of magnitude greater than any polarized gas target of ^{3}He currently in operation [Lar94, Bec94]. Its density corresponds to approximately 750 bars of room-temperature gas. The polarizations achieved during this experiment (32–40%) are not as great as those of the gas targets (typically 50–60%, with 10 bars of ^{3}He). However, comparing the figure of merit for total cross section measurements such as these, $(\tau_3 P_3)^2$, the TUNL target has the advantage by at least two orders of magnitude.

In Section 3.5 we expressed concern about the possibility of depolarization due to beam-related heating of the target. *No such heating was observed during any of the neutron-transmission measurements.* On the contrary, in every single case the target continued to cool throughout the measurement. Table 5.9 lists the initial, final, and average temperatures observed for asymmetry measurements involving solid ^{3}He.[7] To

[7] The apparent warming that takes place during the 1.94 MeV measurement is due to a partial stoppage of the dilution refrigerator cold traps.

E_n (MeV)	T_i	T_f	T_{avg}	$\pm$	ΔT_{avg}	method
1.94	12.17	12.04	12.27	$\pm$	0.25	MCT
3.65	13.65	11.92	12.88	$\pm$	0.26	MCT
4.95	15.31	15.02	15.27	$\pm$	0.31	MCT
7.46	13.48	12.83	13.16	$\pm$	0.30	NO

Table 5.9: Initial, final, and average temperatures (in mK) for the solid ^{3}He target during neutron-transmission measurements.

further illustrate this fact, we show the cooling curve of the target before, during, and after the measurement at 3.65 MeV (Fig. 5.9).

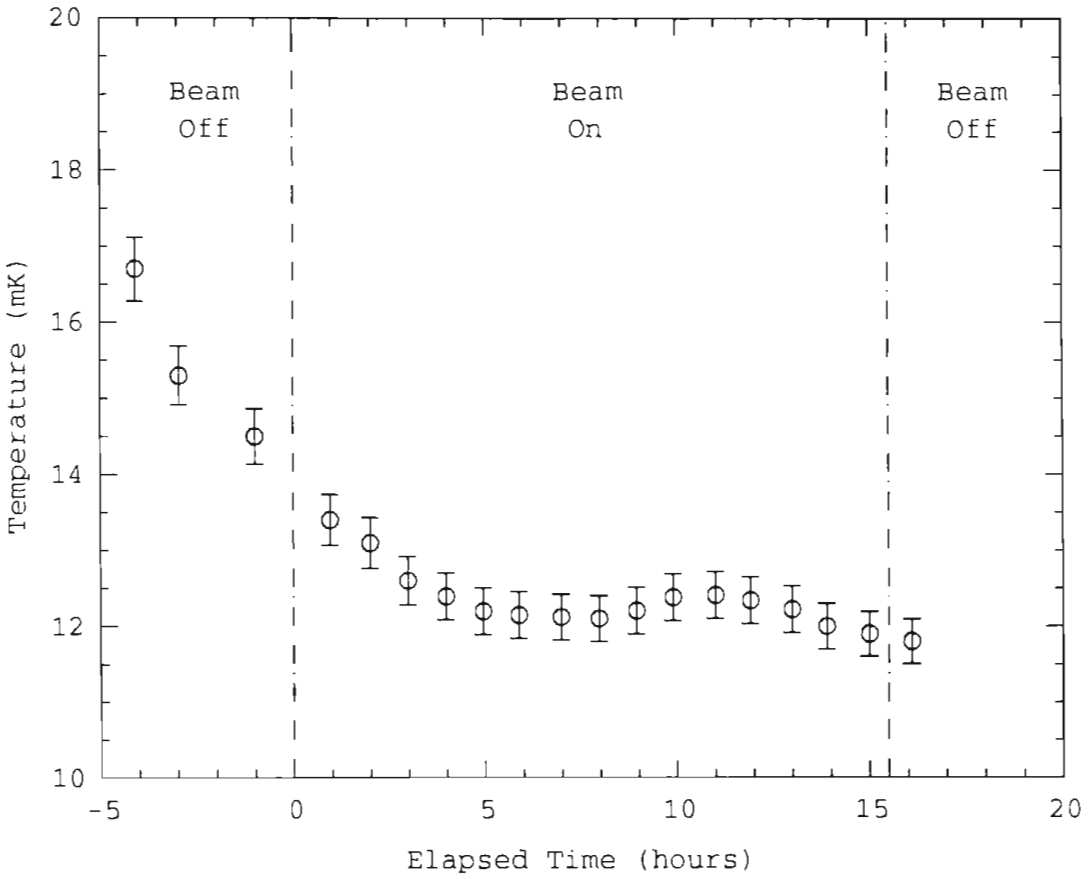

Figure 5.9: Cooling of the solid ^{3}He target during the neutron asymmetry measurement at $E_n = 3.65$ MeV. Target temperature determined by the ^{3}He melting curve thermometer.

Chapter 6

Summary and Conclusions

The total cross section difference $\Delta\sigma_T$ for the scattering of polarized neutrons from polarized ^{3}He has been measured for incident neutron energies between 2 and 8 MeV. The experiment was performed with both beam and target spins transverse to the incident beam momentum, and is highly sensitive to the $\ell = 0$ and $\ell = 1$ scattering amplitudes. The cross section differences were extracted from the observed asymmetries in neutron transmission when the spin of the incident beam was reversed. This is the first polarized neutron—polarized ^{3}He measurement that covers a broad portion of the ^{4}He excited state spectrum.

The present results have been compared to phase-shift predictions from four independent analyses of the n-^{3}He system:

1. a comprehensive, charge-independent R-matrix analysis of nearly all $A = 4$ scattering and reaction data [Hal];

2. the single-energy partial-wave analysis of Lisowski *et al.* [Lis76];

3. the single-energy partial-wave analysis of Jany *et al.* [Jan88];

4. a Multi-Channel Resonating Group Model calculation of the ^{3}He scattering states [Hof].

The observed values of $\Delta\sigma_T$ are in disagreement with predictions based on both partial-wave analyses and the MCRGM calculation (items 2–4 above). In most cases the disagreement can be explained as the result of one or two phase shifts. The results

are well reproduced by the phase shifts from the R-matrix analysis and lend further support to the ^{4}He energy level scheme proposed by Hale *et al.* [Hal, Til92].

When comparison is made simultaneously with both $\Delta\sigma_T$ and the total unpolarized cross section σ_0, there is indication that the R-matrix level scheme overpredicts the n-^{3}He $^3P_1$ partial wave. This partial wave is dominated by the presence of two negative-parity, $J = 1$ resonances in the ^{4}He compound nucleus. Both resonances are located very near the ^{2}H + d threshold, and play important roles in d-d fusion reactions.

It is planned to repeat the present measurements with longitudinally polarized beam and target. The total cross section difference for this geometry, $\Delta\sigma_L$, is highly sensitive to the partial wave in question.

Measurements were made with a 0.4 mole target of polarized solid ^{3}He. The target was cooled to approximately 12 mK in the 7 Tesla magnetic field of a superconducting magnet, resulting in a ^{3}He nuclear polarization of 38%. The sample temperature was determined using two independent thermometric standards: ^{60}Co γ-ray anisotropy and the ^{3}He melting curve. This is the first time that the latter has been used to determine the polarization of a statically-polarized target. Agreement between the two thermometers was typically better than 2%. There was no evidence of heating caused by neutron or γ-ray interactions inside the target.

The target developed for this experiment is the largest polarized ^{3}He target yet constructed for a nuclear physics experiment. It is an attractive candidate for experiments requiring polarized high-density ^{3}He, but which produce little heat inside the target and which are insensitive to the effects of a 7 Tesla polarizing field. The figure-of-merit chosen for comparing polarized targets is usually (polarization $\times$ density)^2. In comparison with current state-of-the-art gaseous targets, the present target excels by three orders of magnitude.

Plans for further target development include investigation of the higher-density hcp phase of ^{3}He, and solidification by the Pomeranchuk Effect. In either scheme, the polarization of the present target can, in principle, be exceeded by 5–10%.

The Pomeranchuk Effect involves cooling by the isoentropic compression of the liquid phase [Lou74]. If compression is begun at 50 mK, the solid may be cooled as low as 1–2 mK. This may significantly reduce the time required to polarize the sample. At the same time a polarization as high as 60–70% may result. It remains

to be seen however, whether it is possible to maintain such a low temperature for the duration of a nuclear physics experiment. It may also be difficult to grow the solid with a homogeneous temperature throughout the sample.

There are also two advantages to cooling in the hcp phase. First, the sample density may be increased 50–100%. Second, unlike the bcc phase of ^{3}He, the hcp phase does not suffer from antiferromagnetic corrections to the Curie law [Dob93]. Hence for a given temperature, the polarization of the hcp phase is higher.

The role of the silver powder inside the BeCu container is unclear. Some amount of powder is certainly necessary to provide good thermal contact to the dilution refrigerator, but it may be adequate to locate the powder in an area outside the neutron beam. While the powder probably improves the temperature homogeneity of the solid ^{3}He, it makes the target more susceptible to heating from neutron and γ-ray induced reactions.

In conclusion, we have demonstrated that a polarized target of solid ^{3}He can be used in a nuclear physics experiment. The present $\Delta\sigma_T$ results are in agreement with the current, experimentally-derived ^{4}He level scheme and can be used to characterize future target developments.

Appendix A

Determination of the Deuteron Polarization

In order to determine the polarization of neutrons produced via the ^{2}H$(d,n)^3$He reaction, both the vector (P_d) and tensor (P_{dd}) polarizations of the deuteron beam must be known. These polarizations can be extracted from the left-right asymmetry ε_d measured at the carbon-foil polarimeter (Section 4.1.3). A calibration of ε_d versus the resultant neutron polarization P_n has been performed at $E_d = 5.0$ MeV by Wilburn *et al.* [Wil93b]. This calibration allows us to write

$$\varepsilon_d = \chi A_{eff} P_n \tag{A.1}$$

where A_{eff} is an "effective" analyzing power, and χ is a corrective term that depends on the tensor polarization of the deuteron beam. During the calibration P_{dd} was close to zero, and so $\chi \simeq 1$. For this experiment we expect $P_{dd} \simeq P_d$, and so it is necessary to calculate the correction factor based on our knowledge of the ^{12}C$(d,p_0)^{13}$C and ^{2}H$(d,n)^3$He reactions.

The left-right asymmetry that is produced in the carbon-foil polarimeter by the ^{12}C$(d,p_0)^{13}$C reaction is given by Eq. (4.6), while Eq. (4.9) relates the polarization of the neutrons produced via the ^{2}H$(d,n)^3$He reaction to the deuteron polarization (vector and tensor). To avoid confusion between the analyzing powers of the ^{2}H$(d,n)^3$He and ^{12}C$(d,p_0)^{13}$C reactions, we write the latter in terms of spherical analyzing powers iT_{11}, T_{20}, and T_{22}, and use cartesian geometry to label the ^{2}H$(d,n)^3$He tensor

analyzing power A_{zz}[1] The correction factor is then given by

$$\chi = \frac{c}{f} \tag{A.2}$$

where

$$c = 1 - \frac{1}{4} A_{zz} P_{dd} \tag{A.3}$$

$$f = 1 - \frac{1}{2} P_{dd} (\sqrt{3}\, T_{22} \sin^2\beta + \frac{1}{\sqrt{2}} T_{20} \sin^2\beta - \sqrt{2}\, T_{20} \cos^2\beta) \tag{A.4}$$

and $\beta = 93°$ (see Fig. 4.5).

In order to determine χ we make the following assignments:

$$A_{eff} = 0.1455 \pm 0.0028 \tag{A.5}$$

$$P_{dd}^{\pm} = |P_d^{\pm}| \tag{A.6}$$

$$T_{20} = 0.05 \pm 0.1 \tag{A.7}$$

$$T_{22} = 0.20 \pm 0.1. \tag{A.8}$$

The ($\pm$) sign in Eq. (A.6) labels the spin state of the polarized ion source. The analyzing power in Eq. (A.5) was determined experimentally by Wilburn *et al.* The validity of Eq. (A.6) can be judged by Figs. 4.2 and 4.3. We see that in both cases, the transition which de-populates the $m = 0$ spin state is responsible for populating the $m = \pm 1$ spin state. Therefore the likelihood of producing $P_d = \pm 1$ is (to a good approximation) equal to the likelihood of producing $P_{dd} = 1$.

The quoted values of T_{20} and T_{22} are taken from measurements of these quantities at deuteron energies 9–12 Mev [Bas77], [Dre77], and [Lan88]. Measurements of T_{20} between 5–12 MeV have been made by Meyer and Thomson [Mey73], but at angles less than 15°. However, their results support our assumption that the tensor analyzing powers vary more slowly with E_d as the lab angle increases. Still, the validity of using the 12 MeV values of T_{20} and T_{22} is questionable. A new calibration of the carbon-foil polarimeter is planned.

The deuteron polarization (and hence the neutron polarization) is calculated in an iterative process based on ε_d. First the neutron polarization (for both spin states) is

[1] The relations between the spherical and cartesian analyzing powers (T_{kq} and A_{ij}) are identical to those between the polarization tensors (t_{kq} and P_{ij}), which are given Section 2.1.

Polarimeter Asymmetries	ϵ_d^+		ϵ_d^-		$\bar{\epsilon}_d$	
	-0.1146		0.1182		-0.1164	
Iteration	χ^+	χ^-	P_y^+	P_y^-	P_n^+	P_n^-
1	1.000	1.000	—	—	0.788	-0.812
2	1.300	1.308	0.814	-0.840	0.608	-0.621
3	1.244	1.251	0.688	-0.706	0.634	-0.650
4	1.252	1.260	0.708	-0.727	0.629	-0.645
5	1.251	1.258	0.705	-0.724	0.630	-0.646
5	1.251	1.258	0.705	-0.724	0.630	-0.646
Average	1.254		0.715 ± 0.012		0.638 ± 0.051	

Table A.1: Convergence of the neutron polarization at 7.43 MeV. Values of the vector and tensor analyzing powers are quoted in the text. In all cases, $P_{dd}^{\pm} = P_d^{\pm}$.

calculated from Eq. (A.1), assuming $\chi = 1$. This value of P_n is then used to generate the deuteron polarization.

$$P_d = \frac{cP_n}{\frac{3}{2}K_y^{y'}}. \tag{A.9}$$

The tensor polarization for each spin state is assigned the absolute value of the corresponding vector polarization, and the results are used to calculate $\chi^{\pm}$. These values of the correction factor are inserted in Eq. (A.1) and P_n, P_d and P_{dd} are calculated in the same fashion as before. The process is repeated until P_n converges (Table A.1).

The error associated with calculating P_n in this fashion is dominated by the uncertainty in T_{20} and T_{22}, but includes a contribution from P_d. Neglecting the statistical error in our measurement of ϵ_d, the error in the neutron polarization can be expressed as

$$\begin{aligned}
\Delta P_n &= P_n \left[\left(\tfrac{\partial A_{eff}}{\partial P_n}\Delta A_{eff}\right)^2 + \left(\tfrac{\partial T_{20}}{\partial P_n}\Delta T_{20}\right)^2 + \left(\tfrac{\partial T_{22}}{\partial P_n}\Delta T_{22}\right)^2 \right. \\
&\qquad \left. + \left(\tfrac{\partial A_{zz}}{\partial P_n}\Delta A_{zz}\right)^2 + \left(\tfrac{\partial P_d}{\partial P_n}\Delta P_d\right)^2 \right]^{1/2} \\
&= P_n \left[\left\{ \left(\frac{\Delta f}{f}\right)^2 + \left(\frac{\frac{1}{4}\Delta A_{zz}}{c}\right)^2 \right\} P_d^2 + \left(\frac{1}{c} - \frac{1}{f}\right)^2 \left(\frac{\Delta P_d}{P_d}\right)^2 \right]^{1/2}
\end{aligned} \tag{A.10}$$

where the variances $(\Delta f)^2$ and $(\Delta P_d)^2$ are given by

$$(\Delta f)^2 = \frac{3}{4}\sin^2\beta(\Delta T_{22})^2 + \left(\frac{1}{2\sqrt{2}}\sin^2\beta - \frac{\sqrt{2}}{2}\cos^2\beta\right)^2 (\Delta T_{20})^2 \qquad (A.11)$$

$$(\Delta P_d)^2 = \left(\frac{P_n}{a^2}\right)^2 \left[\frac{9}{4}(\Delta K_y^y)^2 + \frac{1}{16}P_n^2(\Delta A_{zz})^2 + \frac{9}{4}(K_y^y)^2(\frac{\Delta P_n}{P_n})^2\right], \qquad (A.12)$$

with

$$a = \frac{3}{2}K_y^y + \frac{1}{4}A_{zz}P_n \qquad (A.13)$$

We see that the error in the deuteron polarization includes a contribution due the uncertainty in neutron polarization. We can move this contribution to the left side of Eq. (A.10) and write

$$\left(\frac{\Delta P_n}{P_n}\right)^2 = \frac{\left\{(\frac{\Delta f}{f})^2 + \frac{1}{16}(\frac{\Delta A_{zz}}{c})^2\right\} P_d^2 + (\frac{1}{c} - \frac{1}{f})^2 \left\{\frac{9}{4}(\Delta K_y^y)^2 + \frac{1}{16}P_n^2(\Delta A_{zz})^2\right\} (\frac{P_n}{a^2 P_d})^2}{1 - \frac{9}{4}(\frac{1}{c} - \frac{1}{f})^2(\Delta K_y^y)^2(\frac{P_n}{a^2 P_d})^2}. \qquad (A.14)$$

The uncertainty in the deuteron polarization ΔP_d listed in Table A.1 does *not* include the ΔP_n contribution on the right-hand side of Eq. (A.12). However, the value of ΔP_n is complete, calculated from Eq. (A.14).

References

[And70] A. C. Anderson. *Elementary Dilution Refrigeration.* Rev. of Sci. Instr., **41**(1970) 1446–1450.

[Bas77] A. K. Basak, J. A. R. Griffith, O. Karban, S. Roman, and G. Tungate. *Analysing Powers of the $(\vec{d},p)$ and $(\vec{d},t)$ Reactions Induced by 12 MeV Polarized Deuterons in the 1p Shell.* Nucl. Phys., **A286**(1977) 420–430.

[Bec94] J. Becker, W. Heil, B. Krug, M. Leduc, M. Meyerhoff, P. J. Nacher, E. W. Otten, Th. Prokscha, L. D. Schearer, and R. Surkau. *Study of Mechanical Compression of Spin-Polarized ^{3}He Gas.* Nucl. Instr. and Meth. A, **346**(1994) 45–51.

[Ben87] A. Benoit, J. Bossy, J. Flouquet, D. Rufin, and J. Schweizer. *Neutron Experiments on Solid ^{3}He.* Can. J. of Phys., **65**(1987) 57–68.

[Bla52a] J. M. Blatt and L. C. Biedenharn. *The Angular Distribution of Scattering and Reaction Cross Sections.* Rev. of Mod. Phys., **24**(1952) 258–272.

[Bla52b] J. M. Blatt and V. F. Weisskopf. *Theoretical Nuclear Physics.* John Wiley and Sons, New York, 1952.

[Bow82] J. E. Bowsher. *BABEL*, 1982. Computer code.

[Bra88] R. A. Brandenburg, G. S. Chulick, R. Machleidt, A. Picklesimer, and R. M. Thaler. *Essential Mechanisms in the Triton Binding.* Phys. Rev. C, **37**(1988) 1245–1252.

[Bri71] D. M. Brink and G. R. Satchler. *Angular Momentum.* Oxford University Press, New York, 1971.

[Bus84] P. A. Busch, S. P. Cheston, and D. S. Greywall. *Properties of Sintered-Silver Heat Exchangers.* Cryogenics, **8**(1984) 445–447.

[Chu87] T. E. Chupp, M. E. Wagshul, K. P. Coulter, A. B. McDonald, and W. Happer. *Polarized, High-Density, Gaseous ^{3}He Targets.* Phys. Rev. C, **36**(1987) 2244–2251.

[Cle93] T. B. Clegg, H. J. Karwowski, S. K. Lemieux, R. W. Sayer, E. R. Crosson, W. M. Hooke, C. R. Howell, H. W. Lewis, A. W. Lovette, H. J. Pfützner, K. A. Sweeton, and W. S. Wilburn. *A New Atomic Beam Polarized Ion Source for the Triangle Universities Nuclear Laboratory: Overview, Operating Experience, and Performance.* Submitted to Nucl. Instr. and Meth., 1993.

[Col63] F. D. Colgrove, L. D. Schearer, and G. K. Walters. *Polarization of ^{3}He Gas by Optical Pumping.* Phys. Rev., **132**(1963) 2561–2572.

[Das65] P. Das, R. De Bruyn Ouboter, and K. W. Taconis. In *Proceedings of the 9th International Conference Low Temperature Physics*, page 1253, London, 1965. Plenum Press.

[Dob83] E. R. Dobbs. *Superfluid Helium Three.* Contemp. Phys., **24**(1983) 389–413.

[Dob93] E. R. Dobbs. *Solid Helium Three.* Oxford University Press, Oxford, 1993.

[Dre77] W. Drenckhahn. *Untersuchung der Reaktion $^{12}C(d,p)^{13}C$ mit Tensorpolarisierten Deuteronen.* Ph.D. thesis, Univerität Erlangen-Nürnberg, 1977.

[DS66] A. De-Shalit and J.D. Walecka. *Nuclear Spectroscopy of the α Particle.* Phys. Rev., **147**(1966) 763–773.

[Fia73] S. Fiarman and W. E. Meyerhof. *Energy Levels of Light Nuclei $A = 4$.* Nucl. Phys., **A206**(1973) 1–64.

[Fle94] K. A. Fletcher, Z. Ayer, T. C. Black, R. K. Das, H. J. Karwowski, E. J. Ludwig, and G. M. Hale. *Tensor Analyzing Powers for $^2H(d,p)^3H$ and $^2H(d,n)^3He$ at Deuteron Energies of 25, 40, 60, and 80 keV.* Phys. Rev. C, **49**(1994) 2305–2310.

[Fog92] W. E. Fogle, R. J. Soulen, and J. H. Colwell. *A New Cryogenic Temperature Scale from 6.3 to 650 mK.* In J. F. Schooley, editor, *Temperature, Its Measurement and Control in Science and Technology*, volume 6, pages 91–96. Am. Inst. Phys., New York, 1992.

[Fol64] L. L. Foldy and J. D. Walecka. Nuovo Cimento, **34**(1964) 1026.

[Fri90] J. L. Friar, B. F. Gibson, G. L. Payne, A. M. Bernstein, and T. E. Chupp. *Neutron Polarization in Polarized ^{3}He Targets.* Phys. Rev. C, **42**(1990) 2310–2314.

[Fuk87] H. Fukuyama, H. Ishimoto, T. Tazaki, and S. Ogawa. *^{3}He Melting Curve Below 15 mK.* Phys. Rev. B, **36**(1987) 8921–8924.

[Gou81] C. R. Gould, L. L. Holzsweig, S. E. King, Y. C. Lau, R. V. Poore, N. R. Roberson, and S. A. Wender. *The XSYS Data Acquisition System at Triangle Universities Nuclear Laboratory.* IEEE Trans. on Nucl. Sci., **NS-28**(1981) 3708–3714.

[Gou84] C. R. Gould, D. G. Haase, K. E. Nash, and N. R. Roberson. *The Cryogenic Polarized Target Facility.* In *Annual Report XXIII*, pages 121–123, Durham, North Carolina, 1984. Triangle Universities Nuclear Laboratory.

[Gre79] A. S. Greenberg and G. Armstrong. *Low-Temperature Thermal Conductivity of BCC ^{3}He.* Phys. Rev. B, **20**(1979) 1050–1060.

[Gre86] D. S. Greywall. *^{3}He Specific Heat and Thermometry at Millikelvin Temperatures.* Phys. Rev. B, **33**(1986) 7520–7538.

[Gri71] E. R. Grilly. *Pressure-Volume-Temperature Relations in Liquid and Solid ^{3}He.* J. Low. Temp. Phys., **4**(1971) 615–635.

[Haa86] D. G. Haase, C. R. Gould, and L. W. Seagondollar. *A Brute Force Polarized Target for Neutron Scattering Experiments.* Nucl. Instr. and Meth., **A243**(1986) 305–311.

[Hac71] H. H. Hackenbroich and P. Heiss. *A Microscopic Calculation for n-^{3}He Scattering.* Z. Physik, **242**(1971) 352–359.

[Hai72] R. C. Haight, J. E. Simmons, and T. R. Donoghue. *Polarization and Polarization Transfer in the Reaction $T(p,n)^3He$.* Phys. Rev. C, **5**(1972) 1826–1834.

[Hal] G. M. Hale, D. C. Dodder, and K. Witte. A=4 R-matrix analysis of 9/88 (unpublished).

[Hal90] G.M. Hale, D. C. Dodder, J. D. Seagrave, B. L. Berman, and T. W. Phillips. *Neutron-Triton Cross Sections and Scattering Lengths Obtained from p-^{3}He Scattering.* Phys. Rev. C, **42**(1990) 438–440.

[Hal91a] G. Hale, D. Dodder, and P. Young. *ENDF/B-VI Data File for ^{3}He.* National Nuclear Data Center, Brookhaven National Laboratory, Upton, New York, 1991.

[Hal91b] G.M. Hale. *Nuclear Physics of the Muon Catalyzed d+d Reactions.* Muon Catalyzed Fusion, **5/6**(1991) 227–232.

[Hof] H. M. Hofmann. unpublished.

[Hof81] H. M. Hofmann, W. Zahn, and H. Stöwe. *Microscopic Multi-Channel Calculations for the $A = 4$ Systems.* Nucl. Phys., **A357**(1981) 139–156.

[Jan88] P. Jany, W. Heeringa, H.O. Klages, B. Zeitnitz, and R. Garrett. *Analyzing Power of n-^{3}He Elastic Scattering from 1 to 2 MeV.* Nucl. Phys., **A483**(1988) 269–281.

[Kam92] H. Kamada and W.Glöckle. *Solutions of the Yakubovsky Equations for Four-Body Model Systems.* Nucl. Phys., **A548**(1992) 205–226.

[Kei92] C. D. Keith, C. R. Gould, D. G. Haase, N. R. Roberson, W. Tornow, and W. S. Wilburn. *^{3}He Melting Curve Thermometry in a Nuclear Polarization Experiment.* Hyperfine Interactions, **75**(1992) 525–532.

[Kel89] H. Kellermann, H. M. Hofmann, and Ch. Elster. *Gaussian Parameterization of a Meson-Theoretical N-N Potential for Microscopic Nuclear Structure Calculations.* Few-Body Sys., **7**(1989) 31–53.

[Kos90] J. E. Koster. *A Test of Time Reversal Invariance with Polarized Neutrons and Aligned ^{165}Holmium.* Ph.D. thesis, North Carolina State University, 1990.

[Kul82] R. M. Kulsrud, H. P. Furth, E. J. Valeo, and M. Goldhaber. *Fusion Reactor Plasmas with Polarized Nuclei.* Phys. Rev. Lett., **49**(1982) 1248–1258.

[Lan57] L. D. Landau. Soviet Phys. JETP, **3**(1957) 920.

[Lan79] J. Landau and Y. Eckstein. *Absence of Substrate Nucleation for BCC Solid ^{3}He on Grafoil.* Phys. Rev. Lett., **42**(1979) 67–70.

[Lan88] J. Lang, J. Liechti, R. Müller, P. A. Schmelzbach, and J. Smyrski. *Analyzing Power of the Reaction $^{12}C(\vec{d},p)$ Leading to Bound and Unbound States in ^{13}C.* Nucl. Phys., **A477**(1988) 77–88.

[Lar91] B. Larson, O. Häusser, P. P. J. Delheij, D. M. Whittal, and D. Thiessen. *Optical Pumping of Rb in the Presence of High-Pressure ^{3}He Buffer Gas.* Phys. Rev. A, **44**(1991) 3108–173.

[Lar94] B. Larson, O. Häusser, J. Alsher, M. Bahrami, E. J. Brash, W. J. Cummings, P. P. J. Delheij, R. Henderson, D. Ottewell, A. Rahav, S. Ram, M. C. Vetterli, and D. M. Whittal. *Asymmetries in 100 MeV π^+/π^- - $^3\vec{He}$ Elastic Scattering.* Phys. Rev. C, **49**(1994) 2045–2053.

[Leo87] W. R. Leo. *Techniques for Nuclear and Particle Physics Experiments.* Springer-Verlag, Berlin, 1987.

[Lis73] H. Liskien and A. Paulsen. *Neutron Production Cross Sections and Energies for the Reactions $T(p,n)^3$He, $D(d,n)^3$He and $T(d,n)^4$He.* Nuclear Data Tables, **11**(1973) 569–619.

[Lis75] P. W. Lisowski, R. L. Walter, C. E. Busch, and T. B. Clegg. *Polarization Transfer in the $^2H(\vec{d},\vec{n})^3$He Reaction at 0°.* Nucl. Phys., **A242**(1975) 298–308.

[Lis76] P. W. Lisowski, R. L. Walter, C. E. Busch, and T. B. Clegg. *Polarization Transfer Effects in $(\vec{p},\vec{n})$ Reactions on Light Nuclei at $\theta = 0°$*. Nucl. Phys., **A264**(1976) 188–196.

[Lon51] H. London. In *Proceedings of the International Conference on Low Temperature Physics*, page 157, 1951.

[Lou74] O. V. Lounasmaa. *Experimental Principles and Methods Below 1 K*, chapter 3, pages 17–58. Academic Press, London, 1974.

[Mac89] R. Machleidt. *The Meson Theory of Nuclear Forces and Nuclear Structure.* Adv. in Nucl. Phys., **19**(1989) 189–376.

[Mam83] T. Mamiya, A. Sawada, H. Fukuyama, K. Iwahashi, and Y. Masuda. *Molar Volume Dependence of the Pressure of Solid ^{3}He at Very Low Temperature.* In E. D. Adams and G. G. Ihas, editors, *Quantum Fluids and Solids- 1983*, volume 103, page 83. American Institute of Physics, 1983.

[Mar83] H. Marshak. *Nuclear Orientation Thermometry.* J. of Res. of the NBS, **88**(1983) 175–217.

[Mey73] H. O. Meyer and J. A. Thomson. *Compound-Nucleus and Deuteron D-State Effects in the T_{20} Analyzing Power of (d,p) Reactions.* Phys. Rev. C, **8**(1973) 1215–1221.

[Mos65] S. J. Moss and W. Haeberli. *The Polarization of Protons Scattered by Carbon.* Nucl. Phys., **72**(1965) 417–435.

[Ohl72] G. G. Ohlsen. *Polarization Transfer and Spin Correlation Experiments in Nuclear Physics.* Rep. on Prog. in Phys., **35**(1972) 717–801.

[Oku58] S. Okubo and R. E. Marshak. *Velocity Dependence of Two-Nucleon Interaction.* Ann. Phys., **4**(1958) 166–178.

[Pas66] L. Passell and R. I. Schermer. *Measurement of the Spin Dependence of the ^{3}He(n,p)T Reaction and of the Nuclear Susceptibility of Adsorbed ^{3}He.* Phys. Rev., **150**(1966) 146–151.

[Phi63] R. J. N. Phillips. *Spin-Dependent Analogues of the Optical Theorem.* Nucl. Phys., **43**(1963) 413–416.

[Pre62] M. A. Preston. *Physics of the Nucleus.* Addison-Wesley, Reading, MA, 1962.

[Ram70] H. Ramm, P. Pedroni, J. R. Thompson, and H. Meyer. *Nuclear Susceptibility of Liquid ^{3}He–II.* J. Low. Temp. Phys., **2**(1970) 539–553.

[Rob81] N. R. Roberson and S. E. Edwards. *Interface for the TUNL VAX Data Acquisition Facility.* IEEE Trans. on Nucl. Sci., **NS-28**(1981) 3834–3837.

[Rog83] M. Roger, J. H. Hetherington, and J. M. Delrieu. *Magnetism in Solid ^{3}He.* Rev. Mod. Phys., **55**(1983) 1–64.

[RS88] R. C. Richardson and E. N. Smith, editors. *Experimental Techniques in Condensed Matter Physics at Low Temperatures*, volume 67 of *Lecture Notes in Physics.* Addison Wesley, Redwood City, CA., 1988.

[Sat71] G. R. Satchler, T. B. Clegg, G. M. Hale, E. J. Ludwig, G. G. Ohlsen, and J. E. Simonius. *The Madison Convention.* In H. H. Barschall and W. Haeberli, editors, *Proceedings of the 3rd International Symposium on Polarization Phenomena in Nuclear Reactions, 1970*, pages xxv–xxix, Madison, 1971. The University of Wisconsin Press. Proceedings of the Third International Symposium on Polarization Phenomena in Nuclear Reactions.

[Sat83] G. R. Satchler. *Direct Nuclear Reactions.* Oxford University Press, New York, 1983.

[Say61] A. R. Sayres, K. W. Jones, and C. S. Wu. *Interaction of Neutrons with ^{3}He.* Phys. Rev., **122**(1961) 1853–1863.

[Sti85a] H. L. Stipdonk, G. Frossati, and J. H. Hetherington. *Mean Field Calculation of Magnetization, Entropy, and the Melting Pressure of Solid ^{3}He in High Magnetic Fields.* J. Low Temp. Phys., **61**(1985) 185–192.

[Sti85b] H. L. Stipdonk and J. H. Hetherington. *New Fit of the ^{3}He Solid Exchange Parameters.* Phys. Rev. B, **31**(1985) 4684–4687.

[Sto94] V. G. J. Stoks, R. A. M. Klomp, C. P. F. Terheggen, and J. J. de Swart. *Construction of High-Quality NN Potential Models.* Phys. Rev. C, **49**(1994) 2950–2962.

[Ter68] G. E. Terrell, M. F. Jahns, M. R. Kostoff, and E. M. Bernstein. *Polarization in $^{12}C(p,p)^{12}C$.* Phys. Rev., **173**(1968) 931–936.

[Til92] D. R. Tilley, H. R. Weller, and G. M. Hale. *Energy Level of Light Nuclei A=4.* Nucl. Phys., **A541**(1992) 1–104. This compilation article contains a complete reference guide to experimental and theoretical work on $A = 4$ nuclei since 1973.

[Tor74] W. Tornow. *Fast Neutron Double Scattering on ^4He.* Zeit. für Phys., **266**(1974) 357–365.

[Vog59] E. Vogt. *Resonance Reactions, Theoretical.* In P. M. Endt and M. Demeur, editors, *Nuclear Physics*, chapter V, pages 215–258. InterScience Publishing, New York. 1959.

[Wal71] R. L. Walter. *Sources of Polarized Fast Neutrons.* In H. H. Barschall and W. Haeberli, editors, *Polarization Phenomena in Nuclear Reactions*, pages 317–349. Madison. 1971. The University of Wisconsin Press. Proceedings of the Third International Symposium on Polarization Phenomena in Nuclear Reactions.

[Whi79] G. K. White. *Experimental Techniques in Low-Temperature Physics.* Oxford University Press, Oxford, 1979.

[Wil] W. S. Wilburn, C. R. Gould, D. G. Haase, P. R. Huffman, C. D. Keith, J. E. Koster, N. R. Roberson, and W. Tornow. *Calibration of the $^{12}C(p,p_0)^{12}C$ and $^{12}C(d,p)^{12}C$ vector analyzing powers versus the $^3H(p,n)^3He$ and $^2H(d,n)^3He$ polarization transfer coefficients.* unpublished.

[Wil67] J. Wilks. *The Properties of Liquid and Solid Helium.* Clarendon Press, Oxford, 1967.

[Wil93a] W. S. Wilburn. *Measurements of the Transverse Spin-Dependent Total Cross Section Difference $\Delta\sigma_T$ for the Scattering of Polarized Neutrons from Polarized Protons.* Ph.D. thesis, Duke University, 1993.

[Wil93b] W. S. Wilburn, C. R. Gould, D. G. Haase, P. R. Huffman, C. D. Keith, J. E. Koster, N. R. Roberson, and W. Tornow. *Measurements of Polarized Neutron-Polarized Proton Scattering: Implications for the Triton Binding Energy.* Phys. Rev. Lett., **71**(1993) 1982–1985.

[Wu62] T. Y. Wu and T. Ohmura. *Quantum Theory of Scattering.* Prentice-Hall, Englewood Cliffs, NJ, 1962.

[Zhe93] D. C. Zheng, B. R. Barrett, L. Jacqua, J. P. Vary, and R. J. McCarthy. *Microscopic Calculations of the Spectra of Light Nuclei.* Phys. Rev. C, **48**(1993) 1083–1091.